Novel phenomena caused by the chiral orders in metallic magnets

Teruo Yamazaki

Department of Materials science and Engineering, Kyoto University

Abstract

The "spin chirality" is an issue to attract many researchers in the recent solid state physics because it causes many interesting physical phenomena, such as the multiferroic effect and the spin Hall effect. In this thesis, several novel phenomena induced by the spin chirality in metallic helical magnets are reported. This thesis consists of the two parts as below.

(Part I) The novel chiral orders in the classical metallic helical magnet MnP are reported. One is the canted antiferromagnetic structure in the intermediate temperature range of 47 K < T < 282 K, the other is the tilted helical structure in the low temperature range of T < 47 K. It is considered that these chiral orders were induced by the Dzyaloshinsky-Moriya (DM) interaction. Moreover, I discovered a peculiar peculiar temperature hysteresis in the canted antiferromagnetic state, namely, the magnetization along the b-axis in the intermediate temperature range is distinctly enhanced by cooling the sample to the tilted helical phase once. Similar temperature hysteresis behaviors were also observed in the temperature dependences of the nuclear Bragg peaks obtained by the neutron scattering experiments. It suggests that the temperature hysteresis is accompanied by a lattice distortion. Hence, I speculate that the temperature hysteresis is caused by the inverse effect of the DM interaction to stabilize the vector chirality in MnP. It can be the first observation of the inverse effect of the DM interaction in the metallic system.

(Part II) Recently, the possibility of the novel spin dynamics driven by the electric current was theoretically proposed by Wessely *et al.*. According to this theory, a current through a bulk metal with a helical structure induces a spin transfer torque, which gives rise to a rotation of the magnetic moments with keeping its helical structure. In order to observe it experimentally, the AC susceptibility measurements were performed with applying the electric current to the sample in the rare-earth alloy $Gd_{0.62}Y_{0.38}$. An influence of the electric current on the AC susceptibility was observed, however, it is difficult to distinguish the effect of the electric current itself and that of the magnetic field accompanying the electric current. And hence, we cannot conclude that the spin transfer torque effect induced by the electric current is realized in the $Gd_{0.62}Y_{0.38}$ alloy or not. On the other hand, through

the investigation of the spin transfer torque effect, the strong non-linearity of the AC susceptibility in vicinity of the helical temperature and a remarkable increase of the imaginary part χ'' of the AC susceptibility in the temperature range of the helical phase was observed in $Gd_{0.62}Y_{0.38}$ even without the electric current. Such behaviors were not found in similar rare-earth Ho and $Ho_{0.60}Y_{0.40}$. It indicates that the weak magnetic anisotropy of Gd-moments is responsible for the strong nonlinear susceptibility and the anomalous slow dynamics in the helical phase. The anomalous slow dynamics can be caused by rotating spins with keeping their relative angle, the helical spin arrangement. In other words, the spins themselves can be rotated by the AC magnetic field, however, the vector chirality is preserved. It suggests a spin-chirality decoupling in the helical phase of $Gd_{0.62}Y_{0.38}$.

Contents

Part I

Peculiar temperature hysteresis accompanied by emergent chiral structures in MnP

Chapter 1

Introduction

1.1 New phenomena accompanied by the spin chirality

The 'spin chirality' has attracted many researchers as one of the central issues of the solid state physics. The spin chirality is a geometric quantity defined with plural spins and corresponds to the chirality of the optical isomers investigated in the chemistry, being a reflection asymmetric quantity. Two types of the spin chirality are defined, i.e. the vector chirality and the scalar chirality. The vector chirality is defined with the two spins of $\boldsymbol{S}_i$ and $\boldsymbol{S}_j$ as

$$\boldsymbol{\chi}_{ij} = \boldsymbol{S}_i \times \boldsymbol{S}_j. \tag{1.1}$$

The scalar chirality is defined with the three spins of $\boldsymbol{S}_i, \boldsymbol{S}_j$ and $\boldsymbol{S}_k$ as

$$\chi_{ijk} = \boldsymbol{S}_i \cdot (\boldsymbol{S}_j \times \boldsymbol{S}_k). \tag{1.2}$$

The signs of both chirality are changed by the reflection symmetry operation. The chirality is a quantity representing the handedness of the local structure, such as a molecular and a spin structure. The plus chirality corresponds to the right-handed structure and the minus chirality does the left-handed one. The vector chirality and the scalar chirality manifest themselves in different ways in physical phenomena are different a little because of the difference of their symmetries other than the reflection symmetry. For example, the vector chirality is time-reversal symmetric, however, the scalar chirality is antisymmetric.

The spin chirality was innovated into the solid state physics in order to describe the ordered states in frustrated spin systems, such as a triangular antiferromagnet [1, 2]. For example, an chiral ordered state of the vector chirality without any static orders of spin was theoretically predicted in a triangular Heisenberg antiferromagnet [3]. A ferro-chiral order of the vector chirality is equivalent to the helical

ordered state of spiral spin configuration with constant rotate angle. In this case, The left- and the right-handed chirality are called as a left- and a right-handed helicity. An example of antiferro-chiral orders of the vector chirality is the canted antiferromagnetic state in which the antiparallel-arranged spins are canted to the perpendicular direction. Figure 1.2 shows the schematic illustrations of these chiral orders.

In general, the spin chirality could not be directly observed and its role is hidden because the spin chirality does not couple directly with external fields such as a magnetic field. Recently, couplings between the spin chirality and other physical quantities have been studied extensively, and several novel phenomena originating from these couplings have been observed. For example, the multiferroic phenomena originating from the coupling between the spin chirality and the electric polarization in helical magnets and the chirality-driven anomalous Hall effect originating from scattering of conduction electrons by the spin chirality have been studied [4, 5, 6, 7, 8, 9, 10]. Esspecially, amazing responses to external fields have been observed in the multiferroic material such as a magnetization reversal by applying the electric field and an electric polarization flop by applying the magnetic field [7, 8, 11, 12].

In such phenomena, the Dzyaloshinsky-Moriya (DM) interaction originating from the spin-orbit interaction plays significant roles [13, 14]. The DM interaction is an antisymmetric interaction given by the form of

$$\boldsymbol{D}_{ij} \cdot (\boldsymbol{S}_i \times \boldsymbol{S}_j). \tag{1.3}$$

It can act only when the inversion symmetry at the center of sites of $\boldsymbol{S}_i$ and $\boldsymbol{S}_j$ is not preserved. The DM interaction can be rewritten by using the vector chirality $\boldsymbol{\chi}_{ij}$ as

$$\boldsymbol{D}_{ij} \cdot \boldsymbol{\chi}_{ij}. \tag{1.4}$$

Hence, The DM interaction can induce the vector chirality $\boldsymbol{\chi}_{ij}$ and stabilize the chiral structures such as the helical structure and the canted antiferromagnetic structure. Here, we consider the case that the DM interaction and an antiferromagnetic symmetric interaction $J_1 < 0$ act between the nearest neighbor (N. N.) spins, $\boldsymbol{S}_i$ and $\boldsymbol{S}_2$. The size of the spins and the angle between the N. N. spins are denoted as $S = |S_1| = |S_2|$ and $\pi - \theta$, respectively. The coupling energy coming from these interactions is written as

$$E(\theta) = -2|J_1|S^2 \cos\theta - DS^2 \sin\theta. \tag{1.5}$$

The condition of the canted angle θ is obtained to minimize the coupling energy $E(\theta)$ as

$$\tan\theta = \frac{D}{2|J_1|}. \tag{1.6}$$

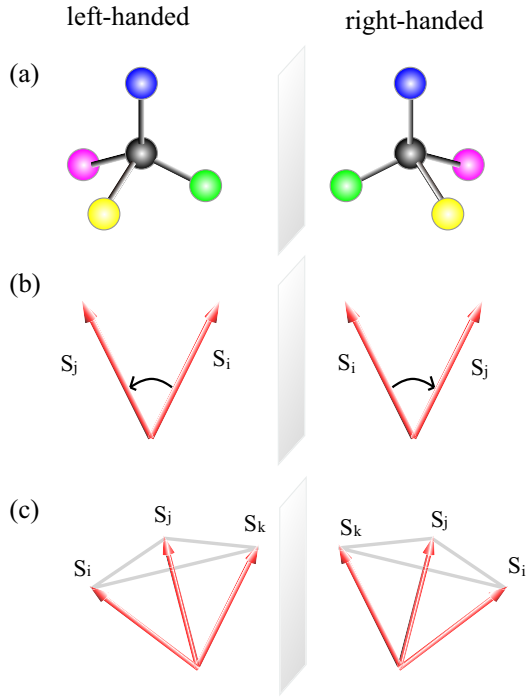

Figure 1.1: Schematic illustrations of the left- and the right-handed chiralities in following categories: (a) chiral molecules (optical isomers); (b) a local vector chirality; (c) a local scalar chirality.

It implies that a canted spin configuration is stabilized with the angle determined by the ratio of D to $|J_1|$. If the antiparallel DM vector $\boldsymbol{D}$ and $-\boldsymbol{D}$ of the DM interaction between the N. N. spins are lined alternately, the canted antiferromagnetic state should arise because spins are canted alternate directions from the antiferromagnetic configuration expected when $\boldsymbol{D} = 0$ and give rise to the ferromagnetic component of the ordered moment in perpendicular direction (see Fig.1.2 (b)). On the other hand, if the parallel DM vector $\boldsymbol{D}$ are lined and the symmetric interaction is ferromagnetic ($J > 0$), the helical structure with constant spin rotate angle is stabilized(see Fig.1.2 (a)). The helical structure stabilized by the DM interaction have a single right- or left-handed helicity in the whole body because the DM interaction breaks the symmetry of the vector chirality. The helicity is determined by the direction of the DM vector. For example, MnSi and $Cr_{1/3}NbS_2$ are well known helical magnets with the helical structure of the single helicity[15, 16]. The helicities in these materials were identified by the polarized neutron scattering experiments

[17, 18]. In short , the DM interaction under the specific lattice symmetry distorts the spin structure and stabilizes the chiral orders.

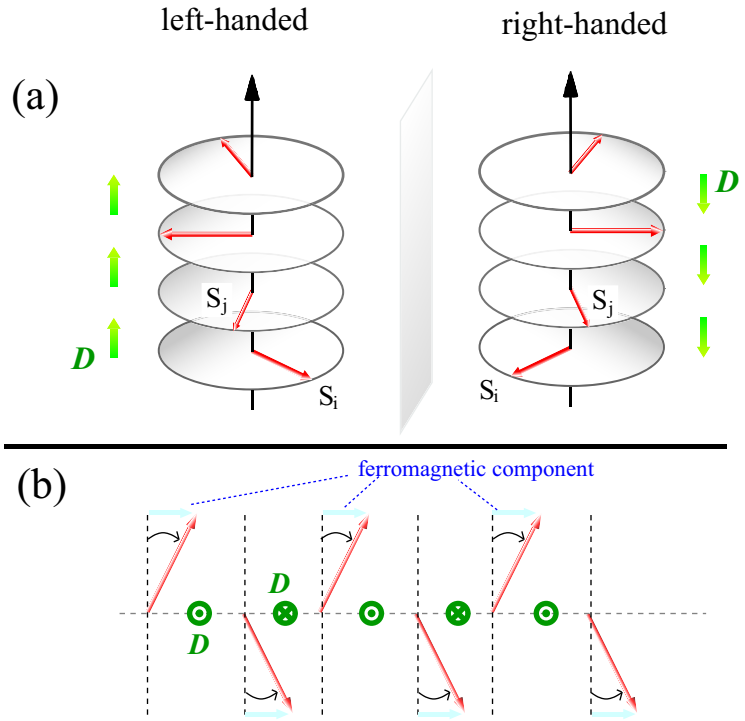

Figure 1.2: (a) Schematic illustrations of the left- and the right-handed helical structures. They are the ferro-chiral ordered states of the vector chirality.(b) Schematic illustrations of the canted antiferromagnetic structure. It is one of the antiferro-chiral orders. The thick green arrows in (a) and (b) represent the DM vector $\boldsymbol{D}$ stabilizing these chiral orders.

Recently, an inverse effect of the DM interaction, namely, the spin chirality distorts the lattice via the DM interaction and causes the consequent ferroelectric polarization, has been investigated in maultiferroic materials[9]. The electric polarization $\boldsymbol{P}_{ij}$ induced by the inverse effect of the DM interaction is related to the vector chirality $\boldsymbol{\chi}_{ij}$ by

$$\boldsymbol{P}_{ij} \propto \boldsymbol{e}_{ij} \times (\boldsymbol{S}_i \times \boldsymbol{S}_j) = \boldsymbol{e}_{ij} \times \boldsymbol{\chi}_{ij} \tag{1.7}$$

where $\boldsymbol{e_{ij}}$ is the unit vector along the direction from the sites i to j [19]. Eq.1.7 means that the vector chirality can induce the electric polarization and vice versa.

The multiferroic state where the ferro-chiral order and the ferroelectric order coexist is realized by this effect. The epoch-making experiment is the discovery of the spin helicity reversal by applying the electric field[11]. $TbMnO_3$ exhibits the helical ordered state below $T_h = 27$ K. The neutron scattering experiment clearly shows that the helicity is controlled by applying the small electric field. Inversely, the simultaneous ferroelectric polarization flop with the transform of the magnetic structure induced by the magnetic field was observed in $MnWO_4$[9]. In this case, the ferroelectric polarization is flopped by the transformation of the vector chirality by applying the magnetic field via the inverse effect of the DM interaction. Figure 1.3 shows the schematic image of this phenomena[20].

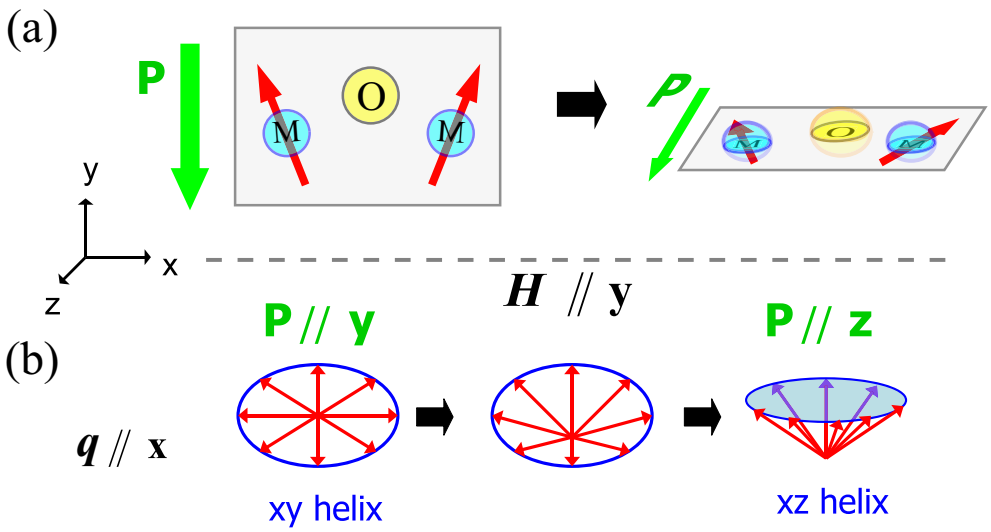

Figure 1.3: Schematic views of the ferroelectric polarization flop by applying magnetic field. (a) The local relation between the configuration of the Mn- and O-atoms and the directions of the Mn-spins. The direction of the local electric polarization is settled by the configuration of the O-atom. (b) Transformation of the helical spin structure by applying the magnetic field. The helical plane is rotated from the xy-plane to the xz-plane when the magnetic field is applied along the y-direction. Consequently, the electric polarization $\boldsymbol{P}$ flops from the y-direction to the Z-direction.

I discovered novel chiral structures originating from the DM interaction in classical metallic magnet MnP. In addition, I was observed a quite peculiar temperature hysteresis phenomena in the chiral ordered phase. It can result from the distortion of the lattice induced by the vector chirality, that is, the inverse effect of the DM

interaction. In several magnets with the vector chirality, helical magnets, the inverse effect of the DM interactions was observed, however, the effect had not been reported in metals yet. Our observation can be the first observation of the inverse effect of the DM interaction in the metallic system. In sec. 1.2, the physical properties of MnP previously reported are described.

1.2 Crystal structure and magnetic properties of MnP

Manganese phosphide MnP is a well known metallic magnet which exhibits a helical magnetic phase at low temperature and has been studied from 1960's[21]. The crystal structure of MnP is an orthorhombic one as shown in Fig.1.4 and its space group is Pbnm. The lattice parameters are a = 5.916 Å, b = 5.260 Å and c = 3.173 Å. The c-axis is easy-magnetization direction. The b- and a-axis are the intermediate- and hard-magnetization directions, respectively.

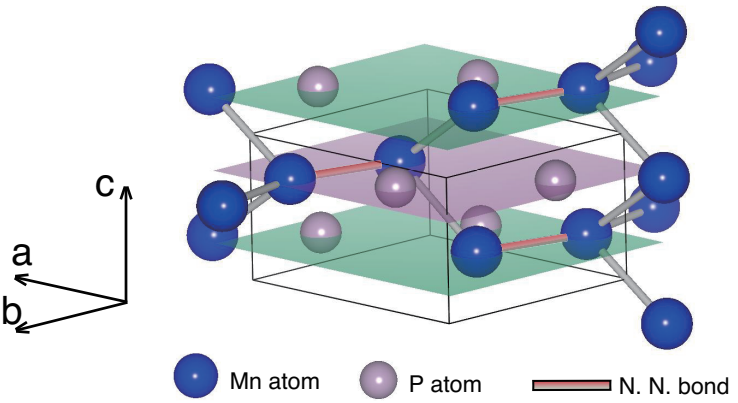

Figure 1.4: The crystal structure of MnP.

The magnetic properties of MnP have been investigated by many researchers and many intriguing phenomena, such as the complex magnetic phase diagram in magnetic field [21, 22, 23, 24, 25, 26, 27], the magnetocaloric effect [28] and the Lifshits critical behavior in magnetic field [29, 30, 27, 31, 32, 33, 34], were found. In particular, the magnetic structures and the critical phenomena in the magnetic field along each axis had been extensively investigated. In zero external field, the ferromagnetic phase transition is undergone at $T_{\mathrm{C}} = 292$ K, where the spins are

parallel to the c-axis [21, 22]. Below $T_{\rm N} = 47$ K, the magnetic structure transforms into the helical structure with the magnetic propagation vector $\boldsymbol{\delta} = (\delta, 0, 0)$ with $\delta \simeq 0.117$, in which the spins lie in the bc-plane. Although the helical plane is perpendicular to the propagation vector, it is reported that the helical structure of MnP is not a simple proper type one but a double-spiral-type one as shown in Fig.1.5 [22, 23, 26]. Figure.1.6 shows the schematic view of the magnetic structures in zero magnetic field. Figure. 1.7, 1.8 and 1.9 show magnetic phase diagrams in the magnetic field H along the c-, b- and a-axes, respectively. The size of magnetic ordered moment was estimated by the magnetization measurements and the neutron scattering experiments about $1.3\mu_{\rm B}$ /Mn-atom [21, 26]. The electronic specific heat coefficient γ was reported as relatively large valuein d-metals, being 9.65 mJ mol^{-1} K^{-2} [35].

It is a controversial issue whether MnP should be treated as a localized spin system or an itinerant electron magnet. The size of the magnetic moment in the ordered phases and the γ value are explained by numerical works with the assuming the itinerant mixing band of Mn-$3d$ and P-$3p$ electrons[36, 37]. On the other hand, most magnetic properties are explained by the s-d model with assuming the localized Mn $3d$ moments. For example, the temperature dependence of the magnetization and spin-wave dispersion relation observed by the neutron scattering experiments are well described by the Heisenberg Hamiltonian with assuming the RKKY type long-range interaction[38, 39, 40]. Magnetic properties in a strong itinerant magnet such as Fe are well descrived by the Heisenberg-type localized spin model. MnP is considered to be in this category. In this thesis, therefore, I discuss on the magnetic properties of MnP on a basis of the localized spin model.

As mentioned above, MnP exhibits the complicated $H - T$ magnetic phase diagram. The stabiliy of the various magnetic phases in zero and finite magnetic fields are explained by the competition between the ferromagnetic and the antiferromagnetic interactions[41, 42, 34]. For example, the stability of the double helical structure observed in zero magnetic field is explained theoretically by considering from the N. N. interaction to the 7th N. N. interaction[41]. The nature of such a helical phase is different from that of the helical phase induced by the DM interaction. The helical phase of MnP, therefore, for instance both handed helicity domains coexist, in contrast to that in MnSi. In polarized neutron experiments, the reflections from the both handed helicity domains were observed actually[24].

Recently, a novel transition was observed at $T^* = 282$ K being about 10 K lower than ferromagnetic transition temperature $T_{\rm C}$ by Becerra in the AC susceptibility measurement at very low field [43]. He suggested that the transition at T^* is a spin reorient transition; namely, the ferromagnetic ordered moment slightly inclines toward the b-axis from the c-direction below T^*, and that the angle of inclination become lower with decreasing temperature and the ferromagnetic ordered

moment go back to the c-direction around T_N. However, further investigations on the novel phase had never reported, and the nature of the phase is still unclear. Considering the crystal structure of MnP as shown in Fig.1.4, the DM interaction can act between the N. N. Mn-spins because the inversion symmetry at the center of the N.N. Mn-sites is lack. However, no influence of the DM interaction has not ever been found.

The aims of this study are to illuminate the nature of the novel phase below T^* and to hunt for tracks of the DM interaction in MnP.

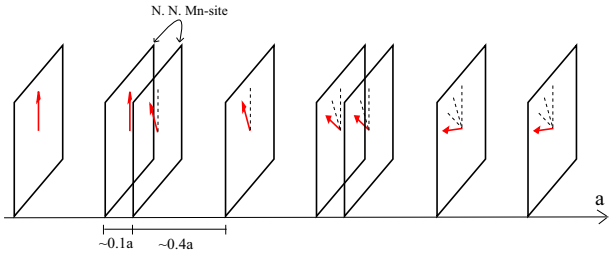

Figure 1.5: The schematic illustration of the double spiral type helical structure in MnP[22].

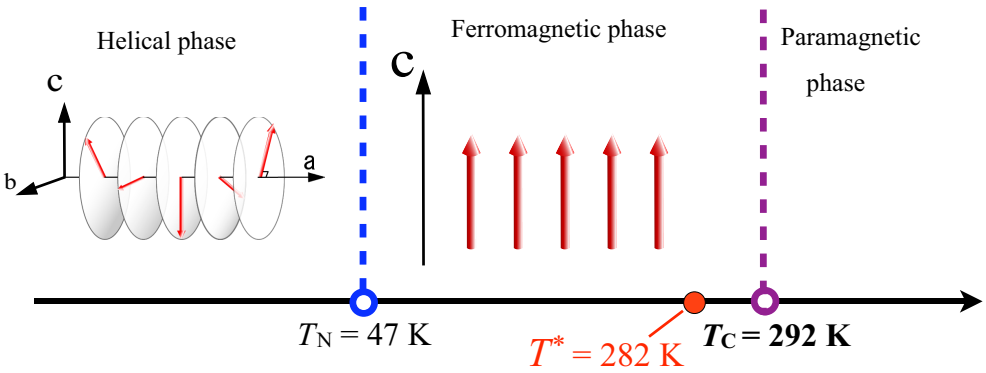

Figure 1.6: The schematic view of the temperature dependence of the magnetic strucutre in MnP.

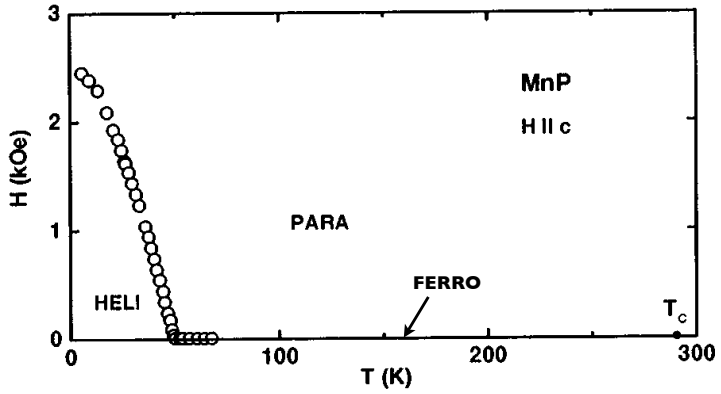

Figure 1.7: $H - T/$ magnetic phase diagram in MnP with the magnetic field along the c-axis. "PARA", "FERRO" and "HELI" represent the paramagnetic, the ferromagnetic and the helical phases, respectively [21].

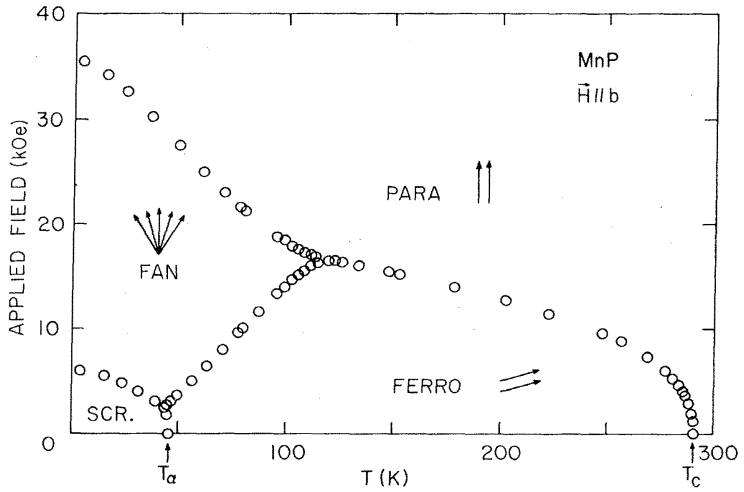

Figure 1.8: $H - T$ magnetic phase diagram in MnP with the magnetic field along the b-axis. "FAN" and "SCR" represent the magnetic phase with the fan-like spin arrangement and the helical phase, respectively [30].

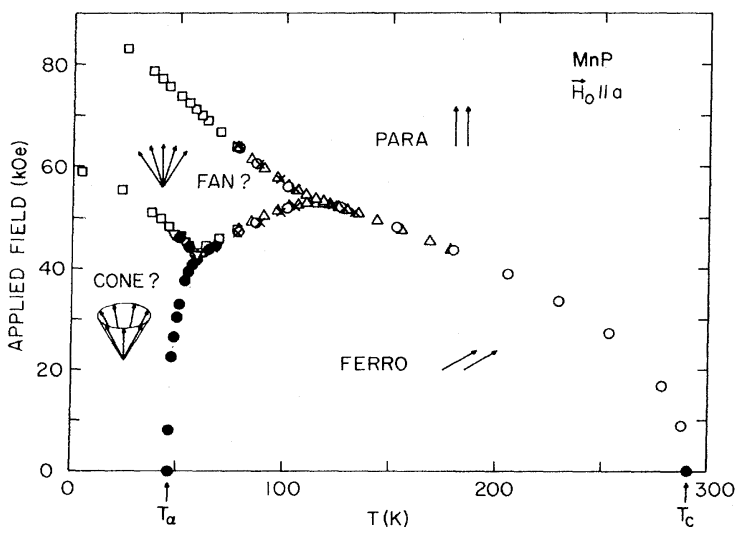

Figure 1.9: $H - T$ magnetic phase diagram in MnP with the magnetic field along the a-axis. "CONE" represents the magnetic phase where the spins incline toward the a-direction with keeping the helical arrangement of their bc-plane component [31].

Chapter 2

Experimental procedures

2.1 Sample preparations

The single crystalline samples were grown by the temperature gradient furnace technique as following Ref. [21]. Pure Mn pieces and pure P pieces were located at the either sides of the evacuated quartz tube (see Fig. 2.1 (a)). The sequences of the controlled temperatures at the Mn-side and P-side were shown in Fig. 2.1 (b). As increasing temperature, phosphorus pieces evaporate and the phosphorus vapor reacts with the manganese pieces to MnP. The single crystal is grown when the Mn-side temperature is decreasing slowly. The vapor pressure of P is a problem because it might break quartz tube at high temperature. In order to prevent it, the thick quartz tube with the thickness of 2 mm was used and the P-side temperature keep lower than 400 °C. The manganese pieces with the purity of 3N were purchased from Nacalai tesque Co., Ltd. and the phosphorous pieces with purity of 6N were purchased from Kojundo Chemical Laboratory Co., Ltd..

For evaluation of the sample, the X-ray powder diffraction (XRD) was performed by using a commercial diffractmeter (Rigaku, Mini-Flex). The powder samples were obtained by crushing pieces of the single crystal. No additional peaks originating from 2nd phases of the XRD was observed in all samples used for the experiments. A typical result of the XRD is shown in Fig.2.2. The ferromagnetic transition temperature T_{C} and the helical magnetic phase transition temperature T_{N} obtained from the magnetization measurements, mentioned later, were agreement with those reported previously, which also warrants the sample quantity. In addition, the residual resistivity ratio (RRR) is estimated at about 83 from resistivity measurements. The high value of the RRR indicates a good quality of the sample from the viewpoint of defects and impurities. The crystallographic axes of the single crystals were determined by the X-ray back Laue method by using

the apparatus (SHIMADZU, XD-3A) installed at Inui laboratory in Depertment of Materials Science and Engineering at Kyoto university. The powder sample for the neutron powder diffraction experiments was obtained by crushing the single crystal as well as that for the XRD.

The list of the size and the shape of typical samples used for the experiments is shown in Tab. 2.1. The single crystal samples were cut by using a commercial speak cutter (Sankyo Engneering Co., Ltd., 5T-2C) at Inui laboratory. In order to check the sample dependence of the properties, I performed the same measurements for several samples in each experiment, and hardly found the sample dependent behaviors. Hence, only experimental results by using the samples listed in Tab. 2.1 are shown in this thesis.

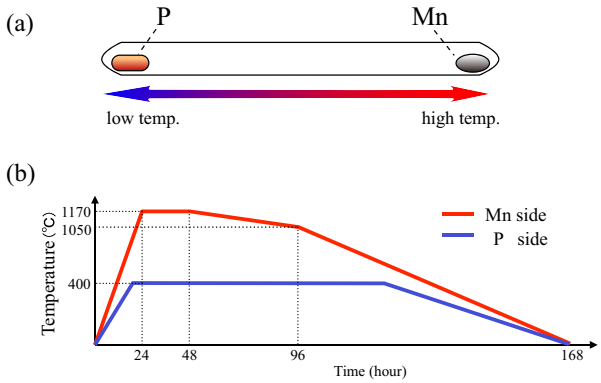

Figure 2.1: (a) The schematic illustration of the position of the Mn and P in the evacuated quartz tube. (b) The time-sequences of the temperatures at the Mn-side and the P-side.

Table 2.1: The sample list of MnP used for each experiment.

sample neme	experiment	a (mm)	b (mm)	c (mm)	weight (mg)
#1	magnetization // a-axis	2.5	0.9	0.7	6.0
#2	magnetization // b-axis	0.7	2.5	1.0	7.0
#3	magnetization // c-axis	0.7	0.6	2.5	2.8
#4	magnetization // c-axis	0.5	2.6	2.6	15.1
#5	resistivity, specific heat capacity	2.36	0.80	0.49	5.1
#6	neutron (single)	6.1	3.6	9.6	762.6
#7	neutron (powder)	-	-	-	3.6×10^3

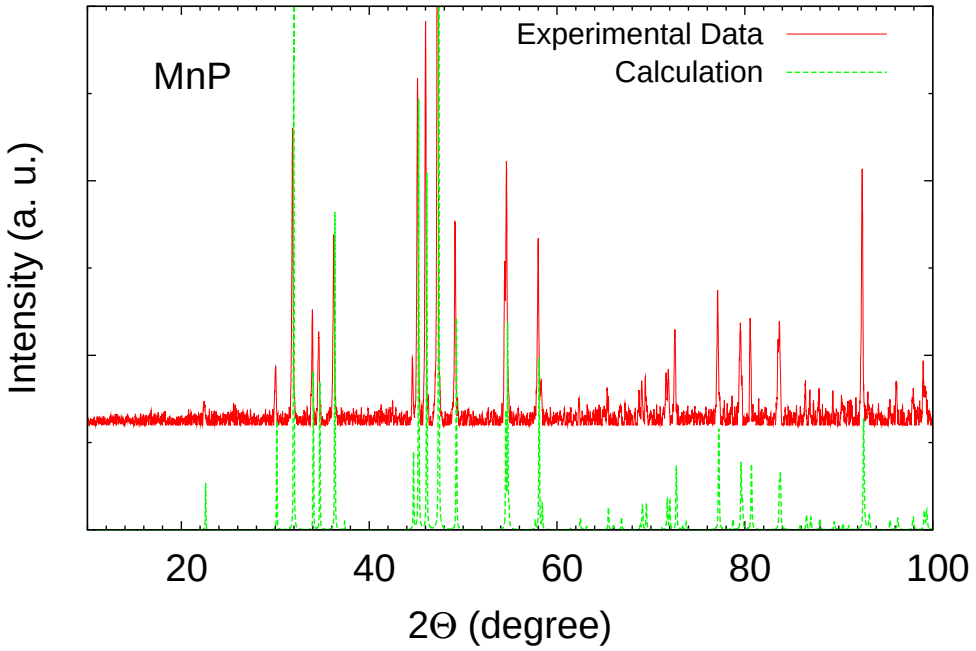

Figure 2.2: The experimental (red line) and the calculation (greenline) of the X-ray powder diffraction for MnP

2.2 AC- and DC-magnetization measurements

AC- and DC- magnetization measurements were performed by using three commercial SQUID-magnetometers (Quantum Design, MPMS-1T, 5T and 5.5T) installed at Research Center for Low Temperature and Materials Sciences in Kyoto university. A SQUID magnetometry is one of the most effective and the most sensitive apparatus for measuring magnetic properties. The term of SQUID is an abbreviation for Superconducting QUantum Interference Device, which is a superconducting ring containing a thin part of the insulator, being the Josephson junction. When one put the SQUID into the magnetic field, the magnetic flux can come into the superconducting ring through the insulator junction. The magnetic flux in the superconducting ring is quantized to integral multiples of the magnetic flux quantum $\Phi_0 = hc/2e$. Therefore, we can measure the magnetization with ultra high resolution of Φ_0 by using SQUID system.

The principle of the measurement by the SQUID magnetometer is schematically shown in Fig. 2.3 The DC-measurement is performed by the pick-up method. The sample is magnetized in the DC magnetic field H generated by a superconducting magnet. When the sample is moving in the pick-up coil from the to bottom to top, the variation of the flux, which is caused by the movement of the sample, generates the screening current in the pick-up coil. The screening current is finally detected by the rf-SQUID through the signal coil. Figure 2.4 shows a typical signal of the SQUID in the DC magnetization measurement. In the AC-measurements, the AC magnetization $M(t)$ was induced by applying the AC magnetic field $h(t) = h_{\rm AC}\cos(\omega t)$ with frequency ω generated by the AC primary coil. Because an induced magnetization of a sample by the AC field is time-dependent, the screening current proportional to the time differential of the magnetization dM/dt is generated in the pick-up coil even when the sample is at rest, The screening current is finally detected by the rf-SQUID as well as done in the DC-measurements. The background signal obtained when the sample is taken out from the pick-up coil completely is subtracted. Figure 2.4 shows a typical signal of the AC-magnetization measurement against the phase of the AC magnetic field.

When the amplitude of the AC magnetic field is small enough, the AC magnetization $M(t)$ is proportional to the AC magnetic field $h(t)$. Because a response to a time-dependent field can have some time-delay, the AC magnetic response $M(t)$ to $h(t)$ is written as $M(t) = M_0\cos(\omega t - \phi)$ with a phase shift ϕ. The phase shift of the AC magnetic response is obtained by considering a complex susceptibility $\chi = \chi' - i\chi''$ at the frequency of ω. By using the complex susceptibility, the AC magnetic responses described with the real part M' and the imaginary part (delay

component) M'' as

$$M(t) = M' \cos(\omega t) + M'' \sin(\omega t), \tag{2.1}$$

where $M' = \chi' h_{\rm AC}$ and $M'' = \chi'' h_{\rm AC}$. The real part of the AC susceptibility is asymptotically identified with the DC susceptibility $\chi' \to \chi_{\rm DC}$ in the limit of $\omega \to 0$. The imaginary part of the AC susceptibility χ'' is called also the dissipation part because of related to the energy dissipation, and is 0 at $\omega = 0$.

In the conditions where the magnetization $M(t)$ is not proportional to the magnetic field $h(t)$, for instance in the high AC-field region and in the vicinity of the magnetic phase transition, the higher order terms of $h(t)$ such as $h(t)^n$ needs to be considered. Considering the time reversal symmetry, the magnetization is written as a function of the magnetic field $h(t)$ as

$$M(t) = \chi_0 h(t) + \chi_2 h^3(t) + \chi_4 h^5(t) + \cdots, \tag{2.2}$$

where χ_0 is a linear susceptibility and $\chi_2, \chi_4, \cdots$ are nonlinear susceptibility. All of $\chi_0, \chi_2, \chi_4, \cdots$ should be complex at a finite frequency. Then the AC magnetic response $M(t)$, which consists of the real and the imaginary components, $M'_{2n}(t)$ and $M''_{2n}(t)$, of various frequencies can be rewritten as

$$M(t) = \sum_{n=0}^{\infty} [M'_{2n} \cos((2n+1)\omega t) + M''_{2n} \sin((2n+1)\omega t)] \tag{2.3}$$

where ${M_0}' = \chi'_0 h_{\rm AC} + \frac{3}{4}\chi'_2 h^3_{\rm AC} + \cdots$, ${M_0}'' = \chi''_0 h_{\rm AC} + \frac{3}{4}\chi''_2 h^3_{\rm AC} + \cdots$, ${M_2}' = \frac{1}{4}\chi'_2 h^3_{\rm AC} + \frac{5}{16}\chi'_4 h^5_{\rm AC} + \cdots$ ${M_2}'' = \frac{1}{4}\chi''_2 h^3_{\rm AC} + \frac{5}{16}\chi''_4 h^5_{\rm AC} + \cdots$. And an induced voltage in a secondary coil is given by

$$\begin{aligned} E &\propto \frac{dm(t)}{dt} \\ &= \omega h_{\rm AC}[-{\chi_0^t}' \sin(\omega t) + {\chi_0^t}'' \cos(\omega t)) - 3{\chi_2^t}' \sin(3\omega t) + 3{\chi_2^t}'' \cos(3\omega t) + \cdots] \end{aligned} \tag{2.4}$$

where $\chi_0^t = M_0/h_{\rm AC}, \chi_2^t = M_2/h_{\rm AC}, \cdots$. If $h_{\rm AC}$ is small enough, we can consider as $\chi_0^t \sim \chi_0$, $\chi_2^t \sim \chi_2$, $\cdots$. Thus the higher order forms of $M(t)$, the nonlinear susceptibilities can be measured as the response with the frequency of $3\omega, 5\omega, \cdots$ in the AC susceptibility measurements.

The nonlinear susceptibilities can be measured by other technique. If the DC field H is applied, the DC magnetization M is written as

$$M = \chi_0 H + \chi_2 H^3 + \chi_4 H^5 + \cdots, \tag{2.5}$$

and the nonlinear susceptibilities are obtained directly by the DC magnetization measurements. When the AC field is applied with the DC field, χ' can be treated as the differential magnetization and given by

$$\chi' \simeq \frac{dM}{dH} = \chi_0 + 3\chi_2 H^3 + \chi_4 H^5 + \cdots , \tag{2.6}$$

in the condition of $h_{\rm AC} << H$ and $\omega \to 0$. Hence, we can obtain the nonlinear susceptibility χ_2 from the slant of the observed χ' vs H^2 plots in the limit of $H^2 \to 0$.

In this study, the AC- and the DC-magnetization measurements were performed in the temperature range from 5 K to 350 K. The DC magnetic field range is 0 - 55 kOe. In this study, the detailed magnetization measurements in very low field, therefore is necessary, residual field in the sample space need to be suppressed as low as possible. To achieve it, I estimated the residual field in the sample space from the magnetization measurements at paramagnetic temperature of 350 K by regarding an applied field when a measured magnetization is zero as being residual field. The zero field environment of $H < 0.3$ Oe was made by compensating the residual field by the superconducting magnet. The magnitude of the applied field which is generated by the superconducting magnet is controlled with high resolution of $\delta H \leq 0.1$ Oe in the measurement system.

I performed the AC magnetization measurements in the AC field range of 0.1 Oe $< h_{\rm AC} <$ 3.0 Oe and frequency range of 0.1 Hz $< f <$ 1000 Hz.

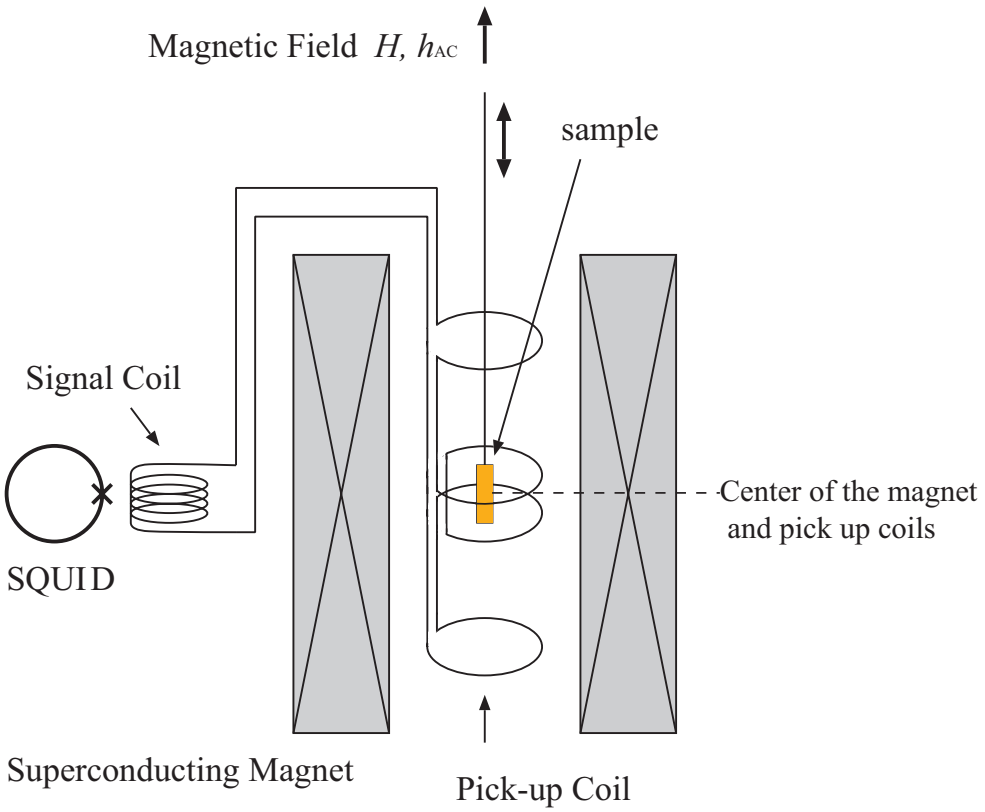

Figure 2.3: Schematic view of the SQUID magnetometer.

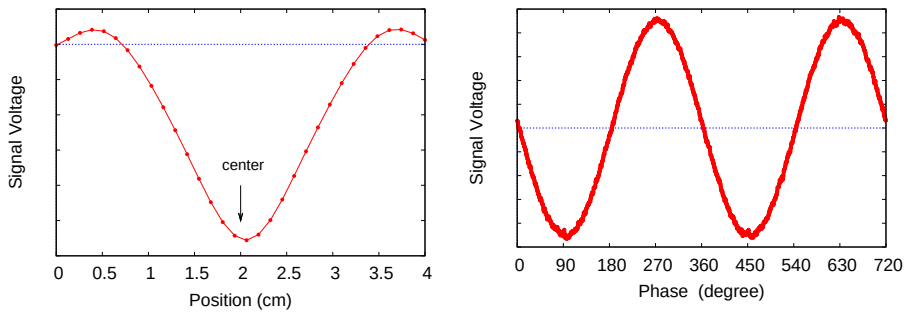

Figure 2.4: Typical signals of the SQUID in the DC (left) and the AC (right) magnetization measurements.

2.3 Resistivity measurement

The electric resistivity was measured by the four terminal method. The electric current of $I = 10$ mA is generated by using the commercial current source (ADVANTEST, R6142) and the excited voltage is measured by using the commercial nanovoltmeter (KEITHLEY, 2182A/J). The sample was cooled by the GM refrigerator and measurements were performed every 30 seconds with sweeping the temperature in the range from 9 K to 310 K. The sweep rate of the temperature is 0.3 K/min. In order to make out whether the temperature hysteresis is or not, the measurements in both the warm-up and the cool-down process were carried out with the sweep rate of 0.1 K/min in the temperature range around the magnetic transition temperatures of 40 K $< T <$60 K and 270 K $< T <$ 310 K .

2.4 Specific heat measurement

The specific heat was measured by using the thermal relaxation-method apparatus of PPMS (Quantum Design) installed at Kindo laboratory in Institute for Solid State Physics (ISSP), University of Tokyo. The measurements were performed in the temperature range from 5 K to 350 K in the warm-up process and the cool-down process.

2.5 Neutron scattering experiment

2.5.1 Single crystal neutron scattering experiment by using the triple-axis spectrometer

The neutron is the electrically neutral particle with a spin $S = 1/2$ and a magnetic moment $\mu_{\rm n} = -1.9132\mu_{\rm N}$ ($\mu_{\rm N}$ is the nuclear magneton). The neutron interacts with nuclei via the strong nuclear force and with magnetic moments via the electromagnetic force. By using the neutron with the wavelength of the same order of the interatomic distance in the condensed matters, about a few Å, we can know their crystal structure and their magnetic structure by analyzing the diffraction pattern. In addition, the energy of the neutron with such a wavelength is between a few meV and tens meV, which is the same order of the elementary excitation energy in the condensed matters, hence, we can also observe the dynamical structure such as the phonon and the magnon by the inelastic neutron scattering experiments. The neutron scattering experiments, therefore, the most poweful technique in the condensed matter science.

The neutron scattering experiments for the single crystal were performed by the triple-axis spectrometer PONTA of the Institute for Solid State Physics (ISSP-PONTA) and ISSP-HER installed at JRR-3M reactor in Japan Atomic Energy Agency (JAEA).

Figure 2.5 shows the schematic view of the triple-axis spectrometer. The triple-axis spectrometer is the most general instrument for the neutron scattering experiments. In the triple-axis spectrometer, the stages of the monochromator, the sample and the analyzer can rotate independently, and we can obtain the neutron scattering function $S(Q, \omega)$ of the optional momentum transfer Q and the optional energy transfer ω.

The incident white neutron beam from the nuclear reactor collimated by the 1st collimator is monochromatized by the Bragg diffraction of the monochromator crystal. The wavelength of the monochromatized neutron λ is determined by the Bragg condition

$$2d \sin \theta_{\mathrm{M}} = n\lambda, \tag{2.7}$$

where d is the reflection-plane spacing of the monochromator and $2\theta_{\mathrm{M}}$ is the diffraction angle. The monochromatized neutron comes to the sample through the 2nd collimator. Scattering at any scattering vector in the 2-dimensional reciprocal lattice space can be observed by adjusting the vertical rotation angle of the sample stage ω and the scattering angle to the analyzer 2θ. The neutron beam scattered from the sample is collimated by the 3rd collimator and its the energy distribution is analyzed by the Bragg diffraction of the analyzer crystal. Finally the analyzed neutron collimated by the 4th collimator is detected.

At the ISSP-PONTA and the ISSP-HER, the (002) plane of the pyrolytic graphite (PG) is used for the monochromator and the analyzer. Only the elastic scattering experiments ($k_i = k_f$) were done with the condition of $2\theta_{\mathrm{M}} = 2\theta_{\mathrm{A}}$ in this study. The ISSP-PONTA is installed in the reactor room. The ISSP-HER is the cold neutron triple-axis spectrometers installed in the guide hall, where the monochromator is placed in the neutron guide tube without the 1st collimator. The biggest difference between these spectrometers is the neutron wavelength (energy). In this study, the wavelength of $\lambda = 1.64$ Å, 2.36 Å and 2.44 Å ($E_i = 30.5$ meV, 14.7 meV and 13.7 meV) were selected in the experiments at the ISSP-PONTA, whereas that of $\lambda = 4.04$ Å and 4.33 Å ($E_i = 5$ meV and 4.36 meV) were selected in the experiments at the ISSP-HER. The combinations of the collimators were open-40'-80'-80' in the experiments at the ISSP-PONTA and guide-open-80-80 in the experiments at the ISSP-HER. When the PG is used for the monochromator, the higher order reflection of the wavelength of $\lambda/2$, which is the (004) reflection, is contaminated unavoidably. In order to eliminate it, the appropriate fillers for the neutron wavelength should be used. The PG filter and the Be filter were used in

the experiments at the ISSP-PONTA and at the ISSP-HER, respectively.

The sample was mounted with its c-axis verticaly in the Al holder so that the (hk0) plane was the scattering plane. The GM refrigerator was used for cooling the sample, and the experiments were performed in the temperature range of 9 K $\leq T \leq$ 305 K.

2.5.2 Neutron powder diffraction experiment

The neutron powder diffraction experiments were performed by using the the KINKEN powder diffractometer, HERMES, of Institute for Materials Research (IMR) Tohoku university installed at the JRR-3M reactor in JAEA. Figure 2.6 shows the schematic view of the neutron powder diffractometer HERMES. The neutron beam monochromized by the PG monochromator comes to the sample through the guide tube. Since the 150 the ^{3}He detectors are lined with 1 degree intervals, we can perform the high efficient measurement in the wide angle range. For example, we can obtain the data at every 0.1 degree in the range of 150 degree only by the 10 times measurements with steps of 0.1 degree. The neutron wavelength for powder diffraction experiments was 1.84843 Å.

The powder sample was put into a cylindrical Vanadium (V) can with the size of 7 mm $\phi\times$ 25 mm. V is a suitable material to the sample can for the neutron powder diffraction experiments because its coherent scattering length is very small which is $b_{coh} = -0.3824$ fm, and hence, unnecessary Bragg reflections hardly arise. The GM refrigerator is used for cooling the sample, and the experiments were performed in the temperature range of 10 K $\leq T \leq$ 300 K.

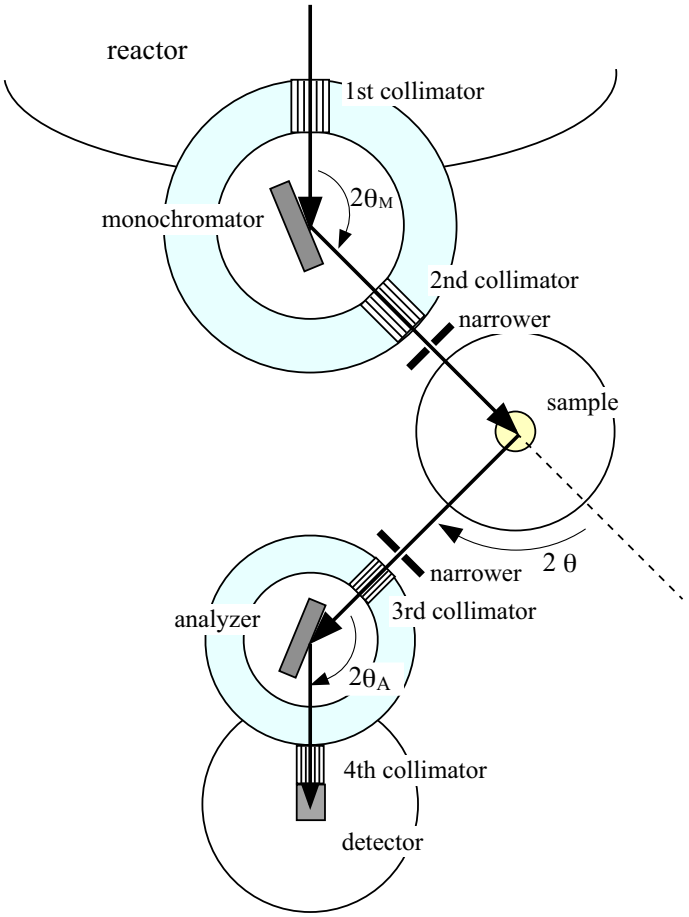

Figure 2.5: The schematic view of the triple-axis spectrometer. In the text, the combination of the horizontal collimators is expressed with the notation of "1st-2nd-3rd-4th".

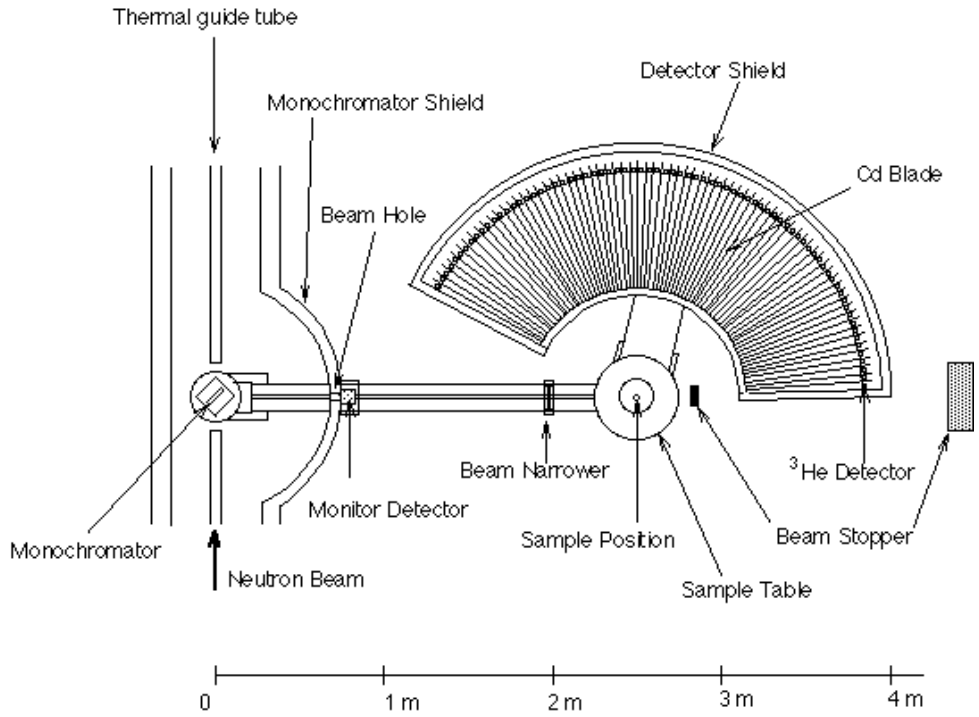

Figure 2.6: The schematic view of the neutron powder diffractmator, HERMES.

Chapter 3

Experimental results and analyses

3.1 AC- and DC-magnetizations

3.1.1 Magnetization along the b-axis

Figure3.1 shows the temperature dependences of the real and the imaginary parts of the AC susceptibility χ' and χ'' with the AC field applied along the b-axis. The AC susceptibility was measured in the following three measurement-processes:

(a) the cool-down process from 350 K;

(b) the warm-up process after cooling the sample to 100 K which is the temperature above T_{N};

(c) the warm-up process after cooling the sample to 5 K which is the temperature below T_{N}.

The AC field with the amplitude of $h_{\mathrm{AC}} = 0.5$ Oe and the frequency of $f = 10$ Hz was applied in these measurements. In all processes, sharp increases of χ' and χ'' are found around $T^* = 282$ K. Interestingly, the peaks at T^* in the process (c) is much higher than those in the process (a) and (b). This process-dependent behavior will be discussed later with including the detailed investigation of the DC magnetization measurements. The divergent behaviors of χ' and χ'' in the process (c) indicate a second order magnetic phase transition at T^*. The peaks of the AC susceptibilities at T^* are much sharper than those observed by Becerra [43]. This discrepancy may come from the difference of the AC-field amplitude, he

measured with the AC-field of $h_{\mathrm{AC}} = 2$ Oe. To verify it, we checked the AC-field dependences of χ' and χ'' and found strong suppression of the peaks at T^*.

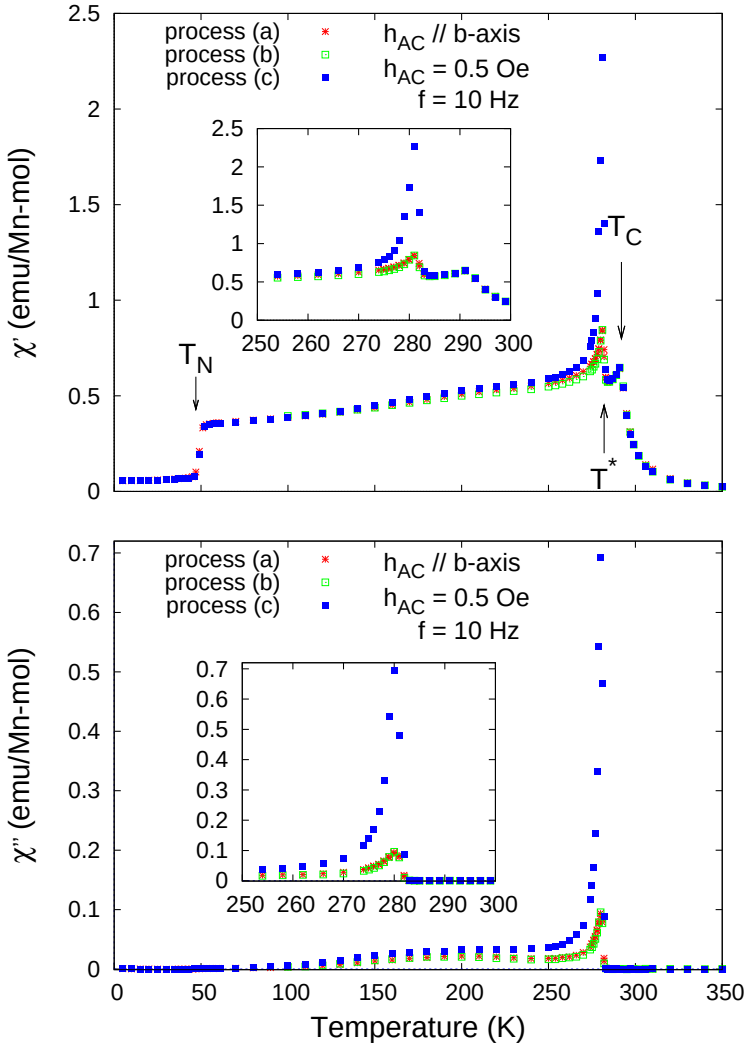

Figure 3.1: Temperature dependences of the AC susceptibilities of MnP in the various processes. The upper figure and the lower one show the real part and the imaginary part of the AC susceptibility, respectivelly. The details of the measurement processes (a)-(c) are described in the text.

The temperature dependences of the DC magnetization along the b-axis in several measurement processes are shown in Fig. 1(b). The measurements were performed in different four T-processes after applying a field of 3 Oe at the paramagnetic temperature 350 K:

(A) the cool-down process from 350 K;

(B) the warm-up process after cooling the sample down to 55 K which is the temperature above $T_{\rm N}$;

(C) the warm-up processes after cooling the sample down to 5 K which is the temperature below $T_{\rm N}$

(D) the warm-up processes after cooling the sample down to 35 K which is the temperature below $T_{\rm N}$

A sharp increase of the magnetization at T^* was observed in any processes, however, the magnetization in the temperature range of $T_{\rm N} < T < T^*$ remarkably depends on the processes. The magnetizations in the processes (A) and (B) and those in (C) and (D) are almost same, respectively. On the other hand, the magnitudes of the magnetization in the latter processes, in which the sample has been once cooled below $T_{\rm N}$, are about three times larger than those in the former processes, in which the sample has not been cooled below $T_{\rm N}$. These results indicate a quite peculiar temperature hysteresis, namely, the magnetization in the state for $T_{\rm N} < T < T^*$, intermediate-temperature phase, strongly depends on whether the sample has undergone to the helical phase below $T_{\rm N}$ once or not. This process-dependent behavior of the magnetization was found only in the intermediate-temperature phase. The magnetizations in the four processes almost collapse in the low temperature helical phase ($T < T_{\rm N}$) and in the paramagnetic phase ($T > T_{\rm C}$). In the high temperature phase for $T^* < T < T_{\rm C}$ though the very small differences are found as shown in the inset of Fig.3.3, which will be fully described below.

The observed temperature-dependent behaviors of the magnetization naturally arise the following question; what temperature do we need to warm up the sample to, for restoring the sample to the state before cooling it down to the helical phase? In order to investigate it, I performed the following measurements. The sample was cooled down to 5 K once and warm up to the returning point (R.P.). After this procedure, the sample was cooled down to 250 K and the magnetization was measured in the warm-up process. If the state of the sample is restored at the R.P., we find the small magnetization corresponding to those in the process (A) and (B). Otherwise, the large magnetization corresponding to those in the process (C) and (D) is found. The selected R.P. were 270 K, 287 K, 300 K, 320 K, 330 K and 350 K. The results

of this measurements were shown in Fig. 3.3. In the figure, we also show the result in the simple warm-up process from 5K. The magnetizations measured in the processes of the 270 K and 287 K are still enhanced, however, the magnetization is restored to the small one when the R.P. is higher than 300 K which is above $T_{\rm C}$. In short, the enhanced magnetization along the b-axis is restored at $T_{\rm C}$. As shown in the inset of Fig. 3.3, the very small difference of the magnetization is also observed in $T^* < T < T_{\rm C}$. Indeed the process-dependece of the magnetization along the b-axis remarkably appears below T^*, but it fundamentally appears below $T_{\rm C}$.

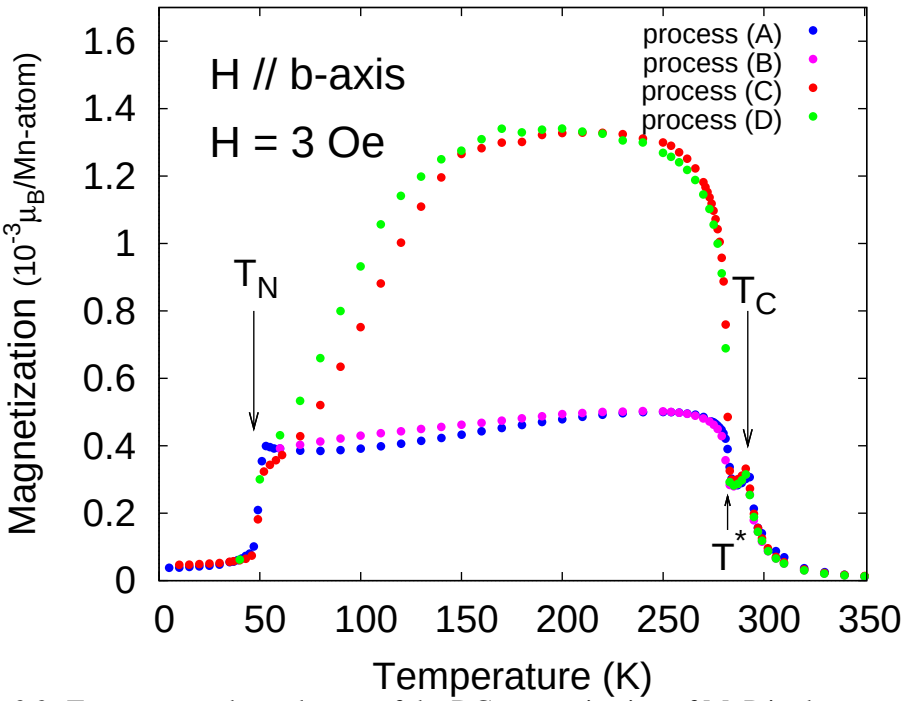

Figure 3.2: Temperature dependences of the DC magnetization of MnP in the various processes. The details of the measurement process (A)-(D) are described in the text.

Figure 3.4 shows the magnetization curves against the magnetic field along the b-axis at $T = 100$ K. In the figure, the data in three different processes to approach the measurement temperature are shown. The three processes are follows:

(A') the sample was cooled from 350 K directly in zero field;

(C') the sample was warmed from 5 K after cooled to 5 K once in zero field;

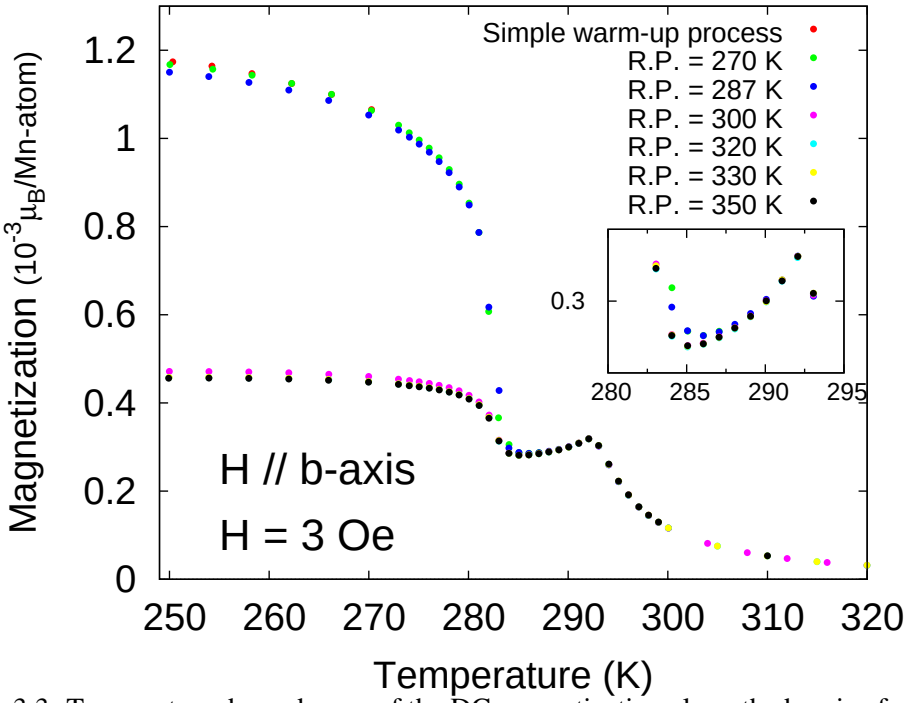

Figure 3.3: Temperature dependences of the DC magnetization along the b-axis of MnP from 5 K and from 250 K after the sample warming up to various returning point (R.P.). The detailed of the measurement process are described in the text

(A") the sample was cooled from 350 K directly in a field of 10 kOe.

The measurements were performed with changing the field in the following sequence: 0 Oe → 30 Oe → -30 Oe → 30 Oe. Ferromagnetic hysteresis loops were observed in all the processes. It indicates that the intermediate-temperature phase is a ferromagnetic one with the very small ferromagnetic moment along the b-axis. The spontaneous magnetization $M_s^{//b}$ and the coercive field H_c exhibit process-dependences. $M_s^{//b}$ in the processes (A') and (B') are about 2 $\times 10^{-4} \mu_B$/Mn-atom and 1 $\times 10^{-3} \mu_B$/Mn-atom respectively, which indicates that the spontaneous magnetization is enhanced five times when the sample has undergone the helical phase before reaching to the measurement temperature. This process-dependent behavior of $M_s^{//b}$ is the same one as that observed in the temperature-dependence of the magnetization shown in Fig. 3.2. It should be noted that the magnetization curves in the processes (A') and (A") nicely collapse on one curve. It clearly indicates that

the magnetic field of 10 kOe, being much higher than the coercive field of about 5 Oe, can not affect the magnetization curve. These magnetization measurements indicate that two magnetic states exist in the intermediate-temperature phase: One is the large magnetization (LM) state and the other is the small magnetization (SM) state. The LM state is realized only by cooling the sample to the low temperature helical phase, not by applying magnetic field. Hence, the LM state does not originate from alignments of the ferromagnetic domains or the ferromagnetic clusters.

In order to determine which state, the LM state and the SM state, is the thermal equilibrium state in the intermediate-temperature phase, I measured time developments of the magnetizations in the LM and the SM states. Figure3.5(a) shows time dependences of the magnetizations at $H = 30$ Oe in the processes (A') and (C'). It should be also noted that the magnetizations in both processes exhibit no time dependences up to 6 hours. I also performed the same measurement at $T = 250$ K, where a thermal relaxation should be more rapid, however, no time dependences were observed up to 16 hours as shown in Fig. 3.5 (b). Therefore, one cannot determine which state is the thermal equilibrium state. No time dependence at $T = 250$ K indicates a high energy barrier between the two states.

Figure 3.6 shows the magnetization curves against the magnetic field along the b-axis at various temperatures. It is shown the results measured in the LM state which were performed after cooling the sample to 5 K once. The ferromagnetic hysteresis and spontaneous magnetization are not found above T^*. I performed the same measurements also in the SM state which were done directly cooling to the measurement temperatures. The temperature dependences of the estimated spontaneous magnetization $M_s^{//b}$ and coercive field $H_{\rm c}$ in the LM and SM states were shown in Fig. 3.7 and 3.8, respectively. Both $M_s^{//b}$ and $H_{\rm c}$ in the LM state are larger than those in the SM state in the intermediate-temperature region. First, we shall describe the manners of the temperature dependences of $M_s^{//b}$ and $H_{\rm c}$ in the LM state. $M_s^{//b}$, which is disappeared below $T_{\rm N}$, sharply increases at $T = T_{\rm N}$, and then gradually increases up to the maximum value around 150 K with increasing $M_s^{//b}$ vanishes at $T = T^*$ not at $T = T_{\rm C}$. $H_{\rm c}$ is also very sharply increase at $T = T_{\rm N}$ and monotonically decreases up to T^*. In the SM state, the manner of $M_s^{//b}$ is similar, in spite of the large difference of its magnitude. $H_{\rm c}$ in the SM state is not so different from that in the LM state above 150 K. The increase of $H_{\rm c}$ below 150 K is modester in the SM state than that in the LM state.

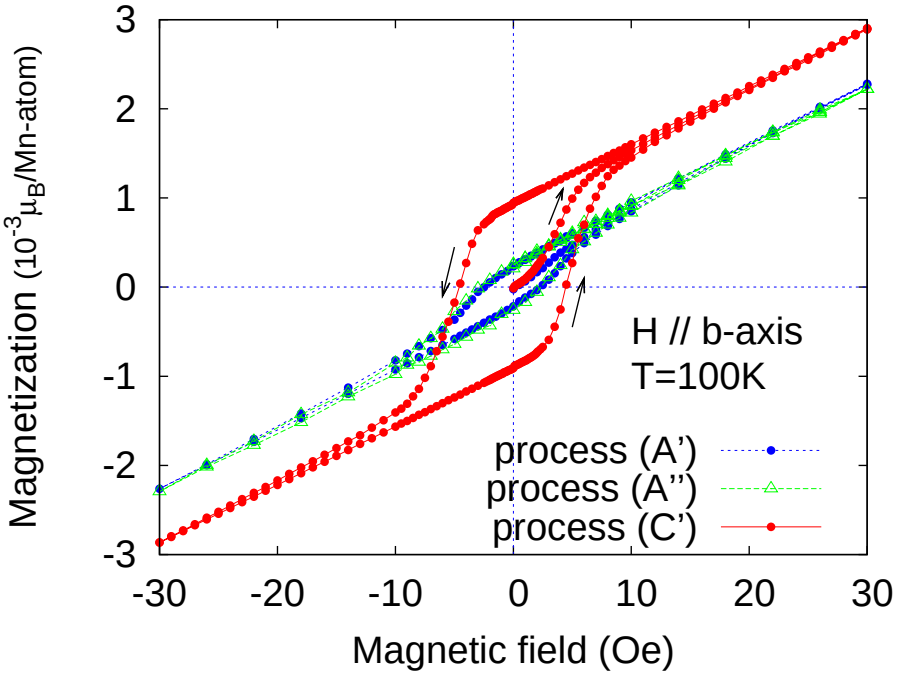

Figure 3.4: Magnetization curves along the b-axis measured in the various measurement processes at 100 K. The details of the measurement process (A'), (A'') and (C') are described in the text.

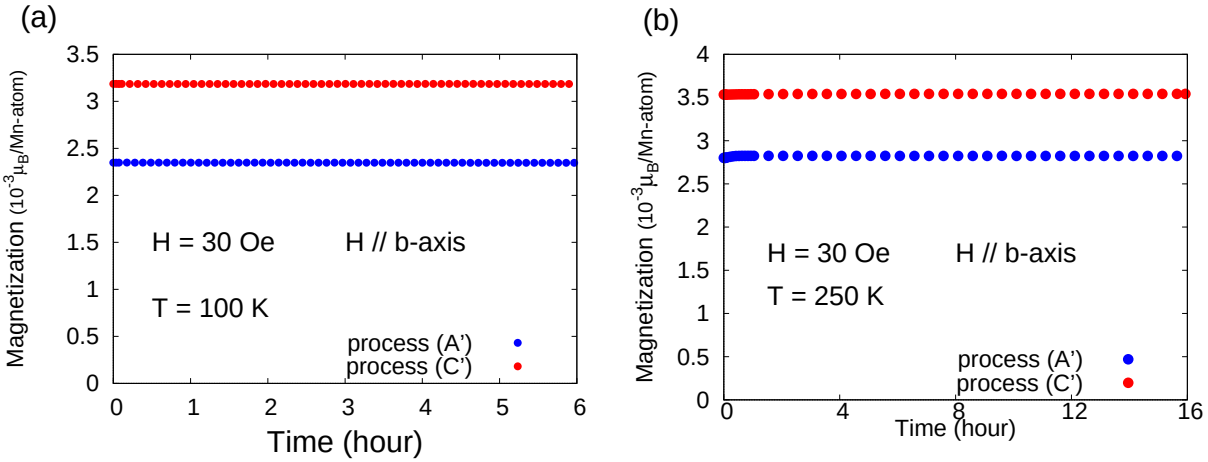

Figure 3.5: Time dependences of the magnetization along the b-axis measured in the magnetic field of 30 Oe for the LM and SM states at (a) 100 K and (b) 250 K.

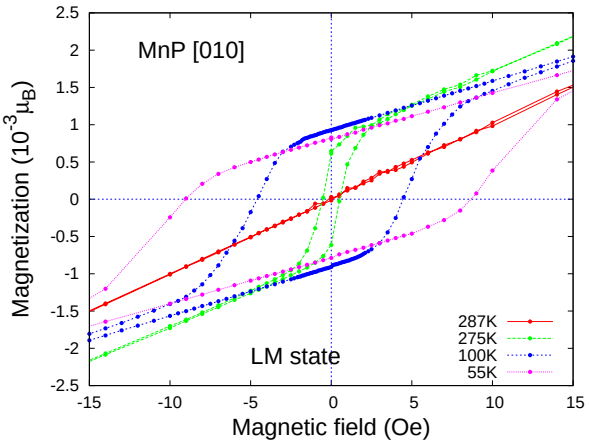

Figure 3.6: Magnetization curve along the b-axis in the LM state at various temperature.

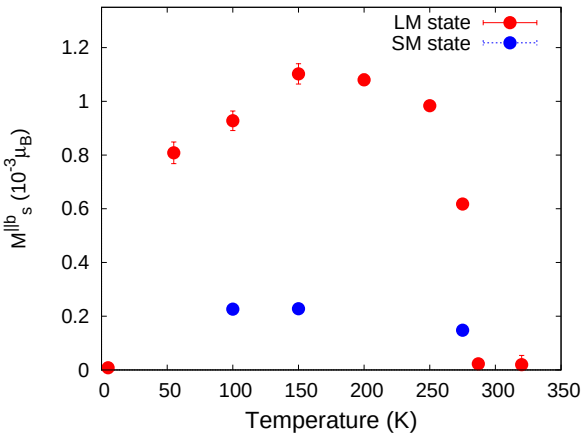

Figure 3.7: Temperature dependences of the spontaneous magnetization along the b-axis $M_s^{//b}$ in the LM and the SM states.

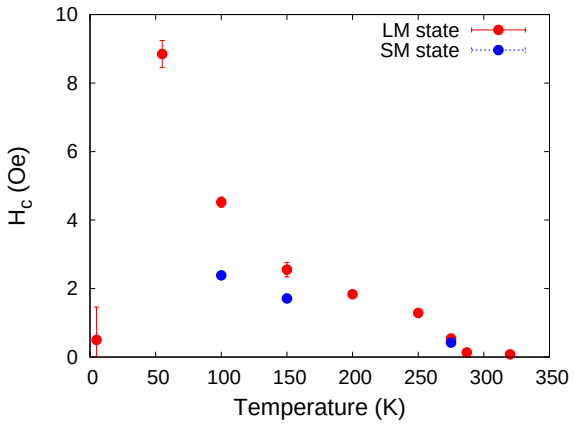

Figure 3.8: Temperature dependences of the coercive field H_c along the b-axis in the LM and the SM states.

3.1.2 Magnetization along the a-axis

Figure.3.9 shows the temperature-dependences of the DC magnetization along the a-axis in the very low field of the 3 Oe. The data measured in the same two processes (B) and (C) shown in Fig. 3.2 are shown; the former is the warm-up process from the temperature above $T_{\rm N}$, and the latter is the warm-up process from the temperature below $T_{\rm N}$. Clear process-dependent behaviors was observed in the magnetizations along the a-axes below $T_{\rm C}$ as well as done in the magnetization along the b-axis below T^*. The magnetizations along the a-axis are suppressed when the sample has been cooled to the helical phase temperature once, which is opposite behavior to that along the b-axis. It should be noted the process-dependence is observed even along the a-axis. It is surprising because it has been believed that MnP has no a-compoent of the ordered moment below $T_{\rm C}$, and hence, it is expected no process-dependence along the a-axis. In addition, the magnetization along the a-axis shows a cusp anomaly at $T_{\rm C}$, which is clearly different behavior from that of ferromagnetic one along the c-axis as shown in later and is an antiferromagnetic one. These results strongly suggest an existence of an antiferromagnetic a-component of the ordered moment below $T_{\rm C}$.

In order to investigate what temperature the sample need to be warmed up to, for restoring the magnetization along the a-axis, I performed the measurements in the same process in Fig. 3.3. The returning temperature is selected as R.P. = 270, 300, 320, 330, 340 and 350 K. Figure 3.10 shows the results of the measurements. The R.P. dependence of the magnetization along the a-axis is rather continuous, in contrast with that along the b-axis, however, discontinuous change seems to be found between R.P. = 320K and 330 K. And also, the small process-dependence of magnetization is observed up to around 310 K being higher than $T_{\rm C}$. Indeed, the process-dependece of the magnetization along the a-axis remarkably appears below $T_{\rm C}$, but it fundamentally appears below 320 K.

Figure 3.11 shows the field-dependences of the magnetization along the a-axis at 100 K. The magnetization were measured in the same two processes (A') and (C') as shown in Fig. 3.4, the former is the measurement after cooling the sample directly to the measurement temperature and the latter is one after the sample has been cooled to the helical phase below $T_{\rm N}$ once. Figure 3.11(a) and (b) shows the magnetization measured with changing the field in the following sequence: 0 Oe $\rightarrow$ 30 Oe $\rightarrow$ -30 Oe $\rightarrow$ 30 Oe and 0 Oe $\rightarrow$ 55 kOe, respectively. The process-dependent behavior as found in the M - T measurements was not found in the M - H measurements along the a-axis. Except for a bend found at about 50 kOe, which is the magnetic transition field to the fan structure phase, the magnetization changes linearly, and no anomaly is found below 50 kOe.

In addition, I measured the difference between the zero field cooled (ZFC) and

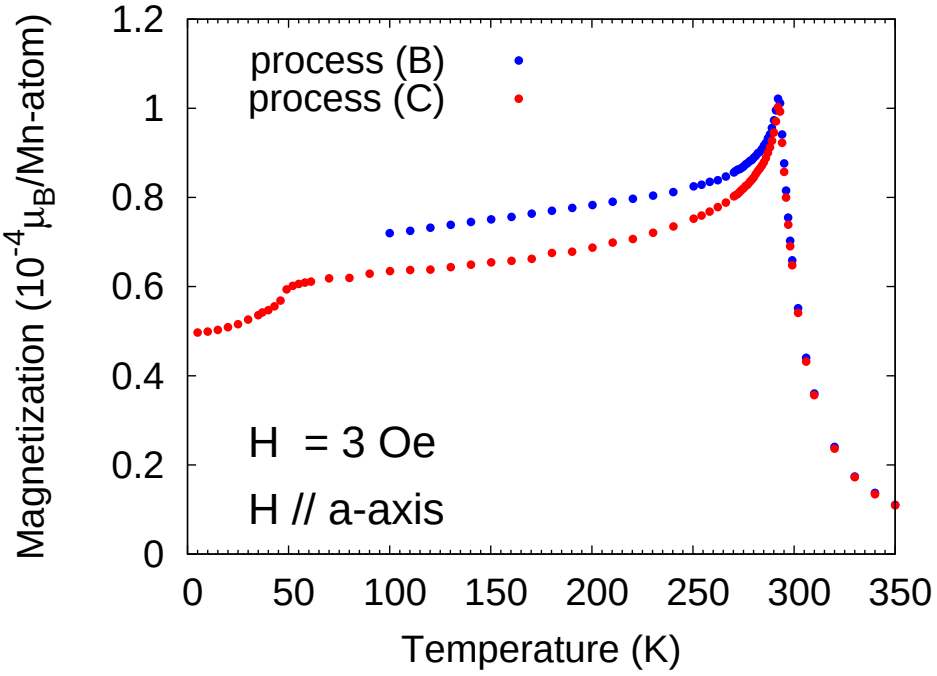

Figure 3.9: Temperature dependence of the magnetization along the a-axis measured in the warm-up process from 100 K (process (B)) and 5 K (process (C)).

field cooled (FC) susceptibility along the a-axis. Fig.3.12 shows the temperature dependences of the susceptibility $\chi = M/H$ along the a-axis. The measurements were performed in the following five warm-up processes:

(i) ZFC measurement performed from 100 K

(ii) FC measurement performed from 100 K (corresponding to the process(B) in Fig.3.9)

(iii) ZFC measurement performed from 5 K

(iv) FC measurement performed from 5 K (corresponding to the process(C) in Fig.3.9)

(v) measurement performed from 100 K after cooling the sample to 5 K and warming it up to 100 K in zero magnetic field.

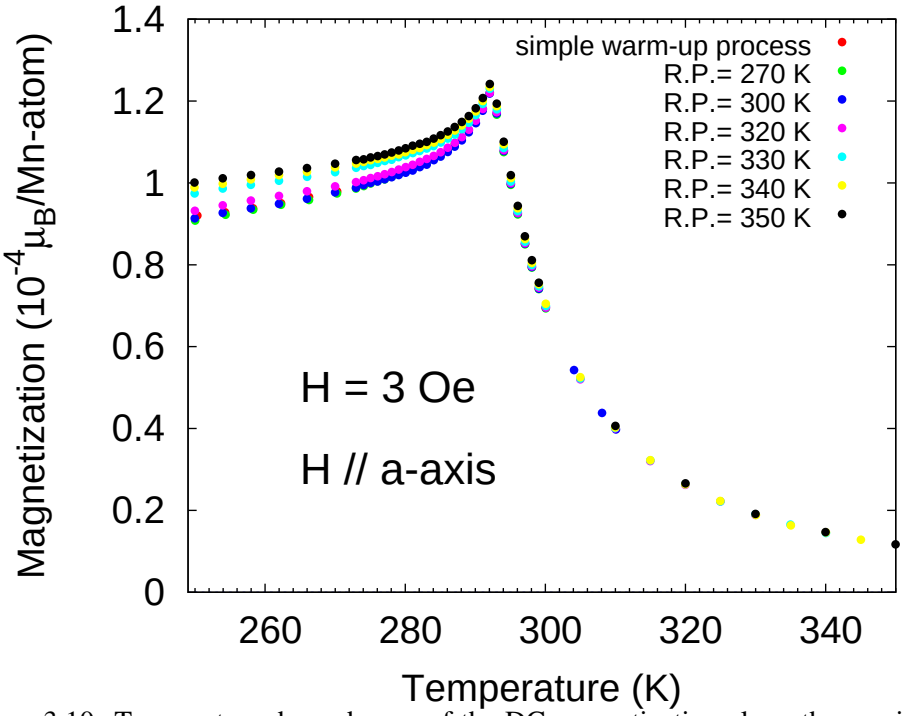

Figure 3.10: Temperature dependences of the DC magnetization along the a-axis of MnP measured from 5 K and from 250 K after the sample warming up to various returning point (R.P.).

Comparing the behavior in the process (i) with process (ii), we found a distinct separation of the ZFC and FC susceptibility below T_C. On the other hand, the separation found between in the process (iii) and (iv) is much smaller than that between in the process (i) and (ii). The separation of the ZFC and FC susceptibility is observed in spin glasses[44]. It may suggest that the a-component of spins is frozen randomly like a spin glass. However, the time dependence of the magnetization is contrast to that in the general spin glass as mentioned below. Figure 3.13 shows the time developments of the susceptibility $\chi = M/H$ along the a-axis at $H = 3$ Oe and $T = 100$ K in the process (i), (ii) and (iv). The susceptibilities exhibit no time dependences up to 16 hours in every process. No time dependence of the magnetization in the FC processes (ii) and (iv) is the same result observed in the magnetization along the b-axis shown in Fig. 3.5. it should be noted that the ZFC susceptibility in the process (i) also exhibits no time dependence. In general spin glasses, a relaxation behavior is observed, namely, ZFC susceptibility grad-

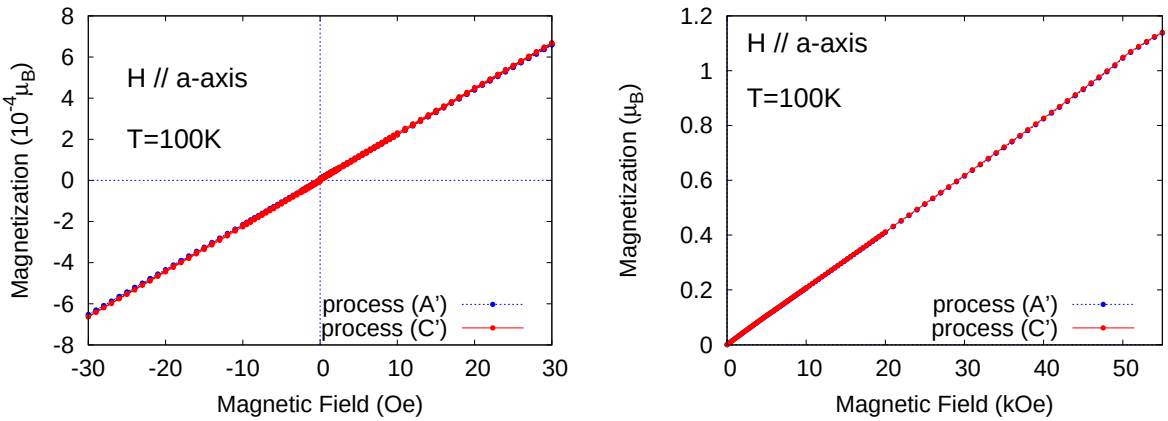

Figure 3.11: Magnetization vs magnetic field plot along the a-axis measured in the two different processes at 100 K. The details of the measurement process (A') and (C') are described in the text.

ually increase to the the equilibrium value [45]. No time dependence of the ZFC susceptibility suggests that the a-component of spins does not form a simple glassy state. It should be also noted that the susceptibility in the process (v) almost collapses with that in the process (iii), not with that in the process (i). It also indicate that the state in the intermediate temperature range is controlled by whether the sample has undergone the helical phase once or not.

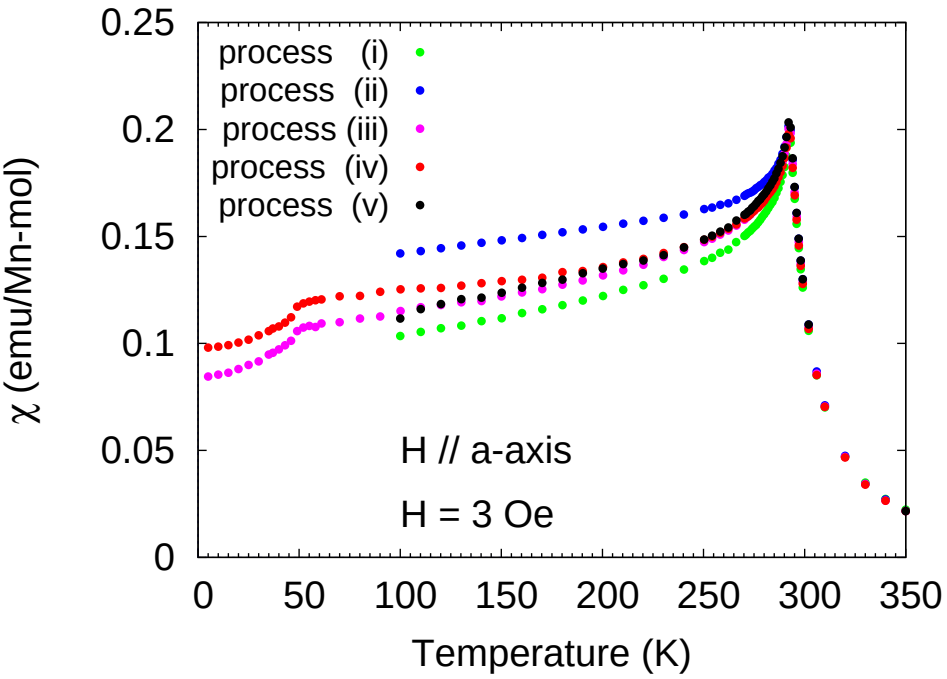

Figure 3.12: Temperature dependencies of the susceptibility along the a-axis in various measurement processes. The details of the measurement process (i)-(v) are described in the text.

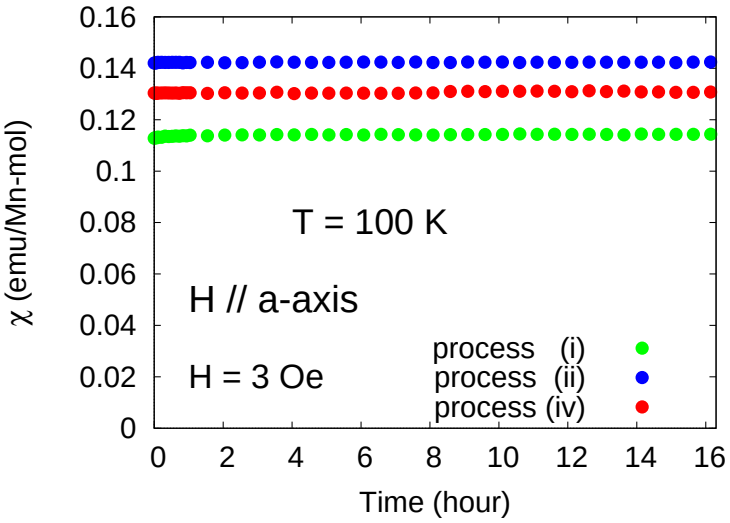

Figure 3.13: Time developments of the susceptibility along the a-axis at 100 K measured after reaching the measurement temperature with various processes.

3.1.3 Magnetization along the c-axis

The temperature-dependences of the magnetization along the c-axis are shown in Fig.3.14. The data measured in the same two processes (B) and (C) in Fig. 3.2 are shown, the former is the warm-up process from the temperature higher than T_N, and the latter is the warm-up process from the temperature below T_N. The process-dependent behavior was also observed in the magnetization along the c-axis. The magnetization along the c-axis is suppressed when the sample has been cooled to the helical phase temperature below T_N. It is the same behavior as that along the a-axis.

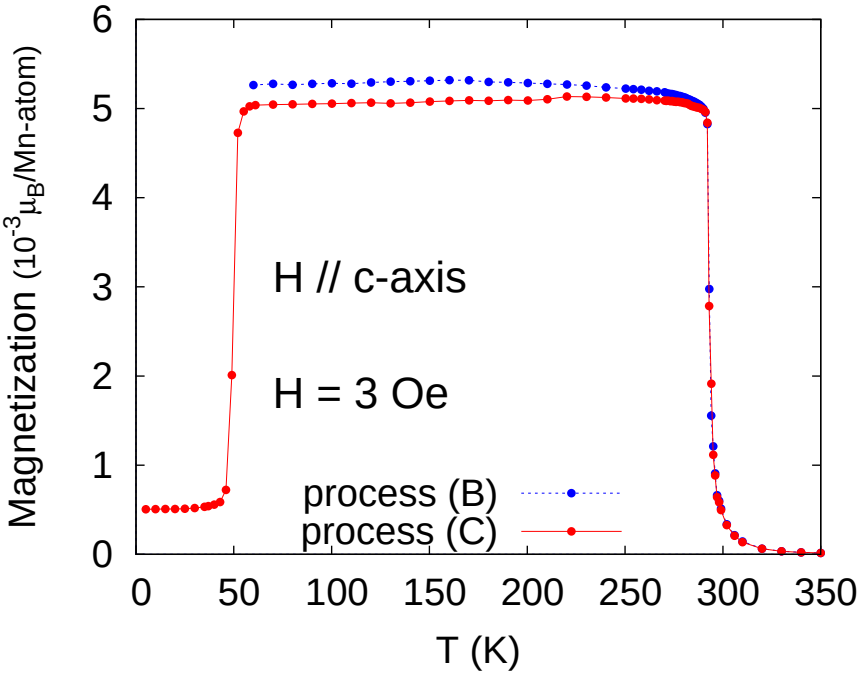

Figure 3.14: Temperature dependences of the magnetization along the c-axis measured from 60 K (process (B)) and 5 K(process (C)).

Figure 3.15 shows the field-dependences of the magnetization along the c-axis at 100 K. Figure 3.15 (a) and (b) shows the magnetization curve measured with changing the field in the following sequences: 0 Oe → 30 Oe → -30 Oe → 30 Oe and 0 Oe → 10 kOe → -10 kOe → 10 kOe, respectively. A ferromagnetic magnetization curve is observed and the saturation moment is about $1.2\mu_B$/Mn-atom as shown in Fig.3.15(b). The coercivity is, however, very weak and coercive

field is 0 Oe within a margin of errors, indicating the ferromagnetism of the c-component magnetization is very soft. The magnetization changes linearly in the range of -30 Oe $< H <$ 30 Oe (see 3.15(a)) in the both (A') and (C') processes, and the slant of the magnetization curve in the process (C') is little smaller than that in the process (A'). It is the same tendency of the process-dependence found in the $M - T$ measurement in Fig. 3.2. The slant of the magnetization curve in the low field region, however, is fully agreement with the estimated value when assuming the internal magnetic flux is zero, that is, the demagnetization field determined by the shape of the sample is equal to the applied field. It means that the magnetization along the c-axis in low field is dominated by the extrinsic factor such as the shape of the sample, and hence, the small difference of the magnetization along the c-axis found in the low field region can be hardly discussed.

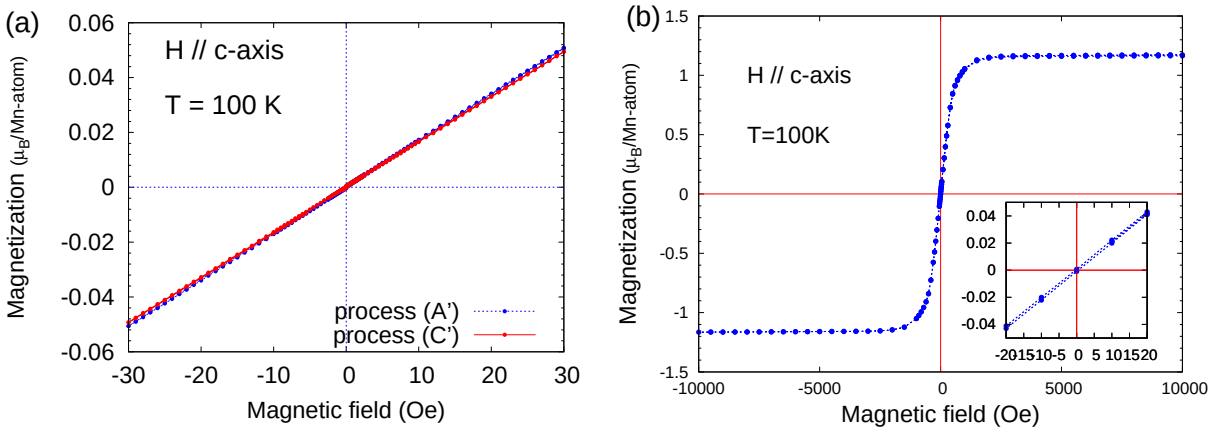

Figure 3.15: The magnetization curves along the c-axis at 100 K. (a) -30 Oe $\leq H \leq$ 30 Oe. (b) -10 kOe $\leq H \leq$ 10 kOe.

3.1.4 Magnetization in the powder sample

The temperature-dependences of the magnetization for the powder sample is shown in Fig.3.16. The data measured in the same two processes (B) and (C) in Fig. 3.2 are also shown; the former is the warm-up process from the temperature higher than $T_{\rm N}$, and the latter is the warm-up process from the temperature below $T_{\rm N}$. The small increase of the magnetization at T^* responsible for the ferromagnetic b-component was also observed in the powder sample. In addition, the process-dependent behavior was also observed. The magnetization of the powder sample was suppressed when the sample has been cooled to the helical phase temperature once, because the magnetization of the powder sample is dominated mostly by the easy-axis magnetization along the c-axis.

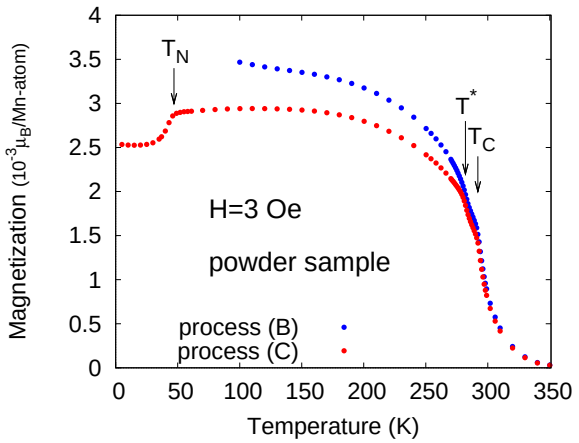

Figure 3.16: Temperature dependence of the magnetization measured for the powder sample in the warm-up process from 100 K (process (B)) and 5 K (process (C)).

3.1.5 Interpretation of the results

In the magnetization measurements, I found the following remarkable facts:

- The weak ferromagnetic behavior of the b-component with the spontaneous magnetization of $\sim 10^{-3}\mu_{\rm B}$/Mn-atom was observed in the intermediate-temperature range of $T_{\rm N} < T < T_{\rm C}$.
- The peculiar temperature hysteresis, namely, the spontaneous magnetization in the weak ferromagnetic state is remarkably enhanced when the sample has cooled to the helical phase below $T_{\rm N}$ was discovered.

Here I discuss the nature of the weak ferromagnetism with considering the following:

- Antiferromagnetic behaviors of the magnetization along the a-axis.
- Possible existence of the DM interaction between the N. N. pairs of Mn-pair.

The DM vector between the N. N. Mn-pair $\boldsymbol{D}$ should be parallel to the c-axis because the c-plane, including the pair of N. N. Mn-pairs is the mirror plane in the crystal structure of MnP (see Fig.1.4) In this case, the energy of the DM interaction between the N. N. pair of Mn-spins, $\boldsymbol{S}_1, \boldsymbol{S}_2$, is given by

$$\boldsymbol{D} \cdot (\boldsymbol{S}_i \times \boldsymbol{S}_j) = D(S_1^a S_2^b - S_1^b S_2^a).$$

It naturally induces a cant of Mn-spins and weak ferromagnetic component along the b-axis in the antiferromagnetic configuration of the a-component. Hence, I propose that the canted antiferromagnetism is the nature of the intermediate-temperature phase in $T_{\rm N} < T < T^*$

The temperature hysteresis phenomenon in the canted antiferromagnetic state caused by the sample undergoing to the helical phase is a quite peculiar. The main issue in the rest of the part I in this thesis is to illuminate the nature of this temperature hysteresis phenomenon. The change of the spontaneous magnetization caused by the temperature hysteresis is very small, being $\sim 10^{-3}\mu_{\rm B}$. The small change of the magnetization, however, cannot be induced by applying the field up to 10 kOe. What in the helical phase induces the LM state? Moreover, the SM state which realizes when the sample is directly cooled from high temperature is completely separated by a very high energy barrier from the LM state which realizes when the sample is warmed up from the helical phase. What separates the two states? To answer these questions, I tried to observe anomalies at T^* and process-dependent behaviors in other physical properties.

3.2 Resistivity

The electrical resistivity measurements of MnP has been previously performed by several groups[46, 47, 48, 49, 50, 51]. Detailed experiments, however, have been done only in order to investigate the Fermi liquid behavior in the low temperature region. The main purpose of the measurement is to find some anomalies due to the phase transition at T^* and the hysteresis phenomena in the canted antiferromagnetic phase.

Figure 3.17 shows the temperature dependences of the electrical resistivity ρ measured in the the cool-down process from the paramagnetic temperature of 310 K and in the warm-up process from the helical phase temperature of 9.3 K. The details in the high temperature region including T^* and $T_{\rm C}$ and in the low temperature region around $T_{\rm N}$ are shown in Fig.3.18 and 3.19, respectively. The electric current was induced along the a-axis. In contrast with the case of the magnetization, the difference of the resistivity in the warm-up process and in the cool-down process is not found in the whole temperature region, except for the thermal hysteresis behavior accompanied by the first order phase transition at $T_{\rm N}$. A bend type anomaly is observed at $T_{\rm C}$, whereas, no anomaly is found at T^* in the electrical resistivity.

As shown in Fig. 3.19, hump-type anomalies at 47.3 K and 47.6 K are found in the cool-down process and in the warm-up process, respectively, which are due to the first order phase transition between the canted antiferromagnetic phase and the helical phase. The thermal hysteresis originating from this first order phase transition was observed between 46.9 K and 49.5 K. The thermal hysteresis behavior around $T_{\rm N}$ was also observed by Takase, *et al.* [49], however, the region is different from that in our experiments. Takase *et al.* reported that the temperature found the hump-type anomaly indicating $T_{\rm N}$ increases up to about 51 K with decreasing the crystal defects of the sample. And also, a hysteresis region in the vicinity of a first order phase transition temperature is generally very sensitive to the sample quality. Hence, we conclude that the discrepancy between the result by Takase *et al.* and ours is due to small difference of the sample qualities. The thermal hysteresis behavior accompanied by the first order phase transition $T_{\rm N}$ was found in the narrow temperature range of $\Delta T \sim 2$ K. The temperature hysteresis phenomena, which observed in the whole range of $T_{\rm N} < T < T_{\rm C}$ in magnetization measurements, is entirely different from such the thermal hysteresis.

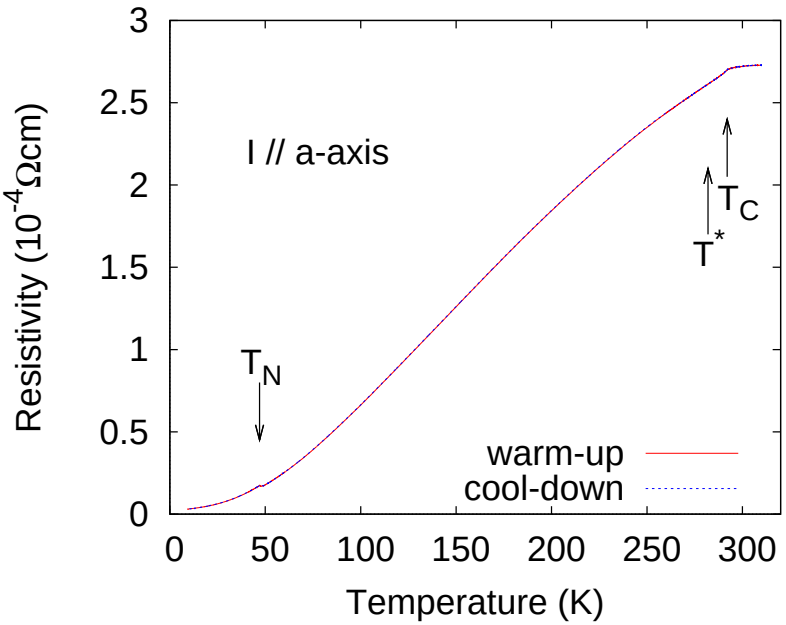

Figure 3.17: Temperature dependence of the resistivity in MnP

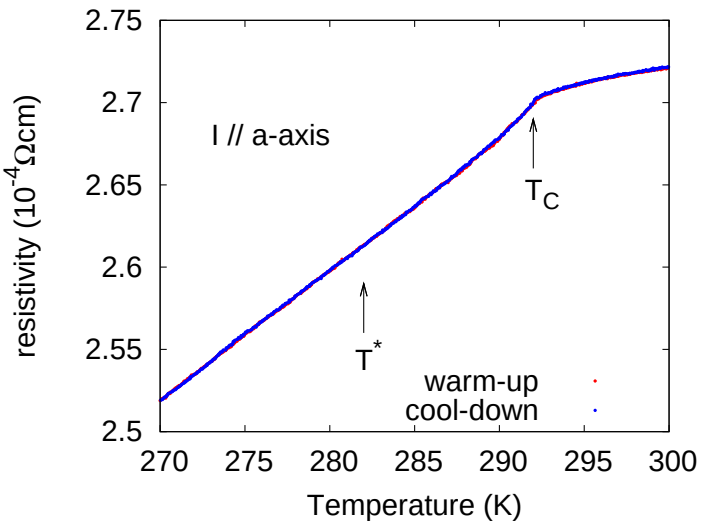

Figure 3.18: Temperature dependence of the resistivity around T^* and T_C in MnP

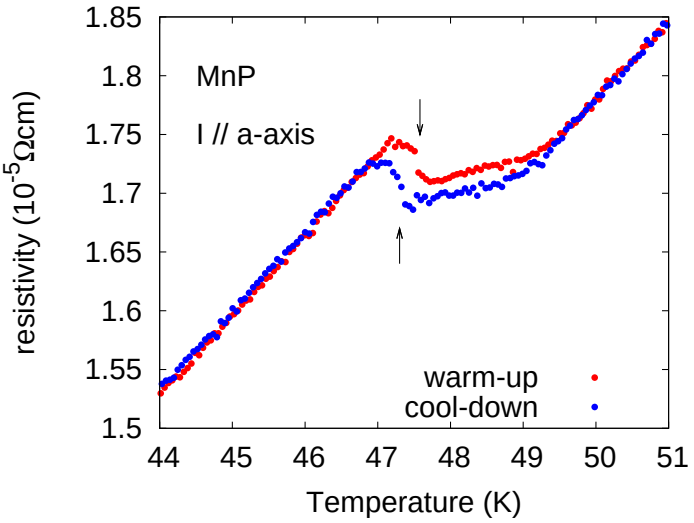

Figure 3.19: Temperature dependence of the resistivity around T_{N} in MnP

3.3 Specific heat

The specific heat measurements has been also previously performed only in the low temperature region [35]. Figure 3.20 shows the temperature dependences of the specific heat C measured in the the cool-down process from the paramagnetic temperature of 310 K and in the warm-up process from 5 K to 350 K. The details in the high temperature region including T^* and T_C and in the low temperature region around T_N are shown in Fig.3.21 and 3.22, respectively. The difference of the specific heat between in the warm-up process and in the cool-down process is not found in the whole temperature region, except thermal hysteresis behavior accompanied by the first order phase transition at T_N. A divergent behavior was observed at T_C, however, no anomaly was found at T^* in the specific heat (see Fig. 3.21). A jump of the specific heat with the small thermal hysteresis was observed at T_N (see Fig. 3.22).

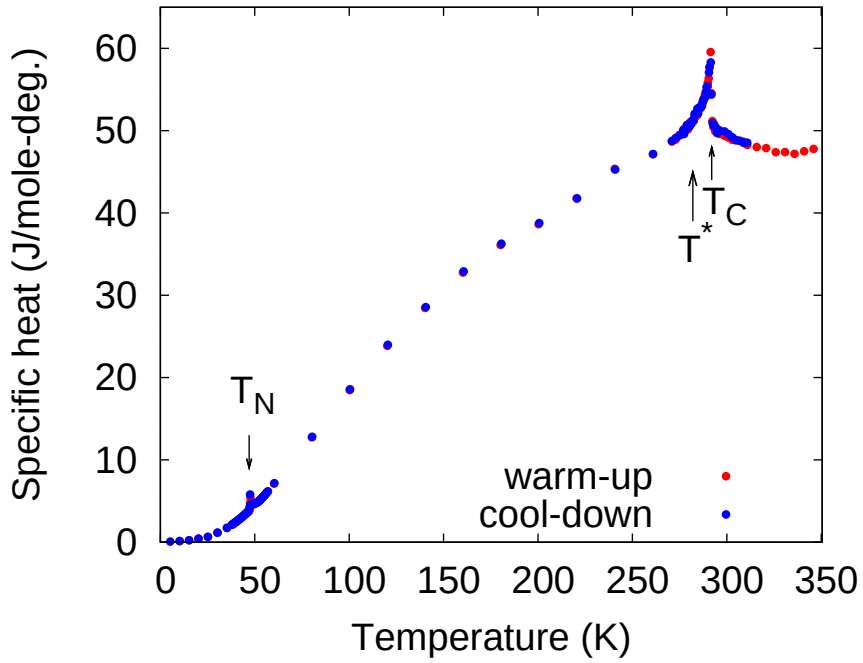

Figure 3.20: Temperature dependence of the specific heat in MnP

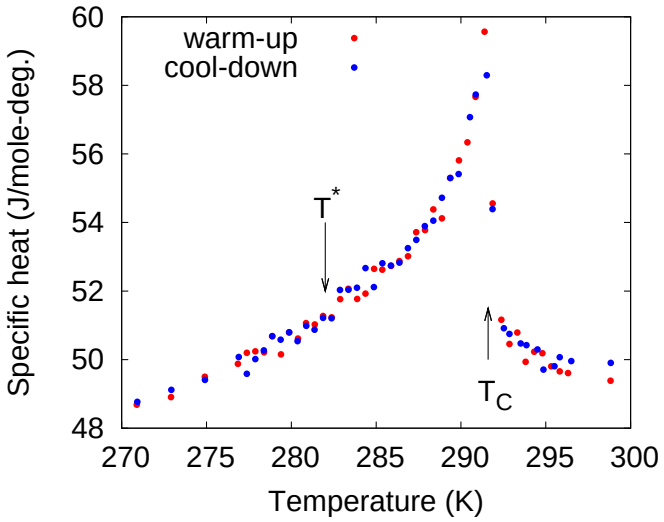

Figure 3.21: Temperature dependence of the specific heat around T^* and T_C in MnP

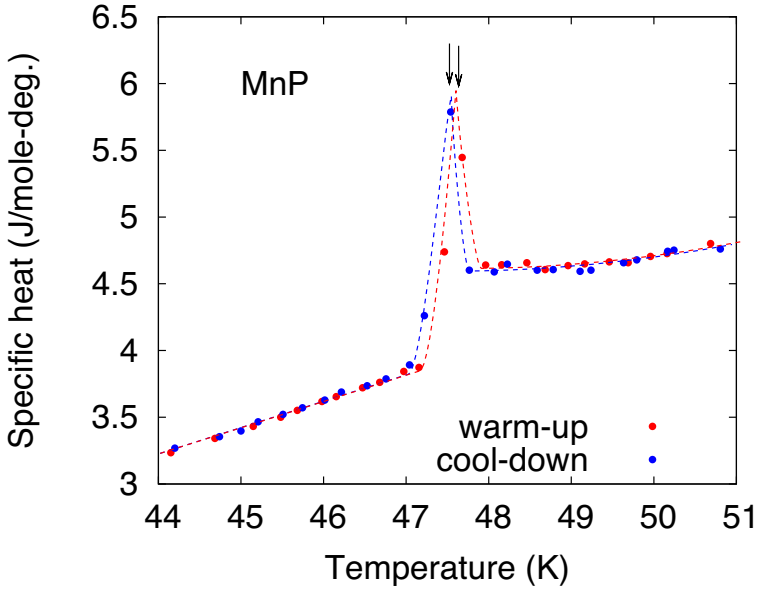

Figure 3.22: Temperature dependence of the specific heat around T_N in MnP

3.4 Neutron scattering

3.4.1 Novel magnetic reflection at $(\delta, 1, 0)$ below T_{N}

As mentioned in Sec. 2.5, the neutron scattering experiments is a powerful technique to investigate magnetic properties of condensed matters, and hence, it is very interesting to examine the nature of the temperature hysteresis phenomena observed in the magnetization by the neutron scattering experiments. And also, some influence of the DM interaction appears in MnP, the magnetic structure should be modulated. For these purpose, I performed the neutron scattering experiments. The basis of analyses for the data of the neutron scattering experiment is described in Appendix A.

Figure.3.23 shows the diffraction patterns of the neutron power diffraction experiments performed with changing the temperature in the following sequence: 100 K $\rightarrow$ 10 K $\rightarrow$ 100 K $\rightarrow$ 200 K $\rightarrow$ 300 K $\rightarrow$ 200 K. Any difference of the diffraction patterns in the cool-down process and in the warm-up process is not found at 100 K and 200 K, being in the intermediate-temperature phase. Although the change of the peak positions,which indicates the change of the lattice constants, were observed with decreasing the temperature, any additional peak was not observed in the intermediate-temperature phase. We can see the asymmetrical intensities of the magnetic reflection at both sides of the nuclear Bragg reflection $\boldsymbol{k} = \boldsymbol{K} \pm \boldsymbol{\delta}$ at 10 K. It was explained with assuming the double spiral type helical structure by Forsyth [23] (see Appendix A). No additional peaks except for the magnetic reflections reported previously are found. After all, any new information about the magnetic structure in MnP in both the intermediate-temperature phase and the helical phase was obtained by the neutron powder diffraction experiments.

For more detailed investigation, the neutron scattering experiments by using the single crystals were performed with the triple-axis spectrometer. The positions of the nuclear reflections and the magnetic reflections in the reciprocal lattice space expected by assuming the conventional helical structure are shown in Fig. 3.24. In such the detailed investigation, I discovered a novel magnetic reflection at $(\delta, 1, 0)$ below T_{N}. The magnetic reflection at $(\delta, 1, 0)$ and $(-\delta, 1, 0)$ are shown in Fig.3.25. Considering the crystal structure of MnP, the nuclear reflections with the condition of (h, k) =(0,odd) and (odd,0) are forbidden (see Appendix A and Fig.3.24). The (0,1,0) and (1,0,0) reflections were not actually observed in our experiments (see Fig. 3.26). In general, the satellite peaks also does not appear at the side of such a forbidden nuclear reflection. The magnetic reflection at $(\delta, 1, 0)$, however, was distinctly observed. The intensity of $(\delta, 1, 0)$ reflection is about 500 times smaller than that of $(2 + \delta, 0, 0)$. Indeed the $(\delta, 1, 0)$-reflection could appear if the helical structure is the conventional double spiral type one with the finite relative phase

between the N. N. Mn-spins. However, the calculated intensity based on the double spiral structure discussed in [23] is about 10^5 times smaller than that of the $(2+\delta, 0, 0)$. This large discrepancy clearly indicates that the magnetic structure of MnP in the low temperature should be modulated from the previously reported one.

Here, I discuss on the possible modulation of the magnetic structure below $T_{\rm N}$ in MnP. First, I assume the modulation with the propagation vector $(\delta, 1, 0)$ simply. If this modulation is, the reflections at $(1 \pm \delta, 0, 0) = (1, \mp 1, 0) \pm (\delta, 1, 0)$ should appear, however, the $(1 \pm \delta, 0, 0)$ reflections were not observed as shown in Fig.3.26. And hence, the (δ,1,0)-modulation of the a-component of the ordered moment is concluded. The modulation of the a-component as illustrated in Fig. 3.27 can give rise to the $(\delta, 1, 0)$ reflection. The a-component is modulated with the wave number δ along the a-direction and is in an antiparallel configuration between the N. N. Mn-spins where the distance is $b/2$. With superposing this modulation of the a-component on the conventional helical structure with the helical plane parallel to the bc-plane, the magnetic structure as shown in Fig.3.27 (b) is obtained. In this structure, the helical planes tilted to the a-direction with the angles of $+\theta$ and $-\theta$ alternately along the b-direction. The schematic view of the same structure from different view angle is shown in Fig. 3.28.

Next, I discuss on the newly proposed magnetic structure below $T_{\rm N}$ from the viewpoint of the crystal symmetry. As mentioned in Sec. 1.2, the inversion symmetry at the center between the N.N. Mn-sites is broken and the DM interaction can work between the N.N. Mn-spins. If we consider the DM interaction between the N. N. Mn-spins, the magnetic structure above mentioned can be realized naturally. As mentioned in subsection 3.1.5, the DM interaction with the DM vector $\boldsymbol{D}$ is parallel to the c-axis in MnP, and the energy of the DM interaction between the N. N. Mn-spins, $\boldsymbol{S}_1$, $\boldsymbol{S}_2$, is given by

$$\boldsymbol{D} \cdot (\boldsymbol{S}_i \times \boldsymbol{S}_j) = D(S_1^a S_2^b - S_1^b S_2^a). \tag{3.1}$$

This energy tilts the spin-components in the ab-plane with a degree of $\theta = \tan^{-1}(D/J)$, where J is the symmetric interaction between the N.N. Mn-spins. Because the ab-component of the N.N. Mn-spins in the fundamental structure, the helical structure, are parallel to the b-axis and are parallel each other, their tilted angles are opposite each other, as being θ and $-\theta$, respectively (see Fig. 3.29). And also, the DM vector directed alternately lines along the b-direction. Consequently, the magnetic structure with the helical planes tilted to the a-direction with the angles of θ and $-\theta$ alternately as shown in Fig.3.28 is also expected with considering the crystal symmetry. Therefore, I propose the tilted helical structure as shown in Fig. 3.28 as the true magnetic structure below $T_{\rm N}$.

3.4.2 Analysis for the tilted helical structure below T_{N}

Here, the analysis of the magnetic reflection intensities with assuming the tilted helical structure as shown in Fig. 3.28 is mentioned. In this analysis, I adopted the Forsyth's model of the double helical structure [23] as the fundamental structure (see Appendix A). I redefine the spin vector at the Mn-site denoted by the spacial position $\boldsymbol{r}$ and the sublattice position in the unit cell ν, $\boldsymbol{\eta}_{\nu\boldsymbol{r}}$, defined by the eq. A.2 in the Appendix A as

$$\boldsymbol{\eta}_{\nu\boldsymbol{r}} = \boldsymbol{q}_c \cos(\boldsymbol{\delta}\cdot\boldsymbol{r}+\gamma_\nu) + \{\hat{\boldsymbol{q}}_b q_b' \cos\phi_\nu + \hat{\boldsymbol{q}}_a q_b' \sin\phi_\nu\}\sin(\boldsymbol{\delta}\cdot\boldsymbol{r}+\gamma_\nu). \quad (3.2)$$

where ϕ_ν is the tilted angle of the spins on the νth Mn-site in the unit cell by the DM interaction and q_b' is the magnitude of the b-component of the ordered moment without consideration of the tilt by the DM interaction. The calculation can be operated by the same way as described in the Appendix A, and the Fourier component of $\boldsymbol{\eta}_{\nu\boldsymbol{r}}$ $\boldsymbol{Q}_\nu$ is given by

$$\begin{aligned}
\boldsymbol{Q}_\nu(\boldsymbol{k}) &= \int_r \boldsymbol{\eta}_{\nu\boldsymbol{r}} \exp(-i\boldsymbol{k}\boldsymbol{r})d\tau \\
&= \frac{1}{2}\boldsymbol{q}_c \int_r \exp[i\{(-\boldsymbol{k}+\boldsymbol{\delta})\cdot\boldsymbol{r}+\gamma_\nu\}] + \exp[\{i(-\boldsymbol{k}-\boldsymbol{\delta})\cdot\boldsymbol{r}-\gamma_\nu\} \\
&\quad + \frac{1}{2}\hat{\boldsymbol{q}}_b q_b' \cos\phi_\nu \int_r \exp[i\{(-\boldsymbol{k}+\boldsymbol{\delta})\cdot\boldsymbol{r}+\gamma_\nu\}] - \exp[\{i(-\boldsymbol{k}-\boldsymbol{\delta})\cdot\boldsymbol{r}-\gamma_\nu\}]d\tau \\
&\quad + \frac{1}{2}\hat{\boldsymbol{q}}_a q_b' \sin\phi_\nu \int_r \exp[i\{(-\boldsymbol{k}+\boldsymbol{\delta})\cdot\boldsymbol{r}+\gamma_\nu\}] - \exp[\{i(-\boldsymbol{k}-\boldsymbol{\delta})\cdot\boldsymbol{r}-\gamma_\nu\}]d\tau
\end{aligned} \quad (3.3)$$

It is a similar form to eq. A.7. The first term in each integrals is zero unless $\boldsymbol{\delta}=\boldsymbol{k}$ and the second one is zero unless $\boldsymbol{\delta}=-\boldsymbol{k}$. If the number of unit cells is very large, finally, the magnetic scatterings only appear at $\boldsymbol{k}=\boldsymbol{K}\pm\boldsymbol{\delta}$ where $\boldsymbol{K}$ is the reciprocal lattice vector. The satellite peaks will be observed at $\boldsymbol{K}\pm\boldsymbol{\delta}$, and $\boldsymbol{P}(\boldsymbol{K}\pm\boldsymbol{\delta})$ can be expressed as

$$\begin{aligned}
\boldsymbol{P}(\boldsymbol{K}+\boldsymbol{\delta}) \propto \sum_\nu f_\nu(\boldsymbol{K}+\boldsymbol{\lambda})\frac{1}{2}[\boldsymbol{q}_c \exp\{i(\boldsymbol{K}\cdot\boldsymbol{r}_\nu-\gamma_\nu)\} - \hat{\boldsymbol{q}}_b q_b' \cos\phi_\nu \exp\{i(\boldsymbol{K}\cdot\mathrm{r}-\gamma_\nu)\} \\
-\hat{\boldsymbol{q}}_a q_b' \sin\phi_\nu \exp\{i(\boldsymbol{K}\cdot\mathrm{r}-\gamma_\nu)\}]
\end{aligned} \quad (3.4)$$

$$\begin{aligned}
\boldsymbol{P}(\boldsymbol{K}-\boldsymbol{\delta}) \propto \sum_\nu f_\nu(\boldsymbol{K}-\boldsymbol{\lambda})\frac{1}{2}[\boldsymbol{q}_c \exp\{i(\boldsymbol{K}\cdot\boldsymbol{r}_\nu+\gamma_\nu)\} + \hat{\boldsymbol{q}}_b q_b' \cos\phi_\nu \exp\{i(\boldsymbol{K}\cdot\mathrm{r}+\gamma_\nu)\} \\
+\hat{\boldsymbol{q}}_a q_b' \sin\phi_\nu \exp\{i(\boldsymbol{K}\cdot\mathrm{r}+\gamma_\nu)\}]
\end{aligned} \quad (3.5)$$

$f_\nu(\boldsymbol{k})$ is the magnetic form factor of Mn-atom at the ν-site. Substituting the positions of the Mn site ($\nu = 1, 2, 3, 4$) assigned as eq. A.10, and replace any $f_\nu(\boldsymbol{k})$ with $f_{\rm Mn}(\boldsymbol{k})$ by assuming the form factor does not depend on the direction of the spin, the a-component of $\boldsymbol{P(K-\delta)}$ in eq. 3.5 can be expressed as

$$\begin{aligned}
&\frac{P(\boldsymbol{K}-\boldsymbol{\delta})_a}{Cf_{\rm Mn}(\boldsymbol{K}-\boldsymbol{\delta})} \\
&\quad = \frac{1}{2}\left[\cos X\cos Y\{\sin\phi_1 e^{i\gamma_1}+\sin\phi_2 e^{i\gamma_2}+\sin\phi_3 e^{i\gamma_3}+\sin\phi_4 e^{i\gamma_4}\}\right. \\
&\qquad -\sin X\sin Y\{\sin\phi_1 e^{i\gamma_1}-\sin\phi_2 e^{i\gamma_2}+\sin\phi_3 e^{i\gamma_3}-\sin\phi_4 e^{i\gamma_4}\} \\
&\qquad +i\sin X\cos Y\{\sin\phi_1 e^{i\gamma_1}-\sin\phi_2 e^{i\gamma_2}-\sin\phi_3 e^{i\gamma_3}+\sin\phi_4 e^{i\gamma_4}\} \\
&\qquad \left.+i\cos X\sin Y\{\sin\phi_1 e^{i\gamma_1}+\sin\phi_2 e^{i\gamma_2}-\sin\phi_3 e^{i\gamma_3}-\sin\phi_4 e^{i\gamma_4}\}\right]
\end{aligned} \tag{3.6}$$

where

$$\begin{aligned}
X &= 2\pi\left[hx_1+\frac{1}{4}(h+k)\right] \\
Y &= 2\pi\left[ky_1-\frac{1}{4}(h+k-l)\right]
\end{aligned}$$

Here, I adopts the relative phases condition of γ_ν as $\gamma_1=\gamma_4$, $\gamma_2=\gamma_3$, which was lead by the Forsyth. As described in subsection 3.4.1, the tilted angles of the N.N. Mn-spins are opposite each other, and hence, the condition of ϕ_ν as $\phi_1=-\phi_2$ and $\phi_3=-\phi_4$ is adopted. Consequently, there are tow possible combinations of ϕ_ν as follows: (a) $\phi_1=-\phi_2=-\phi_3=\phi_4=\phi$; (b) $\phi_1=-\phi_2=\phi_3=-\phi_4=\phi$. In the case of the combination (a), the (δ,1,0)-reflection almost disappears, and hence, I ruled out this possibility. In the case of the combination (b), the first line and the third line of the eq. 3.6 are zero, and

$$\begin{aligned}
\frac{P(\boldsymbol{K}-\boldsymbol{\delta})_a}{Cf_{\rm Mn}(\boldsymbol{K}-\boldsymbol{\delta})} &= \sin X\sin Y\sin\phi(e^{i\gamma_1}+e^{i\gamma_2}) \\
&\quad +i\cos X\sin Y\sin\phi(e^{i\gamma_1}-e^{i\gamma_2}).
\end{aligned} \tag{3.7}$$

When $h=0$ and $k=$odd, the second line is zero, and

$$\frac{P(\boldsymbol{K}-\boldsymbol{\delta})_a}{Cf_{\rm Mn}(\boldsymbol{K}-\boldsymbol{\delta})} = 2\sin X\sin Y\sin\phi\cos(\frac{\gamma_1-\gamma_2}{2})e^{i\frac{\gamma_1+\gamma_2}{2}}. \tag{3.8}$$

The a-component of the $\boldsymbol{P(K+\delta)}$ is the same form as that of $\boldsymbol{P(K-\delta)}$. Thus the magnetic reflection at the $(\pm\delta, 1, 0)$ is not extinct in the tilted helical structure.

In our calculation, the relative phase difference $\gamma_1 - \gamma_2 = 16.1^\circ$, which was lead by Forsyth, was substituted. The magnetic form factor reported for the Mn-3d electron in the $\alpha-$Mn was adopted as $f_{\rm Mn}$ [52]. The b-component without the tilt $q_b' = 1.29\mu_{\rm B}$, which is the estimated value of the ordered moment o the helical structures [21, 26], was chosen. From the ratio of the intensities of the (δ,1,0)- and of the ($2+\delta$,0,0)-reflections, being 1:500, the tilted angle ϕ is estimated as,

$$\phi \fallingdotseq 6.2^\circ.$$

This small tilted angle is adequate because the DM interaction is generally much smaller than the symmetric interaction. And also, the magnitude of the a-component of the ordered moment q_a is

$$q_a = q_b' \sin\phi \fallingdotseq 0.14\mu_{\rm B}.$$

In addition, the magnitude of the b-component of the ordered moment $q_b = q_b' \cos\phi$ is 1.28 $\mu_{\rm B}$. The values of q_b and q_b' are quite similar, and hence, intensities of other magnetic reflections observed previously can be reproduced on a basis of the newly proposed tilted helical structure as well as the fundamental double helical structure proposed previously.

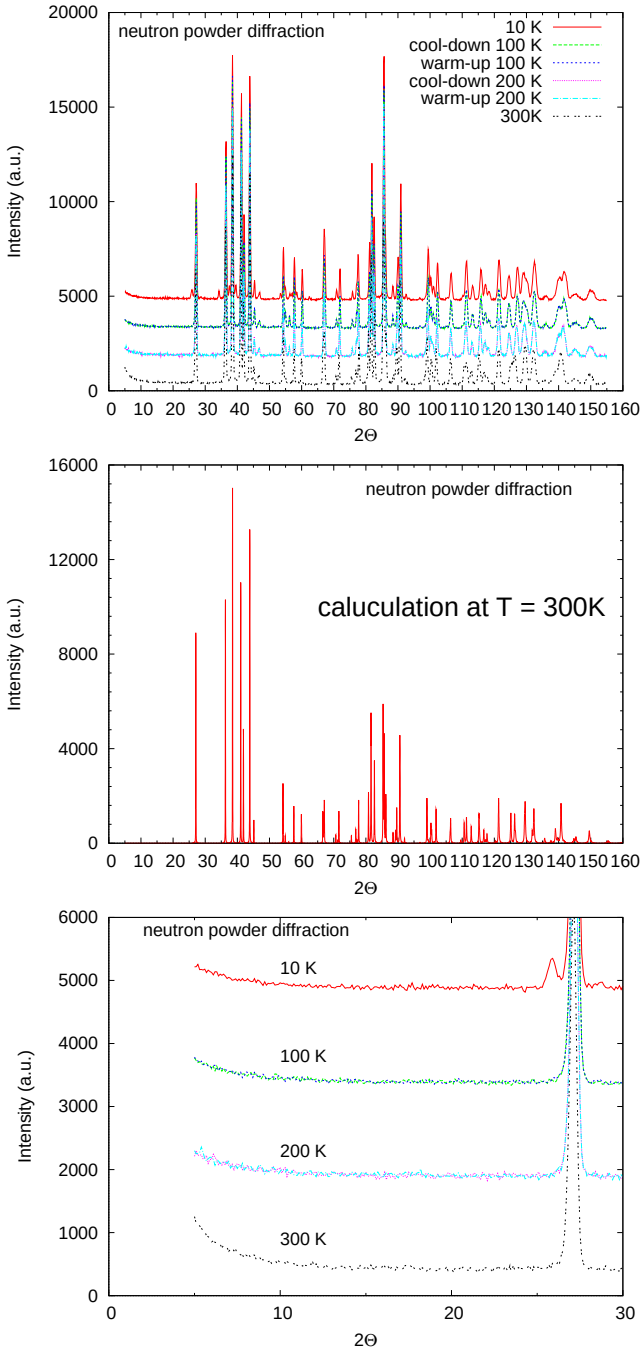

Figure 3.23: In the upper figure, the diffraction patterns of the neutron powder diffraction experiment in MnP performed in the cool-down process and in the warm-up process are shown. The middle figure shows the calculation pattern of MnP at 300 K. The lower figure is the details in the small angle region.

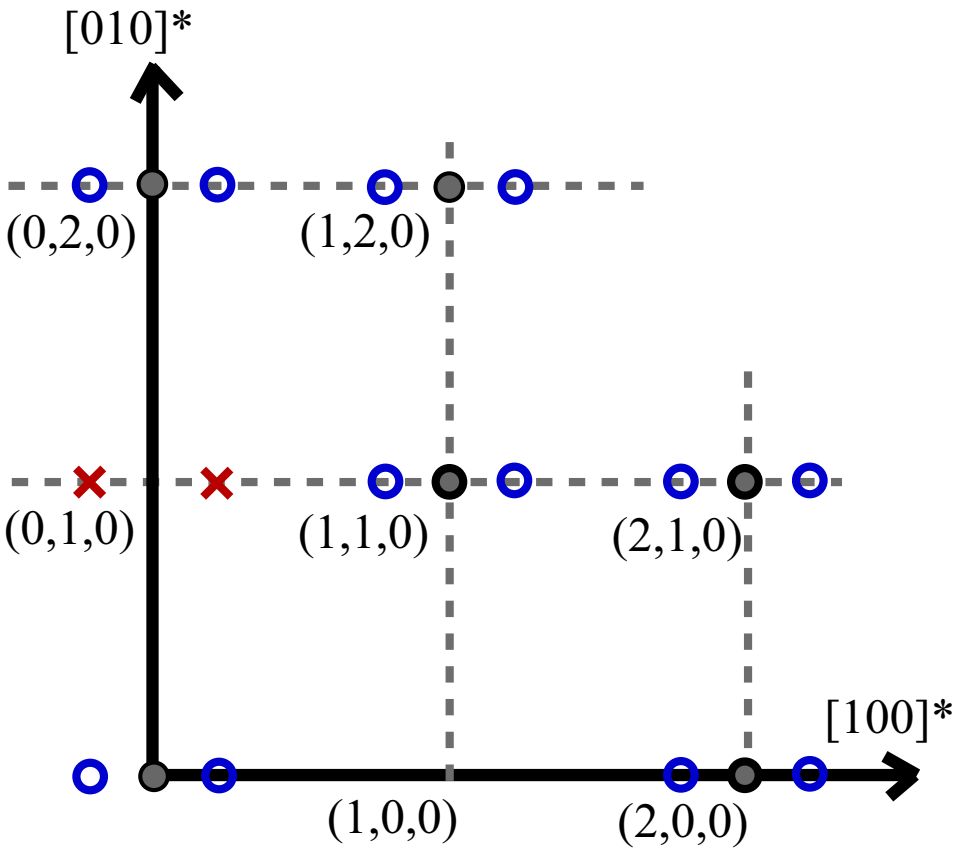

Figure 3.24: The positions in the reciprocal lattice space of the observable nuclear reflections (black closed circles), the magnetic reflection (blue open circles) expected by assuming the previously reported magnetic structure and newly discovered magnetic reflection at $(\pm\delta, 1, 0)$ (red cross) below T_{N}.

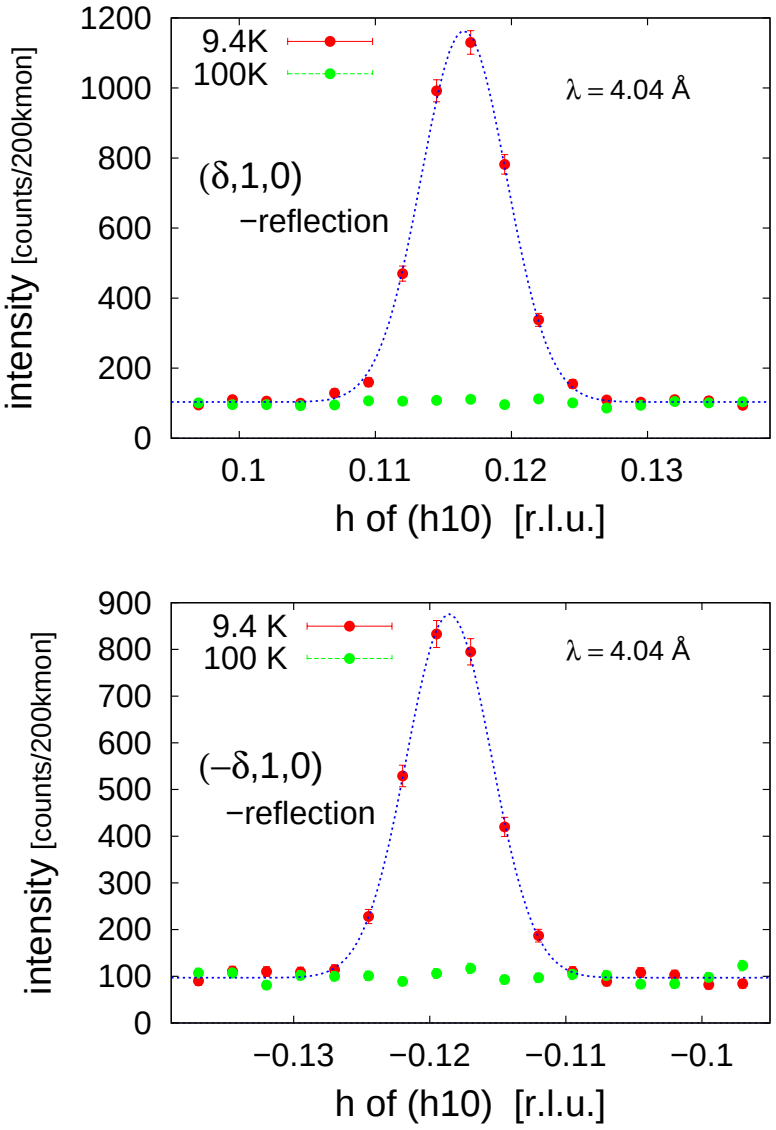

Figure 3.25: The profiles of the magnetic reflections at (δ, 1, 0) and (-δ, 1, 0).

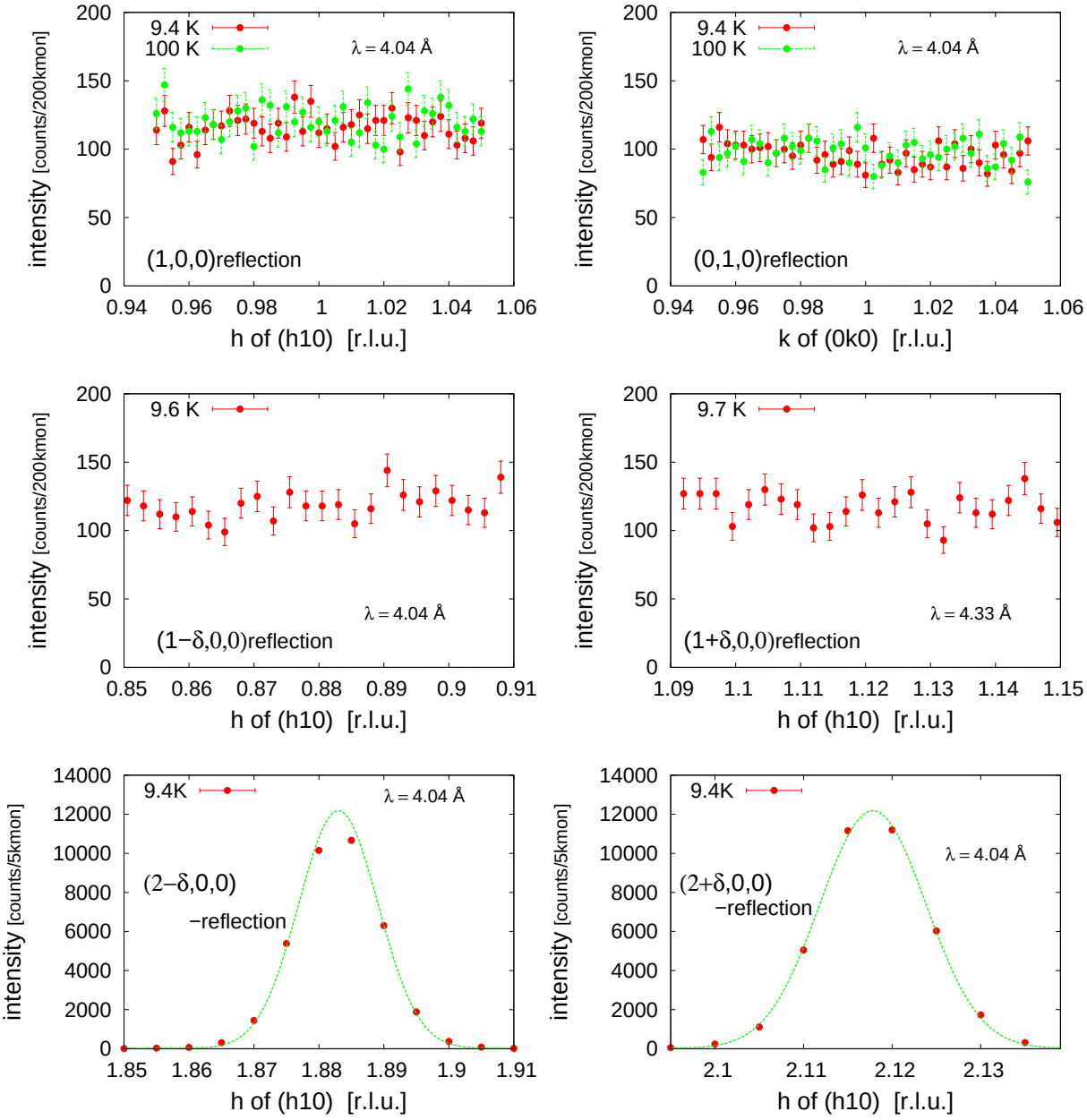

Figure 3.26: The profiles of the (1,0,0), (0,1,0), $(1 \pm \delta, 0, 0)$ and $(2 \pm \delta, 0, 0)$-reflections.

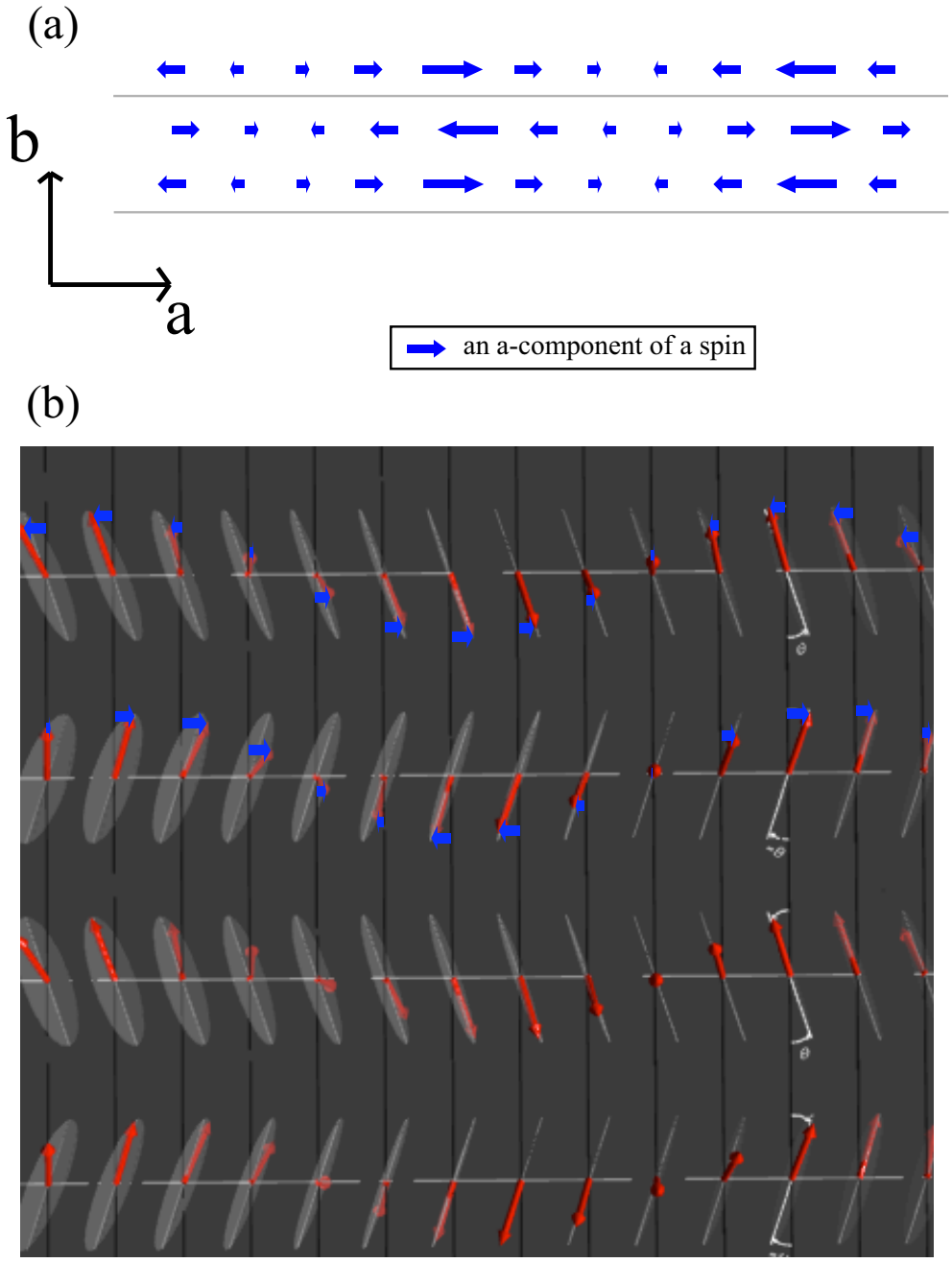

Figure 3.27: (a) The schematic illustration of the $(\delta, 1, 0)$ magnetic modulation. (b) The schematic illustration of the tilted helical structure. The blue arrows in the figures represent the a-components of spins.

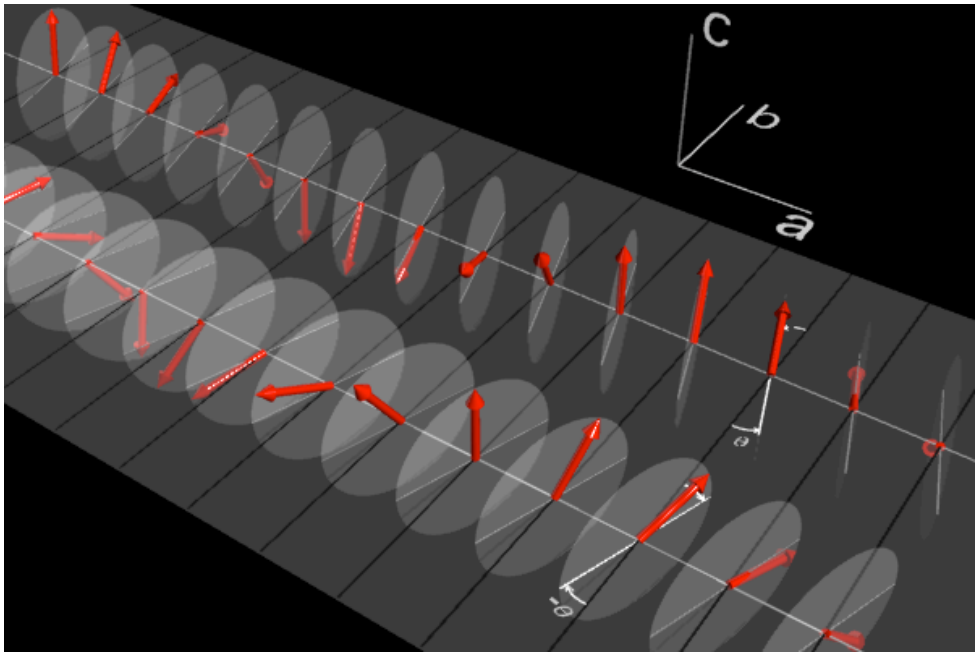

Figure 3.28: The schematic illustration of the tilted helical structure from the different view angle from that in Fig. 3.27 (b)

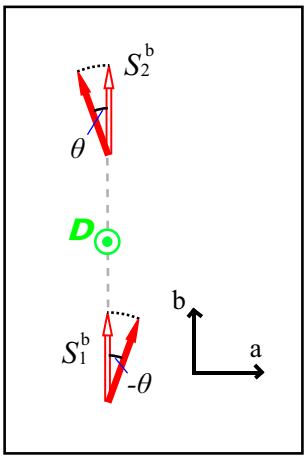

Figure 3.29: Schematic view of the tilt of the ab-component of the N.N. Mn-spins by the DM interaction.

3.4.3 Peculiar temperature hysteresis observed in nuclear reflections

The temperature hysteresis phenomena observed in the magnetization measurements may caused by some lattice distortions. Hence, I investigated the temperature dependences of the nuclear reflections at (1,1,0), (2,0,0) and (0,2,0) with changing the temperature in the following sequence: 305 K $\rightarrow$ 100 K $\rightarrow$ 9.6K $\rightarrow$ 100 K $\rightarrow$ 200 K $\rightarrow$ 305 K. Figure 3.30 shows the profiles of the nuclear reflections at the lowest temperature of 9.6 K. The intensity ratio of the nuclear reflection at (1,1,0), (2,0,0) and (0,2,0) and these calculation values are shown in Table 3.1. The

Table 3.1: Nuclear reflection intensity ratio. The normalized values of the calculation $I_{calc.}$ and observation $I_{obs.}$ are displayed.

h k l	$I_{obs.}$ (ratio)	$I_{calc.}$(ratio)
1 1 0	1.00	1.00
2 0 0	1.41	3.26
0 2 0	1.80	4.02

relative change of the observed intensity is smaller than the calculated one. This discrepancy may be caused by a secondary extinction effect.The temperature dependence of the integrated intensity ratio of the (1,1,0) reflection,which was measured in most detail, is shown in Fig. 3.31. The arrows represent the shift of the measurement temperature. The intensity measured in the warm-up process after the sample has been cooled to the helical phase below T_{N} distinctly larger than that in the cool-down process at 100 K. The behavior is very similar to the temperature hysteresis observed in the magnetizations. The same behaviors were also observed in the (2,0,0) and (0,2,0) reflections. For the sake of comparison, the same plot of the (1,1,0) reflection intensity measured in the neutron powder diffraction experiments are shown in Fig. 3.32. No difference of the intensities in the cool-down process and in the warm-up process was observed. In the temperature range of $T_{\mathrm{N}} \leq T \leq T_{\mathrm{C}}$, the reflections at the reciprocal lattice vectors consist of the nuclear contribution and the magnetic contribution because MnP has the ferromagnetic ordered moment. Hence, the hysteresis behavior above mentioned can originate from the magnetic contribution as well as the nuclear one. The difference of the nuclear reflection intensities in both processes measured with the single crystal sample is about 5 % at 100 K . On the other hand, the difference of the magnetizations is very small value of about $10^{-3}\mu_{\mathrm{B}}$/Mn-atom. Therefore, the nuclear contribution is responsible for the hysteresis behavior of the reflections at the reciprocal lattice vector. In the magnetization measurements, the temperature hysteresis phenomena

was observed in both the single crystal and the powder sample, and hence, even for the powder sample, the effect causing the hysteresis behaviors should emerges after cooling the sample below T_{N}. However, the hysteresis behavior in the nuclear reflections was observed only in the single crystal. A possible explanation of this inconsistency is that a reduction of the secondary extinction effect is the reason of the hysteresis behavior observed in the single crystal. The behavior of the (1,1,0) reflection intensity measured for the single crystal in the warm-up process is almost same as that measured for the powder sample. It suggests that the secondary extinction effect is suppressed when the sample has cooled to the helical phase once because some lattice distortion may be caused in the helical phase and the distortion remains still when the sample warmed up to higher temperature then T_{N} again. In the powder sample, there is no secondary extinction effect at first, and hence, no hysteresis was observed.

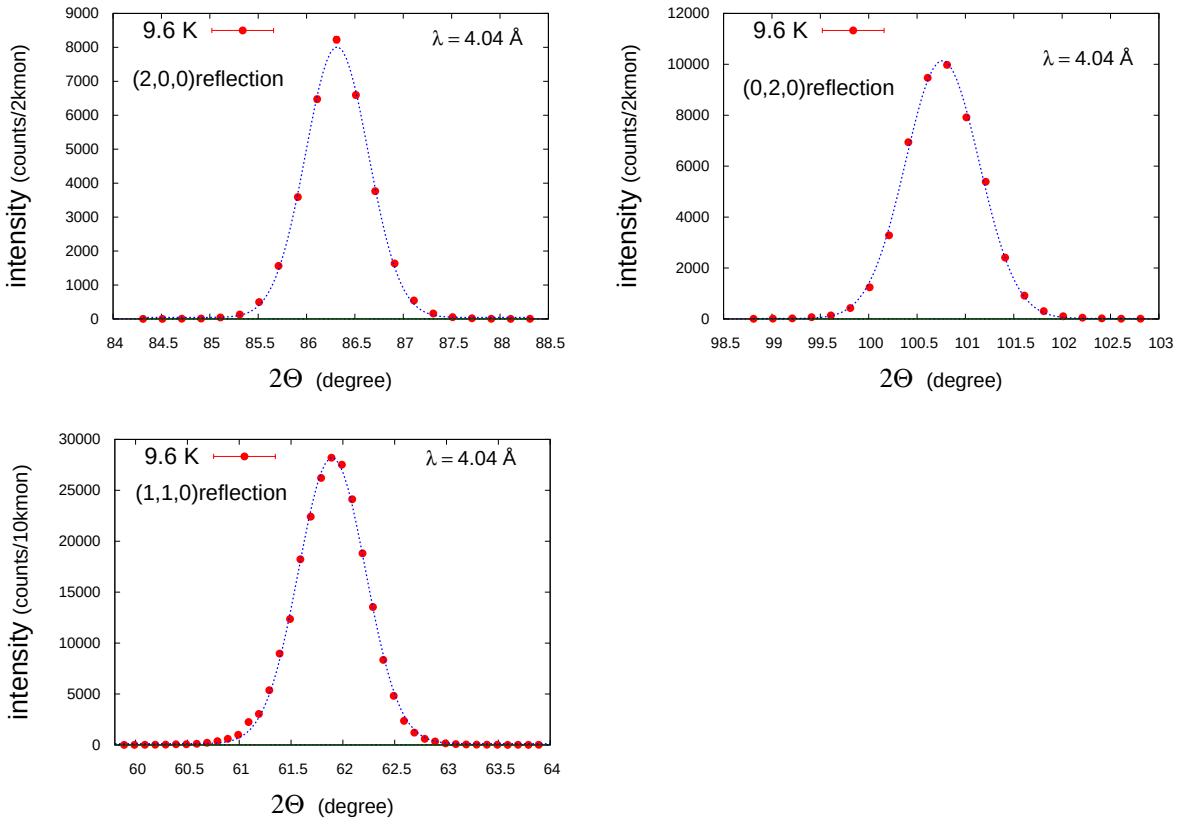

Figure 3.30: Profiles of the observed nuclear reflections at (2,0,0), (0,2,0) and (1,1,0).

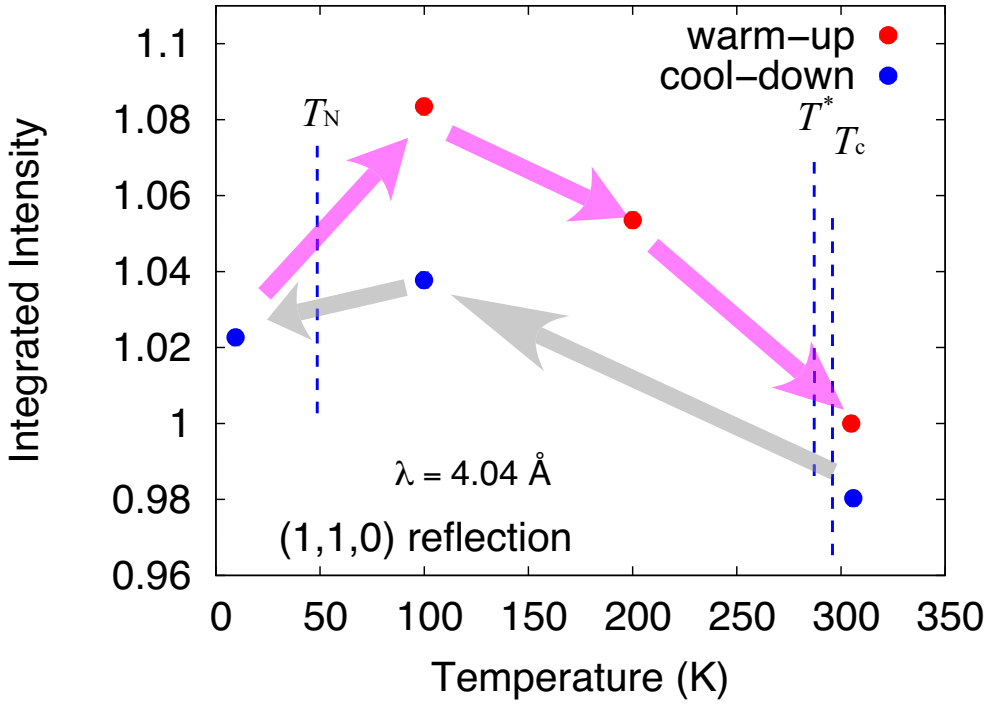

Figure 3.31: Temperature dependence of the relative intensity of the (1,1,0) reflection intensity measured for the single crystal of MnP.

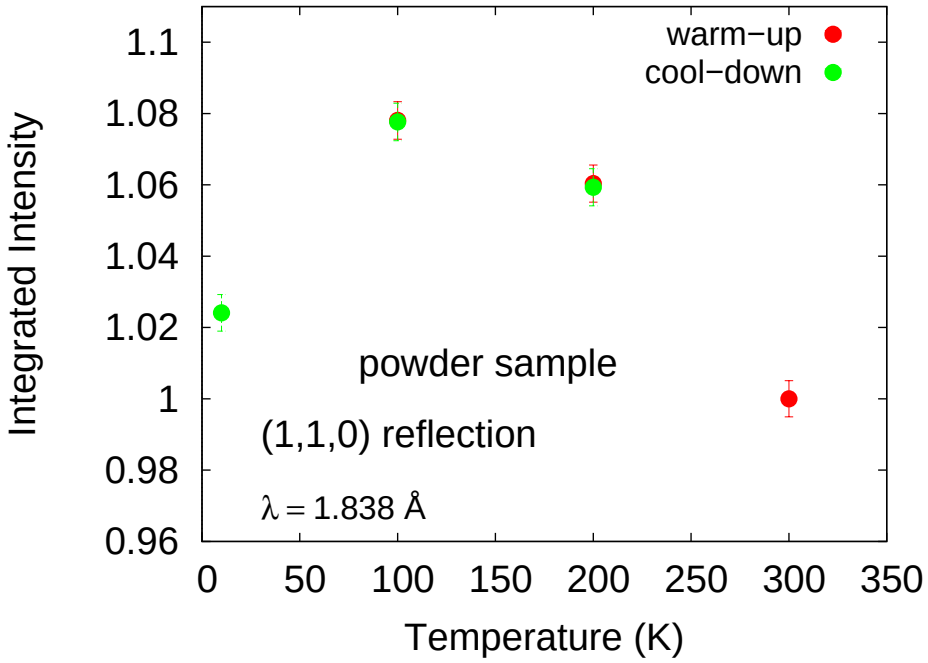

Figure 3.32: Temperature dependence of the relative intensity of the (1,1,0) reflection measured for the powder sample of MnP.

Chapter 4

Discussion

4.1 Possibility of the inverse effect of the DM interaction

The magnetic reflection of $(\delta, 1, 0)$ newly observed in the neutron scattering experiments indicates the tilted helical structure stabilized by the DM interaction below $T_{\rm N}$. It is the first observation of the effect of the DM interaction in MnP. The fact of that the DM interaction affects the low temperature magnetic structure strongly suggests that it should act also in the intermediate-temperature range. It supports my speculation about the intermediate-temperature phase described in subsection 3.1.5, namely, the weak ferromagnetism of the b-componet is a canted antiferromagnetism caused by the DM interaction. The cant angle θ is determined by the ratio of the DM interaction and the symmetric interaction $\theta \propto \tan^{-1}(D/J)$ in the canted structures. The cant angle θ should be the same as the tilt angle in the tilted helical stricture, the antiferromagnetic a-component in the intermediate-temperature phase is estimated at about $0.01\mu_{\rm B}$/Mn-atom for producing the canted ferromagnetic component along the b-axis of $1 \times 10^{-3}\mu_{\rm B}$/Mn-atom.

The peculiar temperature hysteresis phenomena, namely, some physical properties depend on whether cooling the sample to the helical phase or not once, suggests a strong relation between the intermediate temperature state and the low temperature state. Here, I discuss on the origin of the peculiar temperature hysteresis. With consideration of the experimental results and the interpretation of them, described in Chapter 3, I speculate the change of the magnetic state with changing the temperature in the cool-down process and in the warm-up process.

1. The antiferromagnetic a-component of the ordered moment emerges at $T_{\rm C}$, which is expected from the anomaly of the magnetization along the a-axis, as well as the ferromagnetic c-component does. The ordered moment is thought to be stabilized only by the symmetric interactions, in terms of the

crystal symmetry of MnP. In this state, however, the difference of the magnetizations along the a-axis in the ZFC and FC conditions are found, which suggest that the a-component of the ordered state is not simply a uniform antiferromagnetic one, and is very small.

2. When the sample is cooled to the temperature lower than T^*, the canted antiferromagnetic state is stabilized by the DM interaction as the antiferromagnetic a-components are canted to the b-direction. In other words, the vector chirality parallel to the c-axis $\boldsymbol{\chi}_{ij} = (0, 0, \chi^c_{ij})$ is induced by the DM vector parallel to the c-axis $\boldsymbol{D}_{ij} = (0, 0, D_{ij})$ due to the energy of the DM interaction rewritten as $E_{DM} = D_{ij}(S^a_i S^b_j - S^b_i S^a_j) = D_{ij}\chi^c_{ij}$. The canted antiferromagnetic state is nothing but the antiferro-vector-chiral state.

3. When the sample is cooled to the temperature lower than $T_{\rm N}$, the tilted helical state is realized, where the helical modulation of spins nearly lying in the bc-plane is stabilized by the competition of the symmetric interactions, and the helical planes are tilted to the a-direction with the angle of θ and $-\theta$ alternately by the DM interaction (see Figs. 3.27(b) and 3.28). In this phase, a much larger local vector chirality χ^c is induced by the DM interaction than that in the intermediate-temperature region because of the large b-component of the ordered moment, being $S^b \sim 1.3\mu_{\rm B}$. When the energy-gain of the DM interaction $E_{DM} = D\chi^c$ is larger than the loss of the elastic energy, the lattice is distorted to enhance the amplitude of the DM vector. It is just the inverse effect of the DM interaction observed in the multiferroic materials [7, 8, 11, 12]. This speculation is supported by the observation of the reduction of the secondary extinction effect in the neutron scattering experiment for the single crystal sample. If the domain formation accompanies the lattice distortion, the secondary extinction effect should be suppressed.

4. When the sample is warmed up to the intermediate temperature again, the state possess the larger ferromagnetic b-component of the ordered moment, that is the larger ferromagnetic vector chirality along the c-axis, than those in the cool-down process from the paramagnetic temperature induced by the enhanced DM vector. The enhancement of the DM vector is induced by the lattice distortion in the low temperature helical phase and remains even in the intermediate ferromagnetic vector-chirality phase because the lattice distortion still remains. It is supported experimentally by the observation of the reduction of the secondary extinction effect even above $T_{\rm N}$.

5. When the sample is warmed up to the paramagnetic temperature, the lattice distortion fades away. From the detailed magnetization measurement to

study the hysteresis behavior, I can conclude that the lattice distortion completely disappears above 330 K. The observation of the reduction of the secondary extinction effect in the neutron scattering experiments for the single crystal sample supports this conclusion.

The above story on the mechanism of the peculiar temperature hysteresis phenomena can be consistently explained the experimental results observed in both the magnetization measurements and the neutron scattering experiments. The noteworthy matters are that the lattice distortion is induced by the inverse effect of the DM interaction in the helical phase, and that the distortion remains up to $\sim$ 330 K. It can be the firstly observation of the inverse effect of the DM interaction in the metallic system.

4.2 Long-period kink structure model

Most of any experimental results can be explained by another model. It should be called as the long-priod kink structure model. In this model, I assumed the long-period structure, not the simple ferromagnetic state, below T^*, where the Mn-spins ferromagnetically align with forming the periodic alignment of long ferromagnetic domains as shown in Fig. 4.1. In the domain wall which is the kink of the structure, the directions of the spins change continuously. Considering the magnetic anisotropy in MnP, the spins should rotate nearby in the bc-plane in the magnetic domain wall and its rotating angle is $\pm(2n+1)\pi$ (n:integer). Recently, the similar structure stabilized by the DM interaction, the chiral kink crystal (chiral soliton lattice), was observed in the chiral magnets, e.g. CuB_2O_4 [53, 54, 55]. However, the driving force to stabilize the long-period structure in MnP is not clarified at all. With consideration of the crystal symmetry, the DM interaction is ruled out as a candidate of the driving force. It is a fatal weak point of the long-period kink model, however, this model is also attractive because this model can explain most of the experimental result elegantly.

The long-period kink structure as shown in Fig.4.1 is nearby the ferromagnetic structure , however, it is essentially an antiferromagnetic long-range order. The ultra-soft ferromagnetic behavior observed in the magnetization curve along the c-axis, namely, the spontaneous magnetization and the coercivity are not found, can be explained by this model because the magnetic state below T^* is not a ferromagnetic state but the antiferromagnetic state.

The weak ferromagnetic behavior of the magnetization along the b-axis can be interpreted as follows. In the long-period structure below T^*, the domain wall can be regarded as a small ferromagnetic domain for the b-direction and is responsible

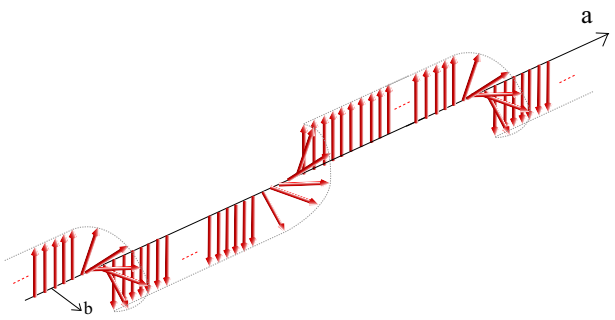

Figure 4.1: The schematic illustration of the long-period kink structure

for the weak ferromagnetic behavior. In the initial state, the domains whose moments are toward the +b-direction and the -b-direction are equally exists. When the applying the magnetic field, the domain-moment toward the opposite direction are flopped and the direction of the domain-moment is equal to the direction of the magnetic field. In this process, the energy-gain by the domain-moment-flops is very small because of its small moment, and hence, some field, coercivity, is needed to overcome the gap energy due to the magnetic anisotropy. As a result, the hysteresis loop can be observed in the $M - H$ curve along the b-axis.

In the domain for the b-direction, the antiferromagnetic a-component is also induced by the DM interaction. The most striking feature discovered in this story, the peculiar temperature hysteresis, can be explained by this model as follows. The magnetization along the b-axis in the long-period kink structure is determined by the number of the domain wall, in other words, by the period of the structure. Hence, the magnetization along the b-axis is enhanced if the period of the domain becomes comparatively shorter. It can be realized after undergoing the helical structure. Here, I assume that the local magnetic structure in the domain wall of the long-period kink structure is the same as the magnetic structure in the helical phase. In other words, the helical structure at low temperature is the structure where the domain wall completely spread out all over the sample. When warming-up the sample from the helical phase to the long-period kink structure phase again, more domain walls are pinned and the period becomes shorter than that of the state in the cool-down process from the paramagnetic temperature. The lattice in the domain wall may be distorted, and hence, the reduction of the secondary extinction effect is also explained by increasing of the number of the domain wall.

As mentioned above, we can interpret the temperature hysteresis phenomena by the different two models. One is "the inverse effect of the DM interaction" and

the other is "the long-period kink structure model". Both models can not be denied completely at present. I shall compare the two models.

1. At first, I discuss on the driving force of the magnetic phase transition at T^*. In the former model, the phase transition between the para-chiral state and the antiferro-chiral state occurs at T^*. and the DM interaction is the driving force of the phase transition. It is unclear why the spins are not canted in $T^* < T < T_{\rm C}$, in spite of the existence of the antiferromagnetic a-component of the ordered moment. It may come from the competition and the symmetric interactions. On the other hand, in the latter model, the driving force of the the long-period kink structure is completely unknown.

2. In these models, the relationship of the a-component and the b-component of the ordered moment in the intermediate temperature phase is opposite. In the former model, the antiferromagnetic a-component arises primarily, and it is canted to the b-direction by the DM interaction. Hence, the a-component is the primary one. In the latter model, the b-component primarily arises in the domain wall, and it is canted to the a-direction and -a-direction alternately by the DM interaction. Hence, the b-component is the primary one.

It is a great advantage for the model of the inverse effect of the DM interaction that the driving force of the phase transition at T^* is clearly known. The hysteresis behavior of the magnetization along the b-axis is completely restored at $T_{\rm C}$, whereas, that along the a-axis remains above $T_{\rm C}$. It implies that the a-component of the ordered moment is primary one. This result also give an advantage to the model of the inverse effect of the DM interaction. Therefore, I propose that the origin of the peculiar temperature hysteresis phenomena is the inverse effect of the DM interaction.

Chapter 5

Conclusion

I discovered the following two novel chiral structures stabilized by the DM interaction in MnP.

1. The tilted helical structure below T_{N}, where the helical planes are tilted to the a-direction from the bc-plane with angles of θ and $-\theta$ alternately by the DM interaction. This structure is a modulated ferro-chiral structure, where the total vector-chirality is nearly along the a-axis and the small modulation of the c-component is induced by the DM interaction.

2. The canted antiferromagnetic state in the $T_{\mathrm{N}} < T < T^{*}$, where the antiferromagnetic ordered moment along the a-axis is canted to the b-direction by the DM interaction and the weak ferromagnetic moment along the b-axis of about $10^{-3}\mu_{\mathrm{B}}$/Mn-atom appears. This structure is nothing but a antiferro-chiral structure, where the vector-chirality is along the c-axis.

Moreover, I discovered the peculiar temperature hysteresis phenomena as below.

- The spontaneous magnetization of the canted antiferromagnetic state is remarkably enhanced when the sample has cooled to the helical phase temperature once.

- The nuclear reflections, in the neutron scattering experiments for the single crystal, also enhanced when the sample has cooled to the helical phase temperature once.

I propose that the temperature hysteresis phenomena is caused by the lattice distortion induced by the inverse effect of the DM interaction, namely, the vector chirality in the helical phase distorts the lattice via the inverse effect of DM interaction and the distortion remains even when the sample is warmed up to the

intermediate temperature again. It can be the first observation of the inverse effect of the DM interaction in the metallic system.

Part II

Slow dynamics in helical magnet $\mathbf{Gd}_{1-x}\mathbf{Y}_x$ alloy

Chapter 6

Introduction

6.1 Electric current driven magnetization dynamics in helical magnets

The chirality driven Hall effect, which was also mentioned in the Sec. 1.1, is a effect that the chiral order affects a force to conduction electrons and consequently bends the orbits of the conduction electrons via the Berry phase. As a reaction of the force, the spin transfer torque which is the effect that the spin-polarized conduction electron (the spin current) exerts a torque to the local spins of the chiral structure was proposed theoretically[56]. After that, the vigorous studies for manipulating the magnetization using the spin transfer torque have been performed. The spin current is a current of the angular momentum, cf. electric current is a current of the charge. The spin current can transfer the angular momentum to the local spin, and result in the torque arising. This spin transfer mechanism is expected for the operating principle of the next generation magnetic devices. The radically new storage memory device, the magnetic race-trac, using spin current has been already proposed by IBM[57]. One of the representative phenomena caused by the spin transfer torque is the electric current driven domain wall motion. The possibility of the charge current driven domain wall motion was firstly proposed by Berger in about 1980[58, 59, 60]. Figure 6.1 shows the schematic image of the electric current driven domain wall motion in a ferromagnetic material. The area where the magnetic moments gradually change its direction in Fig. 6.1(a) represents the domain wall. When electric current is generated in this metal, the spins of the conduction electrons are polarized toward same direction as local spins, hence, the spin directions of the conduction electrons change gradually in the wall (see Fig. 6.1(b)). The difference of the moments of the conduction electrons transforms to the local moments, that is, the local moments in the domain wall rotate. Finally,

the domain wall moves to the opposite direction to the electric current(see Fig. 6.1(c)). In recent years, this phenomena was experimentally observed by inducing the pulse current to the ferromagnetic nano wire[61, 62]. In these experiments, the very high current density of approximately 10^8 A/cm^2 was needed for the domain wall motion, it is the issue for the application. It has been theoretically derived that the threshold current density for the domain wall motion is proportional to the magnetic anisotropy[63]. Since the magnetic anisotropy can be controlled by the sample shape, the studies for reducing the threshold current in terms of that[64].

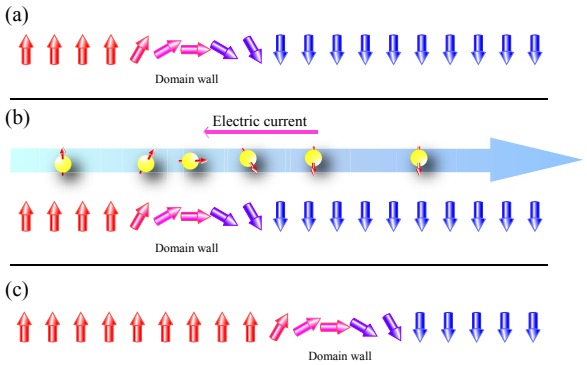

Figure 6.1: Schematic image of the electric current driven domain wall motion in a ferromagnetic metal.

The most of the phenomena caused by the spin transfer torque including the current driven domain wall motion is the microscopic one. Recently, the phenomena in bulk metals, however, was theoretically shown by Wessely *et al*[65]. From their theory, the electric current through a bulk metal with a helical structure induces a spin transfer torque, which gives rise to a rotation of the spins with keeping the helix. The schematic image of the phenomena is shown in Fig. 6.2. In order to quantify this effect, they calculated the spin transfer torque for the rare earth helical magnets. The calculations are based on calculations of the spin flux using the spin current density tensor $\boldsymbol{Q}$ given by

$$\boldsymbol{Q}_{n\boldsymbol{k}}(\boldsymbol{r}) = \mathrm{TrRe}\{\psi^{\dagger}_{n\boldsymbol{k}}(\boldsymbol{r}) \otimes \hat{v}\psi_{n\boldsymbol{k}}(\boldsymbol{r})\}. \tag{6.1}$$

$$\tag{6.2}$$

$\boldsymbol{S}$: spin operator
$\hat{v}$: velocity operator
n : band

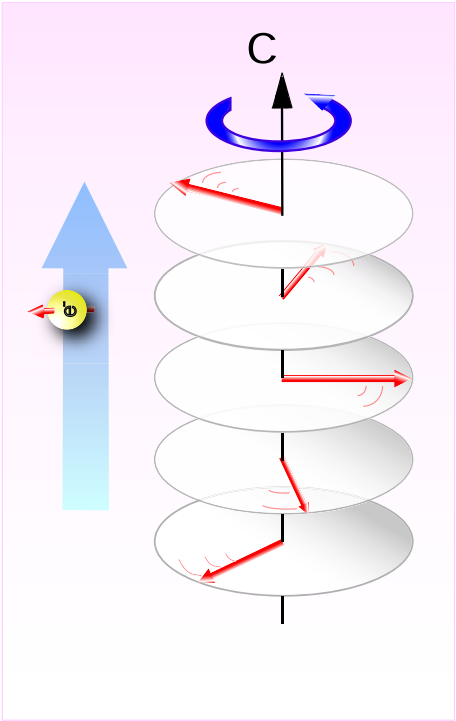

Figure 6.2: Schematic image of the electric current driven spin dynamics in helical magnetic metal.

$\boldsymbol{k}$: wave vector
The torque extended by an electric state with band index n and wave vector k on the angular momentum within a volume V encolesed by the surface S is given by its spin flux into V,

$$\int_s \boldsymbol{Q}_{n\boldsymbol{k}} \cdot d\boldsymbol{S} = -\frac{\partial \boldsymbol{J}_{n\boldsymbol{k}}}{\partial t}. \tag{6.3}$$

They calculated the torque current tensor C for the rare earth helical magnet Er, which has a conical spin structure below 20 K. Although the formalism is valid for conical structure, in this paper they focussed on the planar spin spirals. All the material specific quantities of Er used in the calculation of the tensor C were calculated from first principle density functional theory. The calculation was made using the noncollinear Full-potential-augmented plane wave(APW) + local orbitals method. As a result of their calculation, they concluded that the torque induced by a current along the spiral axis causes the helix to translate along the spiral axis,

which is equivalent to a rigid rotation of the helix with the rotation frequency

$$|f| = (1/2\pi J\hbar)\sqrt{(C_{23}j_3)^2 - (6K_6^6)}. \tag{6.4}$$

Where J is total angular momentum ($J = 15/2$ for Er), $C_{23}$is a finite component of the torque current tensor contributing the spin rotation, K_6^6 is hexagonal magnetic anisotropy, j_3 is a current density along the helical axis. The eq. 6.4 implies that the helical rotation frequency will scale linearly with the current density along the helical axis for current densities significantly larger than the critical current, $j_{3c} = 6K_6^6/C_{23}$. If current of $j_3 = 10^7$A/cm^2 flows along the helical axis of bulk Er, the rotation with the frequency of 0.07 GHz is expected from their calculations.

Since the critical current density, $j_{3c} = 6K_6^6/C_{23}$, is depends on the magnetic anisotropy, the rotation can be induced by smaller current density in the materials with smaller magnetic anisotropy. A favorable candidate material for the observation is the $Gd_{1-x}Y_x$ alloy. The $Gd_{1-x}Y_x$ alloys exhibit a proper type helical structure in $x > 0.30$. It has a very small in-plane anisotropy because Gd^{+3}-ion has no orbital angular moment($L = 0$). The observation of the electric current driven spin dynamics by very smaller current can be expected in $Gd_{1-x}Y_x$. In order to observe this phenomena, I performed the AC susceptibility measurements along the in-plane direction with applying electric current parallel to the helical axis in $Gd_{1-x}Y_x$. When the frequency of the applied AC magnetic field is equal to the rotation frequency, a dissipative behavior, increase of the imaginary part of the AC susceptibility χ'' , would be observed.

6.2 Crystal structure and magnetic properties of $Gd_{1-x}Y_x$ alloy

The crystal structure of the $Gd_{1-x}Y_x$ alloys is hexagonal closed-pack one and its space group is $P6_3/mmc$, where the lattice parameters are independent from Y concentration x and $a = 3.54$ Å, $c = 5.76$ Å[66]. The magnetic ion Gd^{+3} has the magnetic moment of $S = 7/2$ and $L = 0$. Gd is a well known ferromagnetic material and the curie temperature is $T_C = 292$ K, though it has been discussed recently whether the Gd is really ferromagnetic or not[67, 68].

The $Gd_{1-x}Y_x$ alloys exhibit various magnetic ordered states [69]. The magnetic phase diagram of the $Gd_{1-x}Y_x$ alloy series In the x range of $0.20 < x < 0.40$ is shown as shown in Fig.6.3. In this diagram, it is shown following three magnetic ordered phase: (ferro-I) the ferromagnetic phase where the spins parallel to the c-axis; (ferro-II) the canted ferromagnetic phase where the spins are canted from c-axis with the cant angle dependent on the temperature; (basal plane helix) the simple proper type helical phase where the spins are confined to the hexagonal basal

plane. $Gd_{1-x}Y_x$ has been well studied for the possibility the two multi-critical points in Fig. 6.3 would be Lifshitz points [70, 71, 72, 73, 74]. The stability of the helical structure is explained by the nesting of the Fermi surface in $Gd_{1-x}Y_x$ alloys [75], and the both handed helicity domains are exists. The x-dependence and the T-dependence of the turn angle were investigated [76, 69]. In the case of the $Gd_{0.62}Y_{0.38}$, which is used in this study, the turn angle gradually decrease with cooling the sample from the helical magnetic transition of $T_N \sim 200$ K to the ferromagnetic temperature of $T_C \sim 100$ K which is the second order transition to the ferro-II phase.

6.3 Purpose of this study

The main purpose of this study is to observe the current induced spin dynamics in bulk single crystal of the $Gd_{1-x}Y_x$.

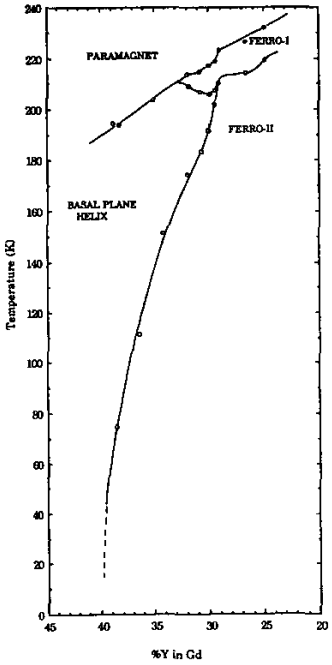

Figure 6.3: Magnetic phase diagram of the $Gd_{1-x}Y_x$ alloy series.

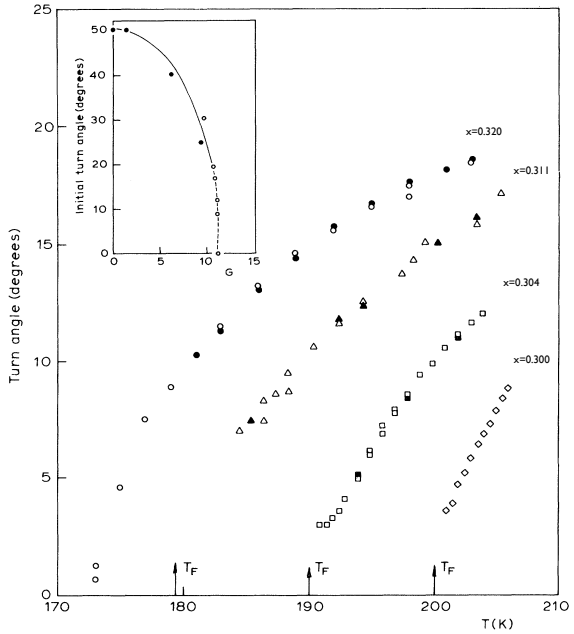

Figure 6.4: Temperature dependence of the helical turn angle θ in the $Gd_{0.62}Y_{0.38}$ of $x = 0.320, 0.311, 0.304, 0.300$.

Chapter 7

Experimental procedures

7.1 Sample preparations

For the present study, I have provide the single crystalline sample of the $Gd_{0.62}Y_{0.38}$ and poly crystalline samples of the Ho and $Ho_{0.60}Y_{0.40}$. The elements of nominal amounts for the given x were melt together in an argon arc furnace. The element materials Gd, Ho, and Y were purchased from Nippon Yttrium Co.,Ltd, and these purity are 3N. The single crystal was grown by using the Czochralski's pulling method with a tetra-arc furnace. The single crystal wrapped in a Ta film was sealed in the quartz tube, under high vacuum, and annealed in a electric furnace for seven days at 973 K and then quenched in cold water. The crystallographic axes were determined by X-ray back Laue methodd using the apparatus installed at Inui laboratory in depertment of Materials science and Engineering faculty of Engineering Kyoto university.

The magnetic phase temperatures $T_{\rm N}$ and $T_{\rm C}$ estimated by the anomaly of the AC-susceptibility measurements were $T_{\rm N} = 198$ K and $T_{\rm C} = 155$ K, respectively. They are appropriate to that of the Y concentration x being approximately 0.34 in the previous reports as shown in Fig.6.3. The concentration gradient of the Y concentration in the sample is inevitable in growing a crystal of solid solution by the pulling method. However, It would not be a problem for our measurements because the quantitative magnetic property does not change in this x-range of $0.34 < x < 0.38$. The shaping of the samples were done by using the spark cutting machine installed at Inui laboratory in depertment of Materials science and Engineering faculty of Engineering Kyoto university. The sizes of the samples are listed in Tab. 7.1

Table 7.1: The sample list of $Gd_{0.62}Y_{0.38}$, Ho and $Ho_{0.60}Y_{0.40}$

sample neme	experiment	a* (mm)	a* (mm)	c* (mm)
GdY-1	AC- and DC-susceptibility // a*	0.88	0.30	1.88
GdY-2	AC-susceptibility // c*	0.38	0.20	1.88
sample neme	experiment	w (mm)	d (mm)	t (mm)
Ho	AC-susceptibility	0.5	0.5	9.0
HoY	AC-susceptibility	0.5	0.5	9.0

7.2 AC- and DC-magnetization measurements

AC- and DC- magnetization measurements were performed by using three units of the SQUID-magnetometer (MPMS, Quantum Design) installed at Research center for low temperature and materials sciences Kyoto university. The details were mentioned in Sec.2.2.

7.3 AC-susceptiblity measurement with applying electric current

In order to measure the AC-susceptibility with applying electric current in SQUID-magnetometer MPMS, I made my own sample stick as shown in Fig.7.1. Four Cu lead lines of 0.3 mmϕ go through in the sample rod. Two lines of those were used for inducing the current in the sample. The others were used for generating short-circuit current of the same magnitude and opposite direction to the current in the sample so that the magnetic flux produced by current in the closed circuits were canceled out.

$Gd_{1-x}Y_x$ alloys are liable to be oxidized, therefore, the contact resistance would be too large ($> 2\Omega$) if the Ag-paste extensively used for resistivity measurements is done. The heat generated by current is a problem. Accordingly, The Al-wire bonding was operated for connecting the sample by using a ultrasound wire bonder machine(Ultrasonic Engineering Co.,Ltd., USW). The thickness of the Al-wire is $25\mu m\phi$ and as many wire as possible, $8 \sim 10$ wires / side, was bonded. The electric current was generated by the current source (Yokogawa electric corporation, PA1811) in the range of 0 A $\leq I \leq$ 1.0 A.

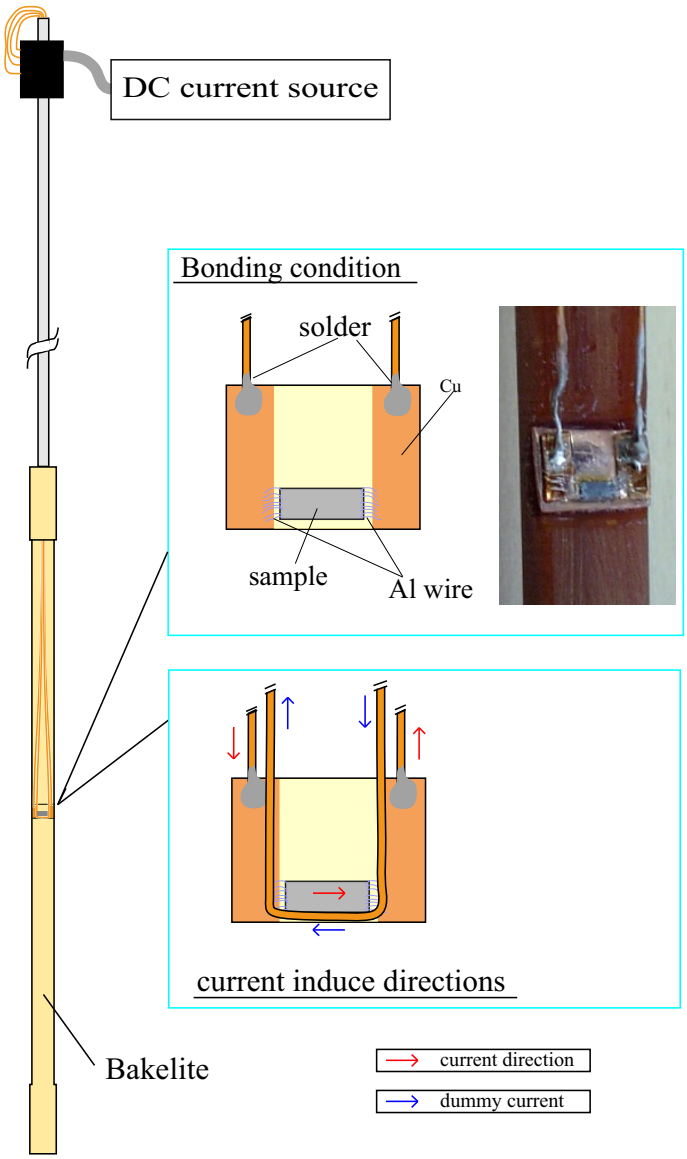

Figure 7.1: The schematic view of my own sample stick for AC-susceptibility measurements with applying electric current in the sample

Chapter 8

Experimental results and discussions

8.1 Bulk effect of spin transfer torque in $Gd_{1-x}Y_x$ alloy

8.1.1 AC-susceptibility

Figure Fig. 8.1 shows the temperature (T) dependence of the real and the imaginary parts of the AC susceptibility , χ' and χ'', in the $Gd_{0.62}Y_{0.38}$ alloy with applying the AC field along the a*- and c*-directions, being in- and perpendicular to the helical plane. The cusps of the χ' at $T_{\rm N} = 198$ K were observed, and the χ' is once decrease and increase again ferromagnetically with decreasing temperature below $T_{\rm N}$. The AC-field $h_{\rm AC}$ is 3 Oe and the frequency of 10Hz. In the helical plane, the sharp peak of the χ'', which indicate the critical slowing down at the ferromagnetic phase transition temperature, was observed. Accordingly, it can be determined the ferromagnetic phase transition temperature $T_{\rm C}$ is 155 K. On the other hand, the peak of the χ'' perpendicular to the helical plane was much smaller. The χ' along each axis crossed each other just at $T_{\rm C}$, which is the reasonable behavior because the susceptibility along the easy magnetization plane become smaller than that along the hard axis in the antiferromagnetic state. The behavior of the χ'' at $T_{\rm N}$ and in the T- range of the helical magnetic phase should be noted. In the helical plane, the remarkable increase of the χ'' was observed in the T- range of the helical magnetic phase and it became very sharp at $T_{\rm N}$. On the other hand, the increase of the χ'' perpendicular to the helical plane was much weaker. These behavior is discussed later in this thesis.

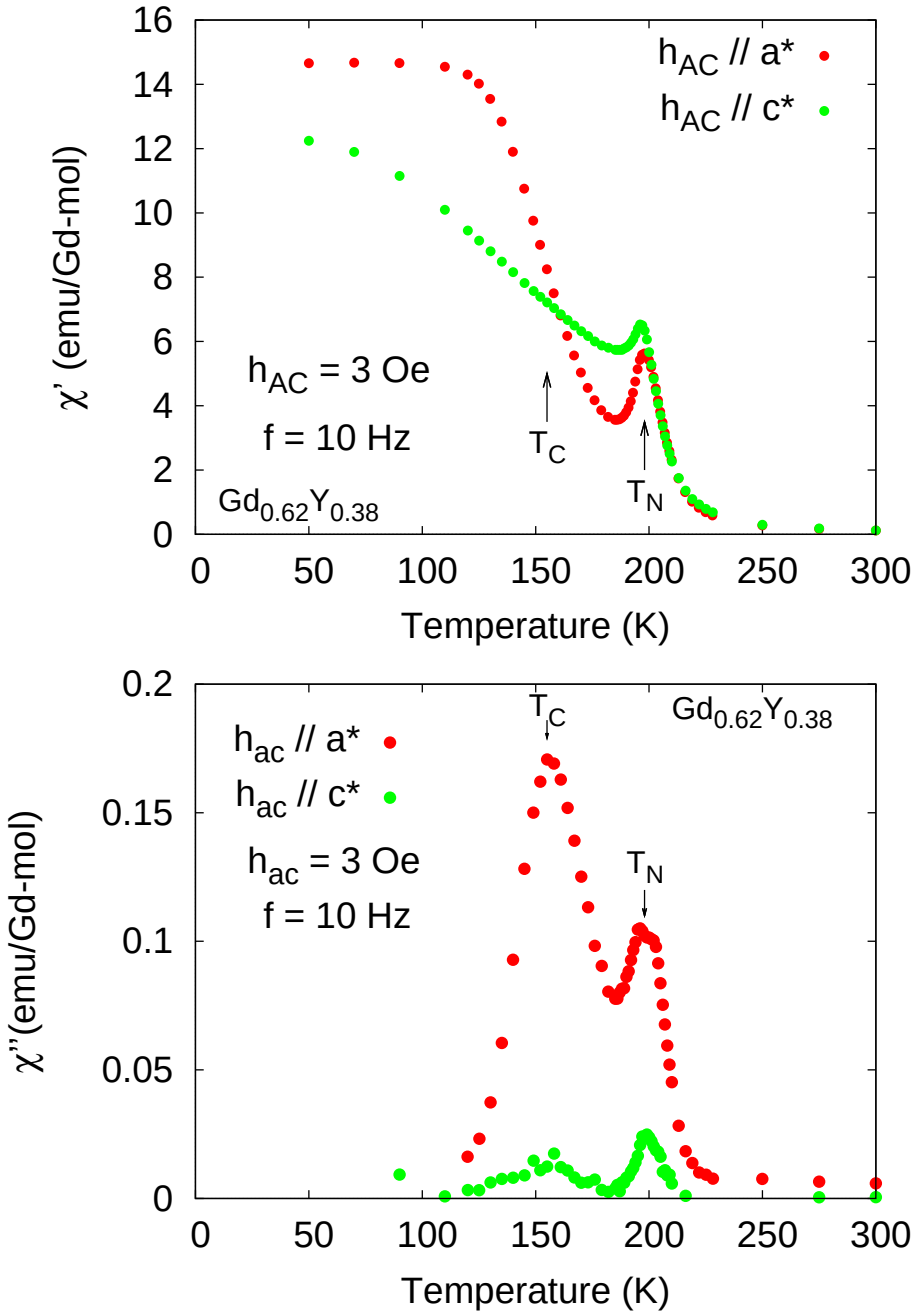

Figure 8.1: The temperature dependence of the real and the imaginary parts of the AC-susceptibility, χ' and χ'', in the $Gd_{0.62}Y_{0.38}$ alloy with applying the AC field along the a*- and c*-directions, being in- and perpendicular to the helical plane.

8.1.2 AC-susceptibiity with applying electric current

In order to observe the electric current driven spin dynamics, the AC-susceptibility measurements along the a*-direction, being in-helical plane, with applying electric current I along the c*-direction, being parallel to the helical axis, were performed in $Gd_{0.62}Y_{0.38}$ alloy. When the electric current is applied, the magnetic flux arrises in the closed circuit. The dummy current I_d with opposite direction was induced beside the sample so that the magnetic fluxes arose from I and I_d were canceled out each other (see inset of Fig.7.1).

At first, the I-dependence of the AC-susceptibility measurements along the were performed at the helical magnetic phase temperatures of 160 K and 185 K. In this measurements, AC-field is 3 Oe and the frequency of 1Hz, and no dummy current was induced. The results are shown in Fig. 8.2.

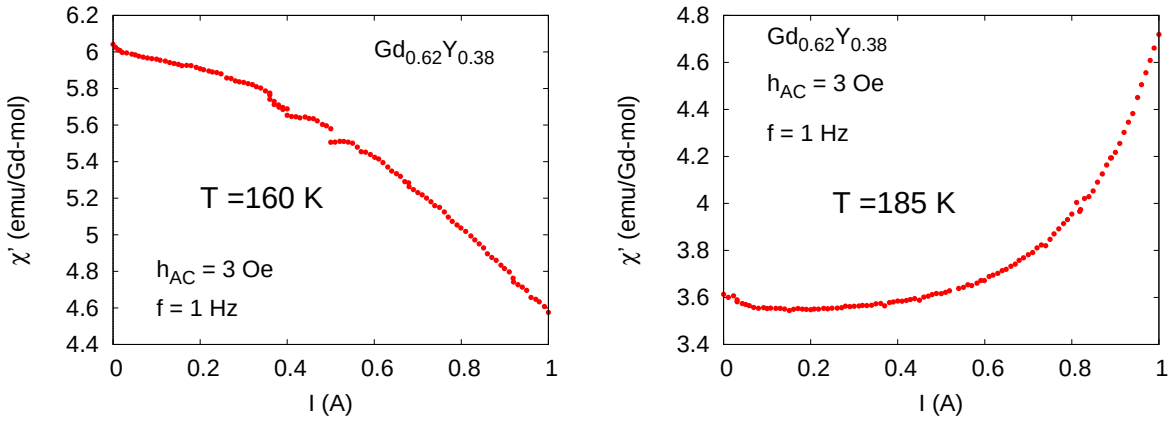

Figure 8.2: The electric current dependence of the real part of the AC-susceptibility χ' at 160 K and 185 K.

The χ' decreases at 160 K and increases at 185 K with increasing the electric current I. These behavior It is guessed that these behaviors of the χ' were caused by the Joule heating in the sample because the tendency of the T-dependence of the χ' as shown in Fig.8.1 is consistent to that of the I-dependences of the χ'. Thus, it was found that the measurements at the fixed temperature is difficult because of the temperature increase in the sample.

Figure 8.3 shows the temperature dependences of the AC-susceptibility along the a*-direction measured with applying the electric current along the c*direction ($I//I_d//c^*$). The measurements were performed in the following electric current condition: $I = I_d = 0$ A (no current); only the dummy current of $I_d = -0.5$ A and $I_d = -1.0$ A; opposite currents of $I = -I_d = 0.5$ A and $I = -I_d = 1.0$

A. In this measurements, AC-field is 3 Oe and the frequency of 10Hz. Corrected temperatures, however, are shown in Fig.8.3 because increasing of the sample temperature caused by the Joule heating were observed. The temperature corrections were done on the basis of the assumption that the temperature change is a constant, depending only on the current, in the whole T-range. The shown temperatures have been shifted from the temperature controlled by MPMS system so that the real parts χ' of the each measurement become equal to that measured with zero current above 210 K. The shifted temperatures ΔT of each measurement condition are listed in Tab. 8.1. 5Since the real parts χ' are well collapsed not only above

Table 8.1: The temperature shift caused by the Joule heating

I (A)	I_d (A)	ΔT (K)
0	-0.5	0.2
0	-1.0	0.4
0.5	-0.5	2.3
1.0	-1.0	9.1

210 K but also below T_{C} in Fig.8.3, we can see that the above assumption is an acceptable one. The suppression of the χ' was observed around the T-range of the helical magnetic phase with increasing electric current I, and it was remarkable particularly around T_{N}. On the other hand, the suppression of the χ' was not observed when inducing only dummy current I_d. It is indicate that the reduction of the χ' is caused by the electric current induced in the sample. The suppression of the chi'' was also observed. The chi'' is slightly suppressed even with increasing the I_d and remarkably done with increasing the I. Although these behaviors of the AC-susceptibility are caused by the electric current, It is needed to confirm caused by whether the spin transfer torque effect of the electric current or not. In order to confirm it, I performed the same AC-susceptibility measurements with applying the electric current perpendicular to the helical axis. In this condition, the spin dynamics would not be induced.

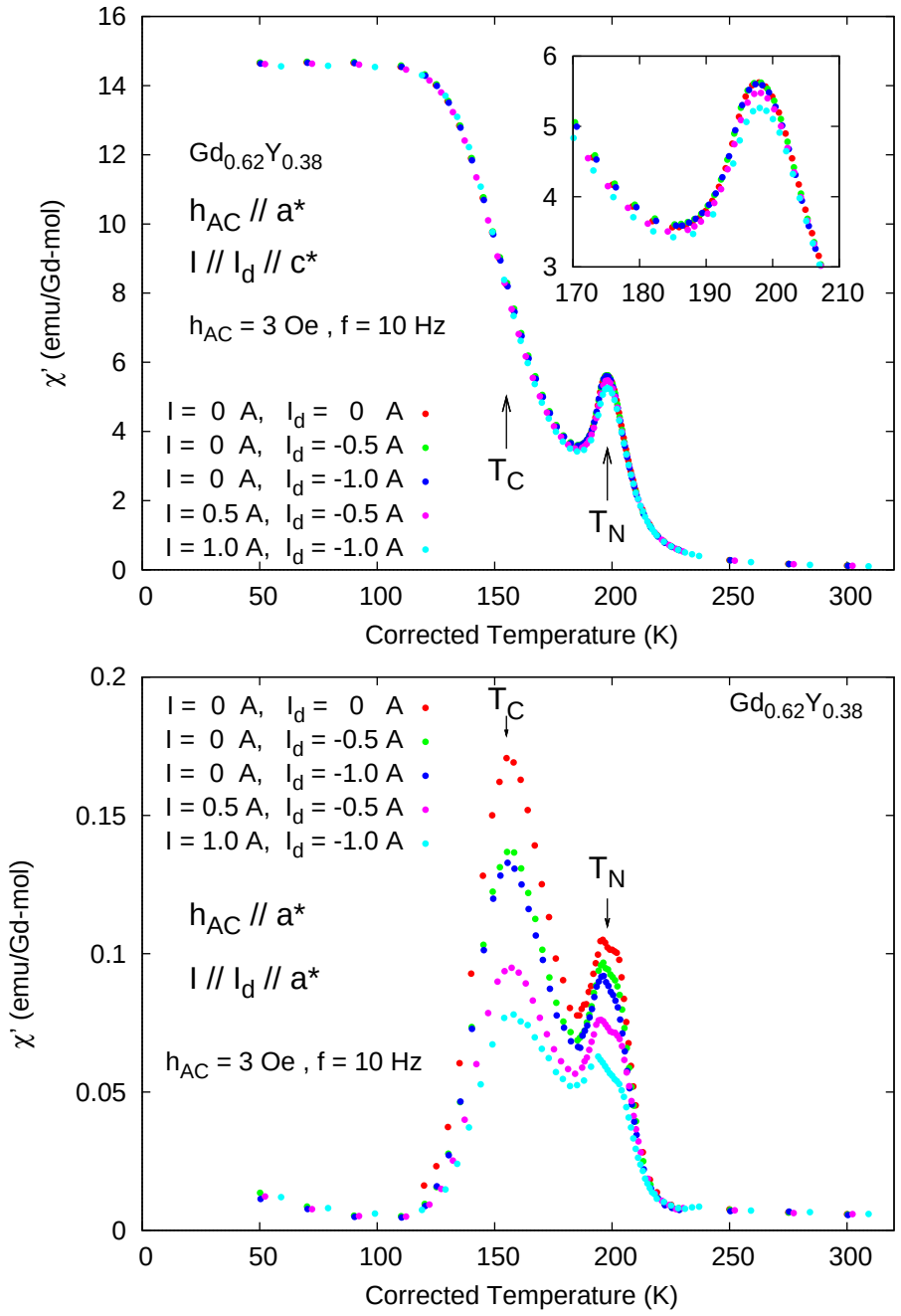

Figure 8.3: The temperature dependences of the AC-susceptibility along the a*-direction measured with applying the electric current along the c*direction

Figure 8.4 shows the temperature dependences of the AC-susceptibility along the a*-direction measured with applying the electric current along the a*direction ($I//I_d//a^*$), being in the helical axis. The measurements were performed in the electric current condition of $I = I_d = 0$ A (no current), and opposite currents of $I = -I_d = 0.5$ A and $I = -I_d = 1.0$ A. The temperature shifts ΔT were 1.9 K and 7.3 K when the electric currents are 0.5 A and 1.0 A, respectively. The back ground of the χ'' caused by the Eddy current effect was observed and represented to the dashed line in the figure. The suppression of the χ' was observed even when the electric current along the parallel to the helical axis is applied. In this case, it was observed only around $T_{\rm N}$, which is different from the case of ($I//I_d//c^*$). The suppression of the χ'' was also observed.

8.1.3 Discussion

Although the change of the AC-susceptibility caused by applying the electric current was observed, it was found when the applied current is both parallel and perpendicular to the helical axis. Therefore, the change can be caused by the different origin from the electric current driven spin dynamics. A candidate origin is a magnetic field accompanying the electric current. The magnetic moments in the surface of the sample can feel the magnetic field. I roughly estimated the magnetic field accompanying the electric current in the surface. When a electric current of 1 A passes through the center of the sample, a produced magnetic field at the the nearest point from the center with the distance of $r = 0.15$ mm is given by the ampere's low

$$H = \frac{I}{2\pi r} \fallingdotseq 1061 \ [\mathrm{A/m}] \fallingdotseq 13[\mathrm{Oe}].$$

In order to illuminate the influence of the DC-field(H) on the AC-susceptibility in the $Gd_{0.62}Y_{0.38}$ alloy, the AC-susceptibility measurements with applying the DC-field H was performed. Figure 8.5 shows the temperature dependences of the AC-susceptibility along the a^*-direction measured with applying the DC-field, $H = 0, 10, 20, 100$ Oe. The χ' and χ'' were strongly suppressed by the small DC-field, $H \leq 100$ Oe, in the T-range of about 120 K $< T <$ 220 K. The behaviors of the χ' and χ'' measured with applying the DC-field of 10 Oe are similar to that measured with applying the electric current. At last, the suppressions of the χ' and χ'' by applying the electric current as shown in Fig.8.2 can be effects of the spin transfer torque, however, the effect of the magnetic field accompanying the electric current can not be eliminated.

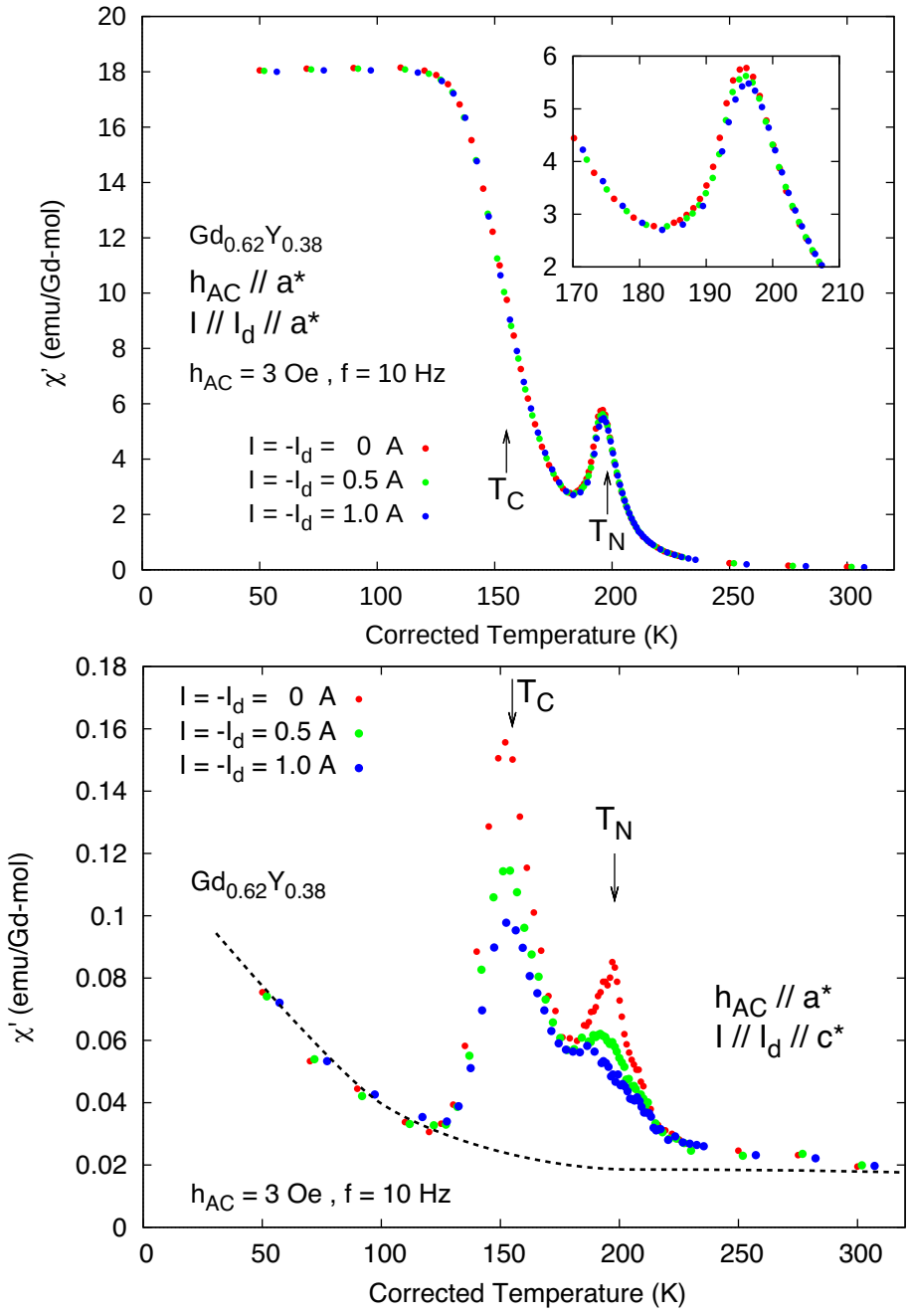

Figure 8.4: The temperature dependence of the AC-susceptibility along the a*-direction measured with applying the electric current along the a*direction.

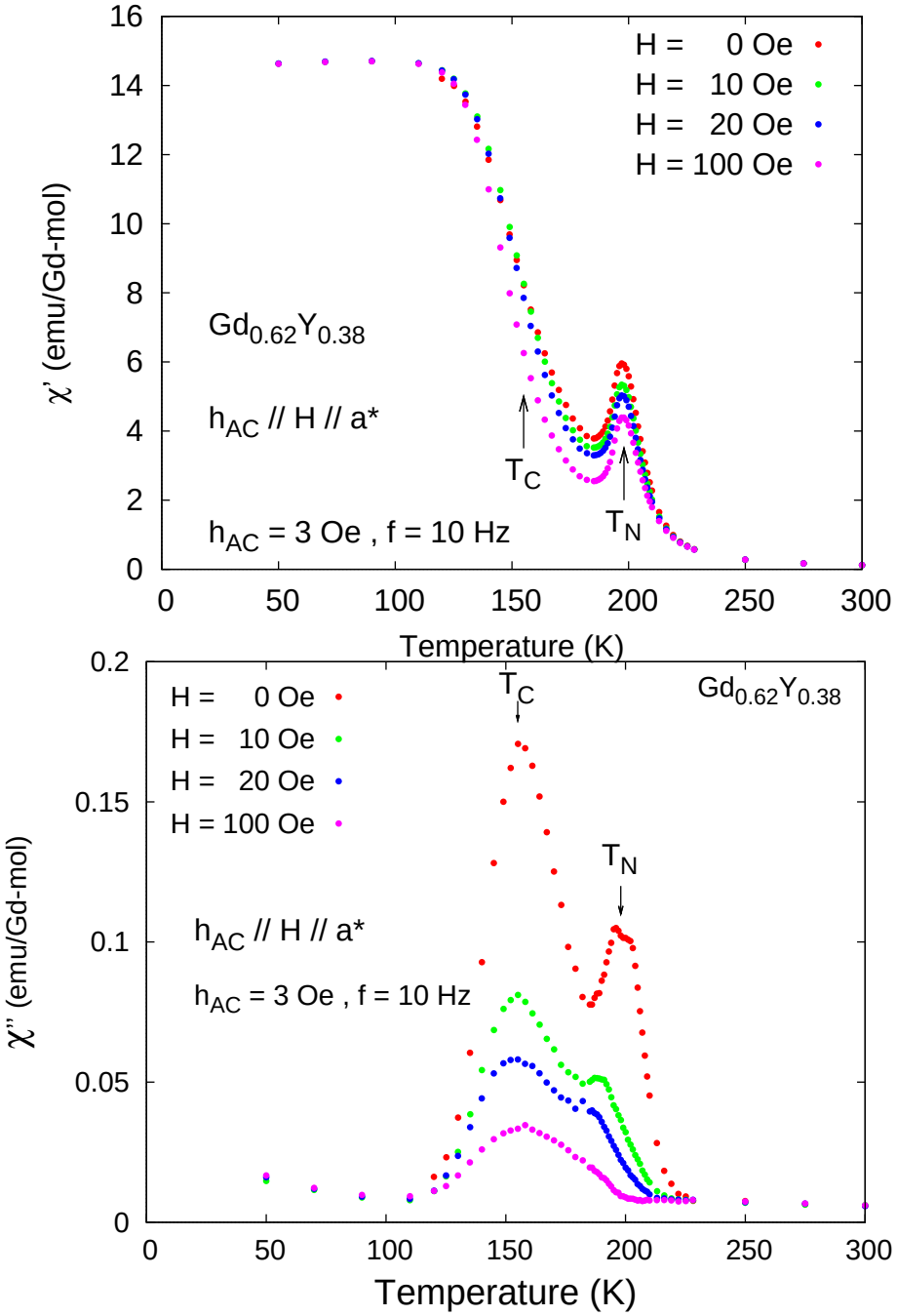

Figure 8.5: The temperature dependence of the AC-susceptibility along the a^*-direction measured with applying the various DC-field.

8.2 Slow dynamics in helical phase in Gd_{1-x}-Y_x alloy

8.2.1 AC-susceptibility

The behavior of the χ' observed around T_N in Fig.8.5 suggests the strong nonlinearity of the AC-magnetization for the magnetic field. It is well known that such a strong nonlinearity at the phase transition temperature is observed in the spin glasses, however, the observation of that at the helical magnetic phase transition temperature is nontrivial and interesting. Moreover, the increase of the χ'' in the T-rage of the helical phase and the suppression of that by applying the magnetic field is also nontrivial and interesting. Here, I investigate the nonlinearity of the AC-magnetization and the origin of the increase of the χ''.

Figure 8.6 shows the temperature dependences of the AC-susceptibility along the c^*-direction, being perpendicular to the helical plane, measured with applying the DC-field, $H = 0, 10, 20$ and 100 Oe. The nonlinearity of the AC-magnetization and increase of the χ'' in the T-range of the helical phase were also observed in perpendicular to the helical plane, however, it was weaker than those in the helical plane.

Next, for the quantitation of the nonlinearity, the nonlinear susceptibility χ_2 was estimated from the data shown in Fig.8.5 and 8.6. If the h_{AC} is regarded as being very smaller than H, the χ' can be treated as the differential magnetization and given by

$$\chi' \simeq \left.\frac{\mathrm{d}M}{\mathrm{d}H}\right|_{H=H_{DC}} = \chi_0 + 3\chi_2 H^2 + 5\chi_4 H^4 + \cdots , \tag{8.1}$$

and then the nonlinear susceptibility χ_2 was estimated from the slant of the χ' vs H^2 plots in the limit of $H^2 \to 0$. In this time, the demagnetization correction was operated by using the coefficient $N \fallingdotseq 0.61$, which was calculated from the shape of the sample. The temperature dependences of the χ_2 along the a*- and the c*-directions are shown in Fig.8.7. In the helical plane, a negative divergent peak of the χ_2 was observed at T_N. On the other hand, the peak of the χ_2 perpendicular to the helical plane was observed, however, it was much weaker.

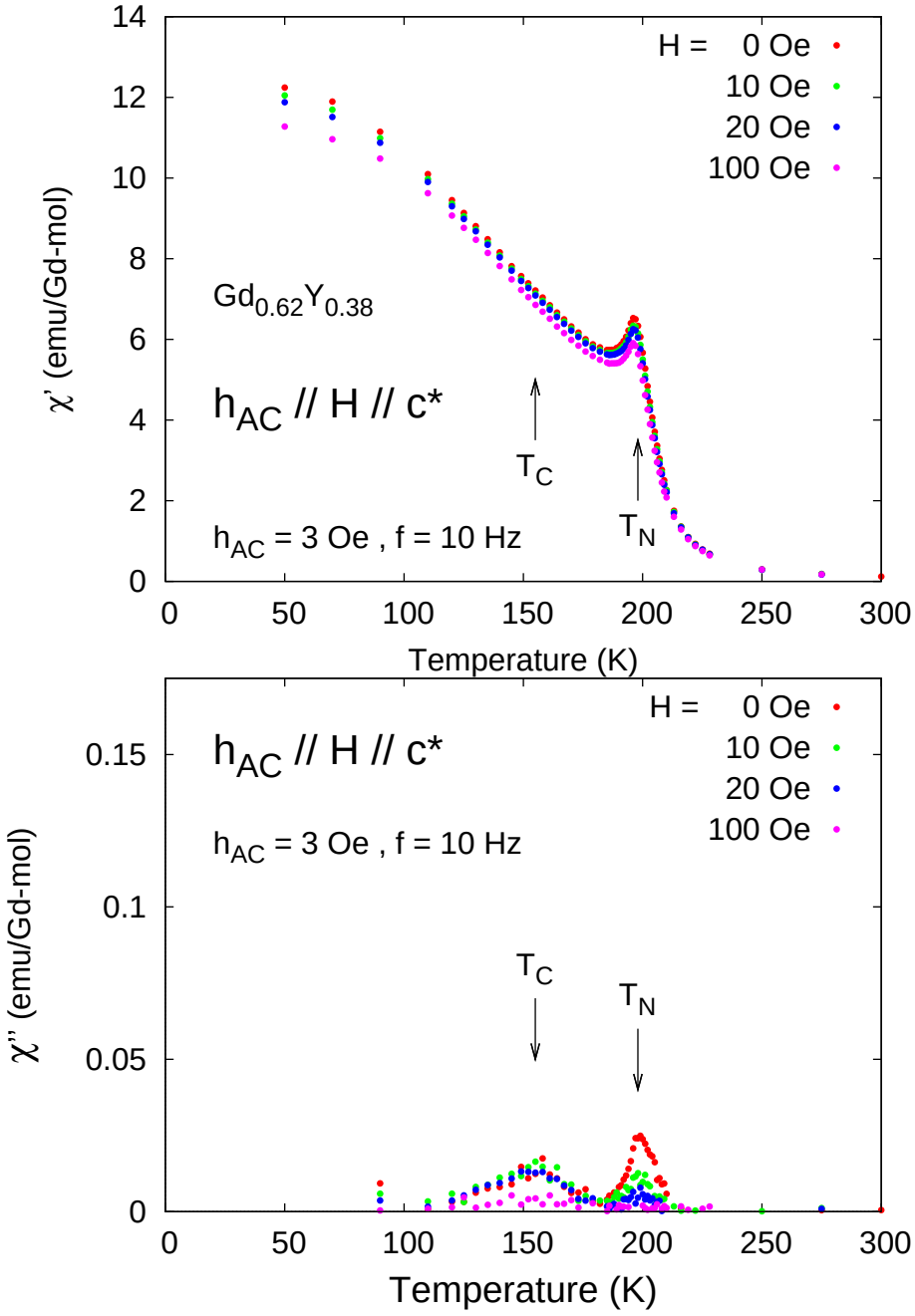

Figure 8.6: The temperature dependence of the AC-susceptibility along the c^*-direction measured with applying the various DC-field.

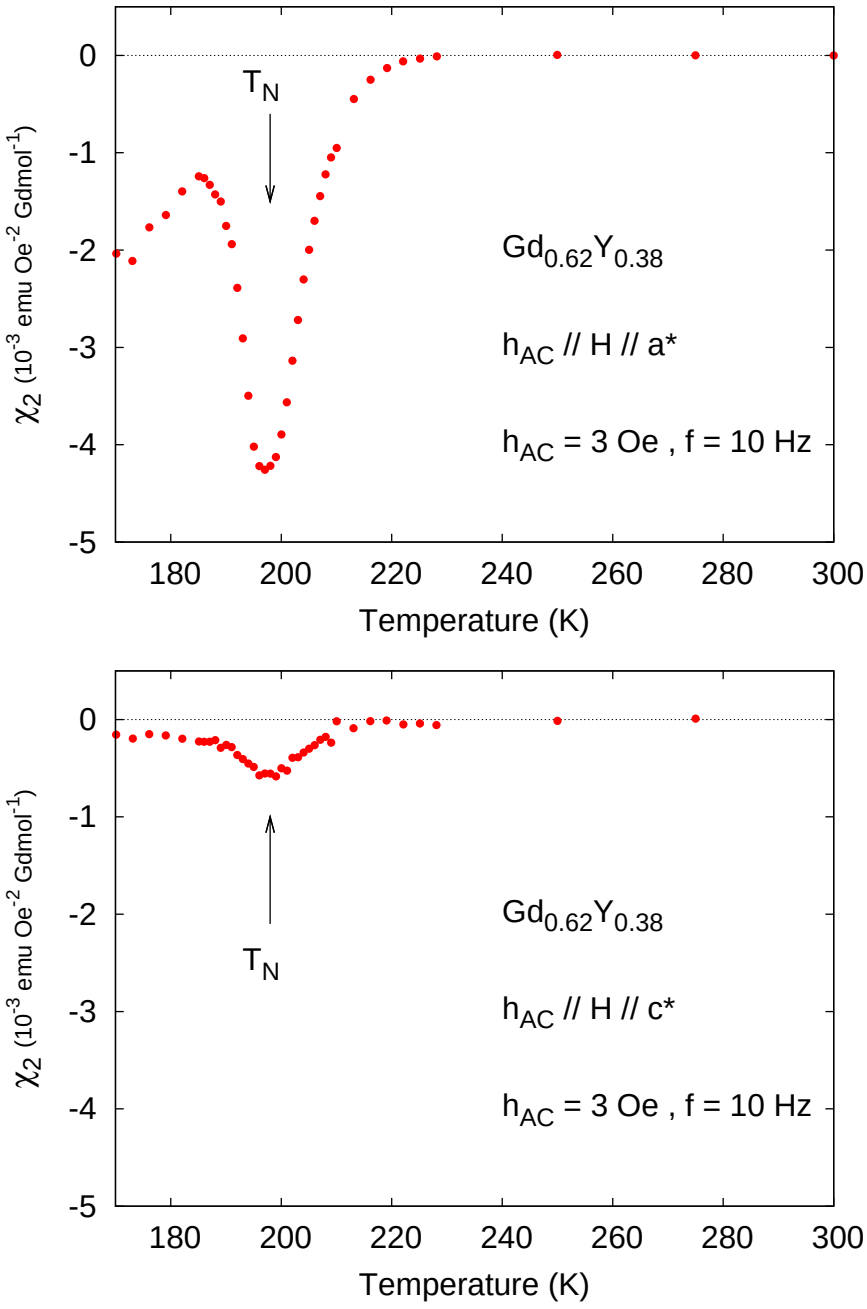

Figure 8.7: The temperature dependence along the a*- and the c*-directions.

8.2.2 DC-susceptibility

The DC-magnetization measurements were performed with applying the the various DC-field H. The effected magnetic field H_{eff} was estimated by subtracting the demagnetization field H_d from the applied field H. Figure 8.8 shows the temperature dependences of the effective DC-susceptibility, $\chi = M/H_{eff}$, along the a*-direction with the several effective field H_{eff}. The strong nonlinearity of the DC-magnetization for the H_{eff} was also observed in the low field range of $H_{eff} < 400$ Oe. The arrows in the figure represents the maximums of the χ, which is regarded as the transition temperature $T_{\rm N}(H)$. The decrease of the $T_{\rm N}(H)$ was found with increasing the magnetic field above 600 Oe, which was not found below 400 Oe.

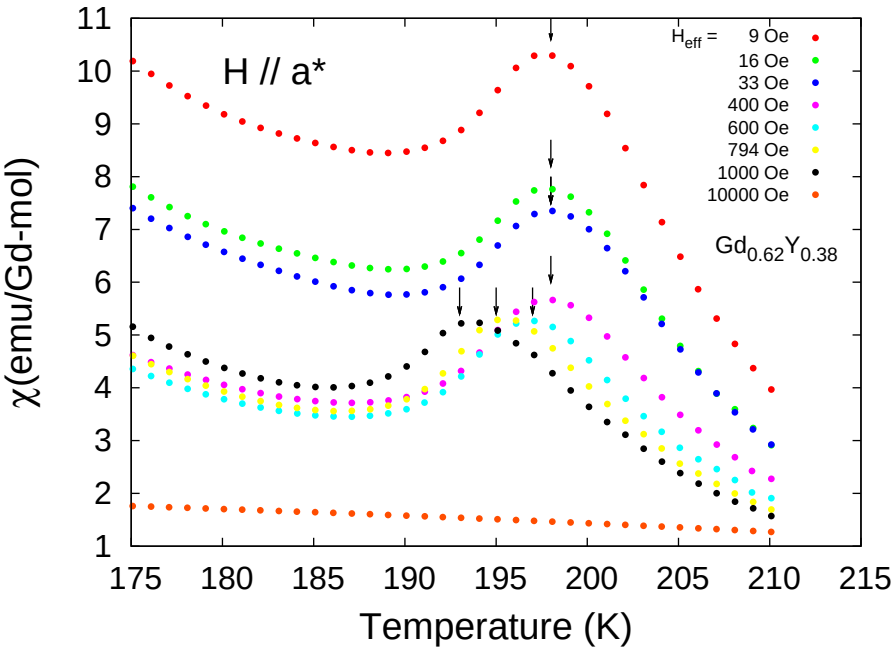

Figure 8.8: The temperature dependence of the DC-susceptibility, $\chi = M/H_{eff}$, along the a*-direction with the various effective field H_{eff}.

8.2.3 Comparison study in reference samples Ho and Ho_{1-x}-Y_x alloy

The same AC-susceptibility measurements were performed in similar rare-earth helical magnets Ho and $Ho_{0.60}Y_{0.40}$ alloy as that in the in $Gd_{0.62}Y_{0.38}$ alloy. The magnetic structure of the Ho is also a proper type helical structure and $T_N = 133$ K , therefore, the Ho can be a good reference material. The divergent behavior of the χ_2 and the increase of the χ'' observed in the $Gd_{0.62}Y_{0.38}$ alloy can be caused by the randomness of the Gd atoms because these behavior are also observed in the spin glasses arising from a randomness of magnetic elements. The randomness are caused by the dilution effect of Y atoms, which is considered as a non-magnetic element. Accordingly, the measurements were performed also in the diluted system $Ho_{1-x}Y_x$. The transition temperature T_N decrease with increasing the Y concentration x[77], and $T_N = 92$ K st $x = 0.40$.

Figure 8.9 shows the temperature dependences of the real part of the AC-suscepticility χ' in the Ho and the $Ho_{0.60}Y_{0.40}$ measured with applying the DC-field of 0 Oe and 100 Oe. No difference of the χ' around the T_N was observed between in zero DC-field and in the DC-field of 100 Oe, and nonlinearity was not observed in both the Ho and the $Ho_{0.60}Y_{0.40}$ alloy.

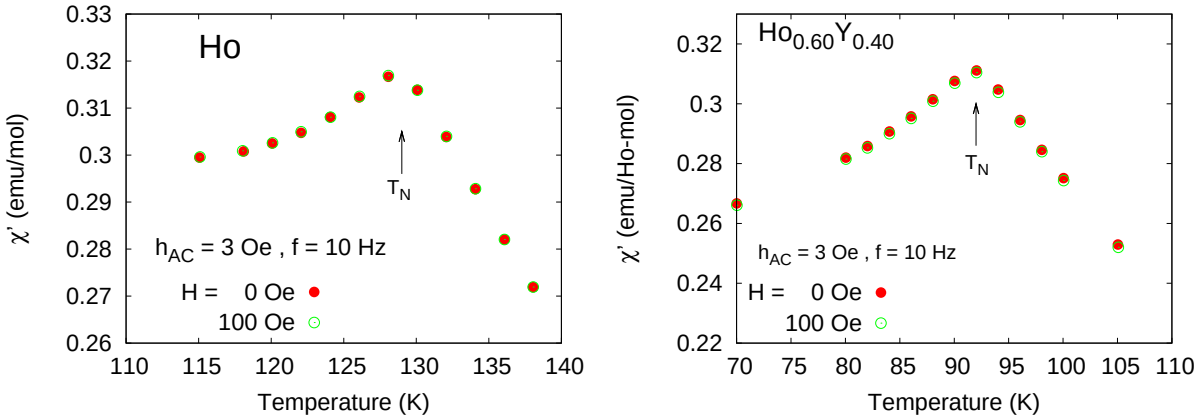

Figure 8.9: The temperature dependences of the real part of the AC-suscepticility χ' in the Ho (left) and the $Ho_{0.60}Y_{0.40}$ (right) measured with applying the DC-field of 0 Oe and 100 Oe.

Figure 8.10 shows the temperature dependences of the imaginary part of the AC-suscepticility χ'' in the Ho and the $Ho_{0.60}Y_{0.40}$ measured with applying the DC-field of 0 Oe and 100 Oe. The behaviors of χ'' around T_N were flat and no anomaly was observed in both materials.

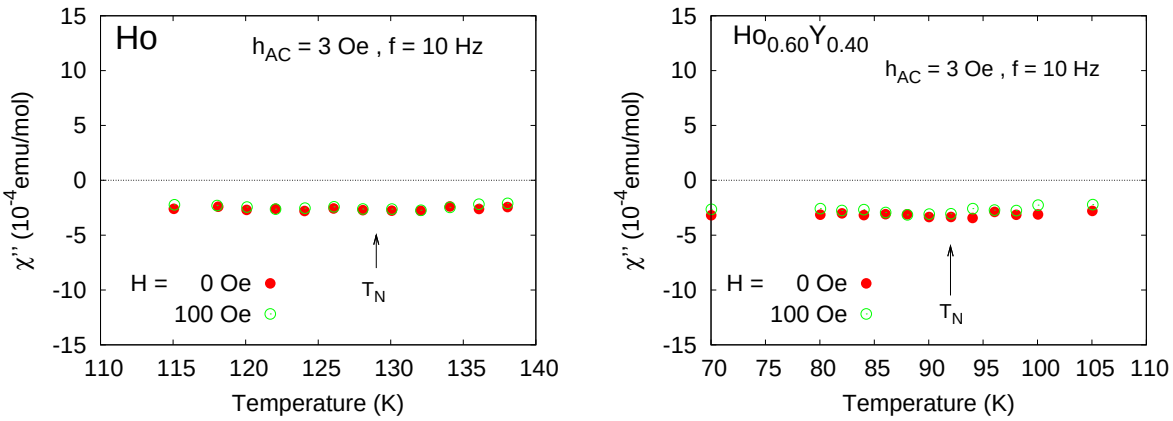

Figure 8.10: The temperature dependences of the imaginary part of the AC-suscepticility χ'' in the Ho (left) and the $Ho_{0.60}Y_{0.40}$ (right) measured with applying the DC-field of 0 Oe and 100 Oe.

8.2.4 Discussion

From the AC- and the DC-magnetization measurements for the $Gd_{0.62}Y_{0.38}$ alloy,

- the remarkable increase of the χ'' in the T-range of the helical phase
- the nonlinearity of the magnetization at T_N

were observed in the helical plane. On the other hand, these behaviors along the helical axis were very weaker. They are nontrivial behaviors. In previous study, the nonlinearity behavior of the AC-susceptibility has been observed at T_N also in similar dilute system $Gd_{1-x}La_x$ alloys [78]. The temperature dependences of the AC-susceptibility of the polycrystalline $Gd_{0.73}La_{0.27}$ measured with applying the various DC-fields are shown in Fig.8.11. The very sharp peak of the AC-susceptibility was found at $H = -0.5$ Oe, which was applied for cancel out the residual magnetic field in the apparatus. The peak decreases with increasing DC-field H. It is known that the similar behaviors of the AC-susceptibility are observed in the diluted spin glass materials, e.g. $Au_{1-x}Fe_x$ alloys, nevertheless, they were not observed in the diluted $Ho_{0.60}Y_{0.40}$. Therefore, the anomalous behaviors of AC-susceptibility are not likely caused by the randomness. Above results suggest that the anomalous behaviors, the nonlinearity of the magnetization and the increase of the χ'', are originated from the weak magnetic anisotropy of Gd^{3+}-ion, which has no orbital angular moment ($L = 0$). In particular, the in-plane anisotropy is vanishingly weak in the $Gd_{1-x}Y_x$ alloys.

The remarkable increase of the χ'' suggests the slow dynamics of the spins, which is probably a collective spin dynamics. Here, I speculate that the spin rotation dynamics in the helical plane with keeping the helix is spontaneously occurs even without electric current in the helical phase of the $Gd_{1-x}Y_x$ alloys. Such rotation dynamics can be realize as one of the low energy excitation mode. In this speculation, the behaviors of the χ'' in the T-range of the helical phase can be explained as below. If a rotation mode of the frequency same as that of applied AC-field h_{AC}, the dissipation component of the AC-susceptibility χ'' increases because of a resonance absorption. The divergent increase of the χ'' at T_N can be accompanied by increase of the spin fluctuation. When the DC-feild H is applied along in the helical plane, the rotation of spins are suppressed by induced anisotropy, and the χ'' decreases. Although the weak increase of the χ'' was observed along the c^*-direction, it can be caused by another excitation states, which is oscillation like as the tilting the helical plane. This rotation dynamics is, in other words, a state that the spins rotate and are not ordered but the chiralities are ordered as the helical structure, which is the ferro-chiral ordered state. In short, it can be a kind of the spin-chirality decoupling state which is expected in the frustrate spin systems[3].

Next, I discuss the origin of the nonlinearity of the magnetization. Figure 8.12 shows the $H-T$ phase diagram expected from the results of the DC-magnetization measurements in the $Gd_{0.62}Y_{0.38}$ alloy. As shown in Fig.6.4, the turn angle of the helical structure in zero magnetic field has been investigated by the previous neutron scattering experiments in the $Gd_{1-x}Y_x$ alloys. In zero magnetic field, magnetic wave number vector q continuously changes to $q = 0$ at the ferro-helical transition temperature $T_{\rm C}$, and it discontinuously changes from $q \neq 0$ to $q = 0$ at helical-para transition temperature $T_{\rm N}$. In finite magnetic field, the transition temperature $T_{\rm C}(H)$, where the q continuously changes to $q \neq 0$, and the $T_{\rm N}(H)$, where the q discontinuously changes from to $q \neq 0$ to $q \neq 0$ are contact with each other at some point ("?" in the figure) in the $H-T$ phase diagram. The contact point would be a special and a multi-critical point such as the Lifshitz point. If $T_{\rm N}(0)$ is such a special point, the magnetization process can be a non-analytic at $T_{\rm N}(0)$ and χ_2 can be a divergent. In recent study, it is indicated that the ferro-helical magnetic phase transition at $T_{\rm C}(0)$ can be a 2.5-order magnetic phase transition [74], therefore, the profound consideration will be needed to understanding these magnetic phase transitions. It is a interesting theme to investigate the magnetic phase transitions $T_{\rm C}(H)$ and $T_{\rm N}(H)$ and to complete the $H-T$ phase diagram, and the neutron scattering experiments in the magnetic field is expected in the future.

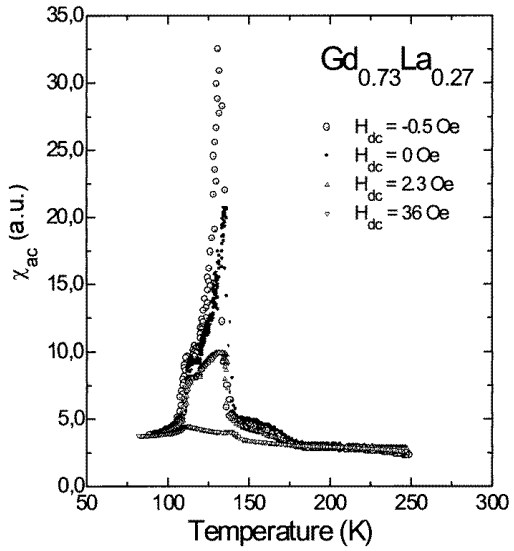

Figure 8.11: The temperature dependence of the AC-susceptibility of the polycrystalline $Gd_{0.73}La_{0.27}$ measured with applying the various DC-fields.

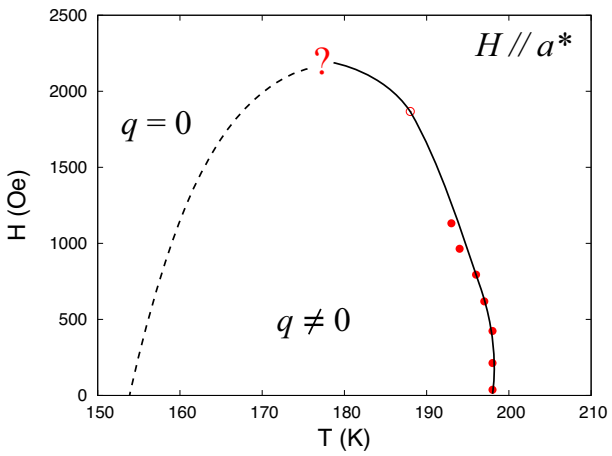

Figure 8.12: The $H-T$ phase diagram of the $Gd_{0.62}Y_{0.38}$ alloy expected from the results of the DC-magnetization measurements.

Chapter 9

Conclusion

In order to observe the current-driven spin dynamics predicted theoretically in a bulk helical magnet, the AC susceptibility measurements along the in-plane direction with applying electric current parallel to the helical axis in the rare-earth helical magnet $Gd_{0.62}Y_{0.38}$ alloy were performed. Although the suppression of the real and the imaginary parts of the AC-susceptibility, χ' and χ'', caused by applying the electric current were observed, I could not distinguish the effect of the electric current itself and the effect of the magnetic field accompanying the electric current, because the AC susceptibility of the alloy is also easily suppressed by the DC magnetic field of 10 Oe.

From the AC- and the DC-magnetization measurements for the $Gd_{0.62}Y_{0.38}$ alloy,

1. the remarkable increase of the χ'' in the T-range of the helical phase
2. the strong nonlinearity of the magnetization at $T_{\rm N}$

were observed only along the in-plane direction. The remarkable increase of the χ'' indicates an existence of the slow dynamics in the helical phase in the $Gd_{1-x}Y_x$ alloys. We speculate that the slow dynamics originates from the dynamics of spins with keeping the helical spin arrangement. In other words, the spins themselves can be rotated by the AC magnetic field, however, the vector chirality is preserved. It suggests a spin-chirality decoupling in the helical phase of $Gd_{0.62}Y_{0.38}$. The strong nonlinearity of the magnetization at $T_{\rm N}$ can be related to the multicritical behavior, which is expected from the $H-T$ phase diagram where the paramagnetic-helical phase transition line $T_{\rm N}(H)$ may merge with the ferromagnetic-helical phase transition line $T_{\rm C}(H)$.

Appendix A

Analysis for the conventional double helical structure

The following is the integrated intensity of a reciprocal lattice point (hkl) in elastic neutron scattering experiments.

$$I = A \cdot N \cdot S(\boldsymbol{k}) \cdot E(\boldsymbol{k}) \cdot L(\boldsymbol{k}) \cdot |F(\boldsymbol{k})|^2 \tag{A.1}$$

A : universal constant common to a certain experiment
N : number of unit cells
$S(\boldsymbol{k})$: absorption factor
$E(\boldsymbol{k})$: secondary extinction factor
$L(\boldsymbol{k})$: Lorentz factor
$F(\boldsymbol{k})$: structure factor

Forsyth performed the neutron scattering experiments for the single crystal of MnP, and analyzed its intensities of the magnetic reflections[23]. Finally he concluded the helical structure of MnP is a double spiral type with the difference of the relative phase between the N. N. Mn-spins and all the spins lie in the bc plane. Here, his analysis is mentioned.

He defined a continuous function $\eta_{\nu \boldsymbol{r}}$ which gives the magnitude and direction of the spin on the νth atom in the unit cell. For a structure containing a spiral with propagation vector $\boldsymbol{\delta}$

$$\eta_{\nu \boldsymbol{r}} = \boldsymbol{q}_c \cos(\boldsymbol{\delta} \cdot \boldsymbol{r} + \gamma_\nu) + \boldsymbol{q}_b \sin(\boldsymbol{\delta} \cdot \boldsymbol{r} + \gamma_\nu) \tag{A.2}$$

where $\boldsymbol{q}_c$, $\boldsymbol{q}_b$ are the c- and b-components of the spin and γ_ν is the relative phase. Since only the perpendicular components of the magnetic moment to the scattering vector contribute to the magnetic scattering, the magnetic structure factor $F_{\mathrm{M}}(\boldsymbol{k})$

is given by

$$|\boldsymbol{F}_{\mathrm{M}}|^2 = |\boldsymbol{P}(\boldsymbol{e})|^2 - |\boldsymbol{P}(\boldsymbol{e}) \cdot \hat{\boldsymbol{e}}| \tag{A.3}$$

where $\hat{\boldsymbol{e}}$ is a unit vector in the direction of $\boldsymbol{e}$, the neutron scattering vector, and

$$\boldsymbol{P}(\boldsymbol{e}) = \sum_{n\nu} f_\nu(\boldsymbol{e}) \boldsymbol{S}_{n\nu} \exp(i\boldsymbol{e} \cdot \boldsymbol{r}_{n\nu}) \tag{A.4}$$

where $f_\nu(\boldsymbol{e})$ is the form factor for the νth magnetic atom, $\boldsymbol{r}_{n\nu}$ is the vector from the origin to the νth atom of the n th unit cell, and $\boldsymbol{S}_{n\nu}$ fives the magnitude and direction of its spin. Writing

$$\boldsymbol{S}_{n\nu} = \delta(\boldsymbol{r} - \boldsymbol{r}_{n\nu}) \boldsymbol{\eta}_{n\nu} d\tau \tag{A.5}$$

and defining $Q_\nu(\boldsymbol{k})$ such that

$$\boldsymbol{\eta}_{n\nu} = \sum_k \boldsymbol{Q}_\nu(\boldsymbol{k}) \exp(i\boldsymbol{k} \cdot \boldsymbol{r}) \tag{A.6}$$

then by the Fourier transform relation and substituting from eq. A.2

$$\begin{aligned} \boldsymbol{Q}_\nu(\boldsymbol{k}) &= \int_r \boldsymbol{\eta}_r \exp(-i\boldsymbol{k}\boldsymbol{r}) d\tau \\ &= \frac{1}{2}\boldsymbol{q}_c \int_r \exp[i\{(-\boldsymbol{k} + \boldsymbol{\delta}) \cdot \boldsymbol{r} + \gamma_\nu\}] + \exp[\{i(-\boldsymbol{k} - \boldsymbol{\delta}) \cdot \boldsymbol{r} - \gamma_\nu\}] d\tau \\ &\quad + \frac{1}{2}\boldsymbol{q}_b \int_r \exp[i\{(-\boldsymbol{k} + \boldsymbol{\delta}) \cdot \boldsymbol{r} + \gamma_\nu\}] - \exp[\{i(-\boldsymbol{k} - \boldsymbol{\delta}) \cdot \boldsymbol{r} - \gamma_\nu\}] d\tau \end{aligned} \tag{A.7}$$

The first term of each integrals is zero unless $\boldsymbol{\delta} = \boldsymbol{k}$ and the second is zero unless $\boldsymbol{\delta} = -\boldsymbol{k}$. From eq. A.4, A.5, A.6 and A.7

$$\boldsymbol{P}(\boldsymbol{e}) = \sum_{n\nu\boldsymbol{k}} f_\nu(\boldsymbol{e}) \boldsymbol{Q}(\boldsymbol{k}) \exp\{i(\boldsymbol{k} + \boldsymbol{e}) \cdot \boldsymbol{r}_{n\nu}\}$$

and since $\boldsymbol{r}_{n\nu}$ can be written as $\boldsymbol{R}_n + \boldsymbol{r}_\nu$ this becomes

$$\boldsymbol{P}(\boldsymbol{e}) = \sum_{\nu\boldsymbol{k}} f_\nu(\boldsymbol{e}) \boldsymbol{Q}(\boldsymbol{k}) \exp\{i(\boldsymbol{k} + \boldsymbol{e}) \cdot \boldsymbol{r}_\nu\} \sum_n \exp\{i(\boldsymbol{k} + \boldsymbol{e}) \cdot \boldsymbol{R}_n\}$$

Now $\sum_n \exp\{i(\boldsymbol{k} + \boldsymbol{e}) \cdot \boldsymbol{R}_n\}$ is an interference function and, if the number of unit cells is large, is essentially zero unless $\boldsymbol{k} + \boldsymbol{e}$ is equal to a reciprocal lattice vector

$\boldsymbol{K}$. After all, there will be no magnetic scattering except when $\boldsymbol{e} = \boldsymbol{K} + \boldsymbol{\delta}$ or $\boldsymbol{K} - \boldsymbol{\delta}$. The satellite peaks will be observed at $\boldsymbol{K} \pm \boldsymbol{\delta}$.

$$\boldsymbol{P}(\boldsymbol{K}+\boldsymbol{\delta}) \propto \sum_{\nu} f_{\nu}(\boldsymbol{K}+\boldsymbol{\lambda})\frac{1}{2}[\boldsymbol{q}_c \exp\{i(\boldsymbol{K}\cdot\boldsymbol{r}_{\nu} - \gamma_{\nu})\} - \boldsymbol{q}_b \exp\{i(\boldsymbol{K}\cdot \mathrm{r} - \gamma_{\nu})\}] \tag{A.8}$$

$$\boldsymbol{P}(\boldsymbol{K}-\boldsymbol{\delta}) \propto \sum_{\nu} f_{\nu}(\boldsymbol{K}-\boldsymbol{\lambda})\frac{1}{2}[\boldsymbol{q}_c \exp\{i(\boldsymbol{K}\cdot\boldsymbol{r}_{\nu} + \gamma_{\nu})\} + \boldsymbol{q}_b \exp\{i(\boldsymbol{K}\cdot \mathrm{r} + \gamma_{\nu})\}] \tag{A.9}$$

The lattice parameter are given below[79].

$$a = 5.918, b = 5.258, c = 3.172$$

The atomic positions are

$$\begin{aligned} 4\mathrm{Mn\ in\ } 4(c)(x,y,1/4) \text{ with} \quad x_1 &= \quad 0.1965 \\ y_1 &= \quad 0.049 \\ 4\mathrm{P\ in\ } 4(c)(x,y,1/4) \text{ with} \quad x_2 &= \quad 0.5686 \\ y_2 &= \quad 0.1878 \end{aligned}$$

The position of the $\nu = 1 \sim 4$th Mn atoms are assigned as follows.

$$\begin{aligned} \boldsymbol{r}_1 &= (x_1, y_1, 1/4) \\ \boldsymbol{r}_2 &= (-x_1 - 1/2, y_1 - 1/2, 1/4) \\ \boldsymbol{r}_3 &= (-x_1, -y_1, -1/4) \\ \boldsymbol{r}_4 &= (x_1 + 1/2, -y_1 + 1/2, -1/4) \end{aligned} \tag{A.10}$$

Assuming the $\gamma_1 = \gamma_4$ and $\gamma_2 = \gamma_3$, which are given by the Forsyth' analysis, the c-component of the $\boldsymbol{P(K-\delta)}$ in eq.A.9 can be expressed as

$$\frac{P(\boldsymbol{K}-\boldsymbol{\delta})_c}{C f_{\mathrm{Mn}}(\boldsymbol{K}-\boldsymbol{\delta})} = 2\exp\left(\frac{\gamma_1+\gamma_2}{2}\right)\cos\left(X - \left(\frac{\gamma_2-\gamma_1}{2}\right)\right)\cos(Y) \tag{A.11}$$

where

$$\begin{aligned} X &= 2\pi\left(hx_1 + \frac{1}{4}(h+k)\right) \\ Y &= 2\pi\left(ky_1 - \frac{1}{4}(h+k-l)\right) \end{aligned}$$

C is a constant which is indipendent of $\boldsymbol{K}$. The b-component of $\boldsymbol{P}(\boldsymbol{K}-\boldsymbol{\delta})$ is similar and the components of $\boldsymbol{P}(\boldsymbol{K}+\boldsymbol{\delta})$ are the same except $X-(\gamma_2-\gamma_1)/2$ are replaced by $X+(\gamma_2-\gamma_1)/2$. Even the non-polarized neutron scattering, the intensity of the magnetic reflections of $\boldsymbol{K}+\boldsymbol{\delta}$ and $\boldsymbol{K}-\boldsymbol{\delta}$ are asymmetric in MnP. Forsyth explained its asymmetry by assuming the double helical structure with the relative phase difference of $\gamma_1-\gamma_2=15.8^\circ$.

The structure factor for the nuclear scattering is given by

$$F(\boldsymbol{K}) = b_{\mathrm{Mn}} \cos X \cos Y + b_{\mathrm{P}} \cos X' \cos X'. \tag{A.12}$$

where X', Y' are the same as X, Y except the x_1, y_1 are replaced by x_2, y_2. Therefore, the extinction rules are

$$h = 0 \quad \text{and} \quad k = \text{odd} \tag{A.13}$$

$$h = \text{odd} \quad \text{and} \quad k = 0. \tag{A.14}$$

Acknowledgement

This work owes much to many collaborators. The encounter with them was stimulative and fortunate for me.

First, I would like express the deepest gratitude to Prof. Hiroyuki Nakamura for his valuable suggestions, enlightening discussions and continuous encouragement during my present work. I also wish to express great thanks to Dr. Yohikazu Tabata for his stimulating discussions and variable suggestions. He is the best collaborator and the teacher throughout my present study. I also wish to express sincere thanks to Dr. Takeshi Waki for his variable discussions and his helps. The shaping the sample and the determination of the axes of the samples were performed at Inui Laboratory. I would like to express grate thanks to Prof. Haruyuki Inui and Dr. Katsushi Tanaka for their kindness. I would like to express special thanks to Yusuke Takahashi for his helpful assistance and variable discussions. I would also like to thank to all members in Nakamura laboratory. I had enjoyed my student life with them.

Finally, I wish to express the greatest thanks for my family for their sincere supports.

Bibliography

[1] J. Villain. A magnetic analogue of stereoisomerism: application to helimagnetism in two dimensions. *Journal de Physique*, 38(4):385–391, 1977.

[2] S. Miyashita and H. Shiba. Nature of the phase transition of the two-dimensional antiferromagnetic plane rotator model on a triangular lattice. *Journal of the Physical Society of Japan*, 53(3):1145–1154, 1984.

[3] H. Kawamura and S. Miyashita. Phase transition of the two-dimensional Heisenberg antiferromagnet on the triangular lattice. *Journal of the Physical Society of Japan*, 53(12):4138–4154, 1984.

[4] J. Ye, Y.B. Kim, AJ Millis, BI Shraiman, P. Majumdar, and Z. Tešanović. Berry phase theory of the anomalous Hall effect: application to colossal magnetoresistance manganites. *Physical review letters*, 83(18):3737–3740, 1999.

[5] Y. Taguchi, Y. Oohara, H. Yoshizawa, N. Nagaosa, and Y. Tokura. Spin chirality, Berry phase, and anomalous Hall effect in a frustrated ferromagnet. *Science*, 291(5513):2573, 2001.

[6] G. Tatara and H. Kawamura. Chirality-driven anomalous Hall effect in weak coupling regime. *JOURNAL-PHYSICAL SOCIETY OF JAPAN*, 71(11):2613–2616, 2002.

[7] T. Kimura, T. Goto, H. Shintani, K. Ishizaka, T. Arima, and Y. Tokura. Magnetic control of ferroelectric polarization. *Nature*, 426(6962):55–58, 2003.

[8] Y. Yamasaki, S. Miyasaka, Y. Kaneko, J.P. He, T. Arima, and Y. Tokura. Magnetic reversal of the ferroelectric polarization in a multiferroic spinel oxide. *Physical review letters*, 96(20):207204, 2006.

[9] K. Taniguchi, N. Abe, T. Takenobu, Y. Iwasa, and T. Arima. Ferroelectric Polarization Flop in a Frustrated Magnet MnWO_ {4} Induced by a Magnetic Field. *Physical review letters*, 97(9):97203, 2006.

[10] T. Taniguchi, K. Yamanaka, H. Sumioka, T. Yamazaki, Y. Tabata, and S. Kawarazaki. Direct observation of chiral susceptibility in the canonical spin glass AuFe. *Physical review letters*, 93(24):246605, 2004.

[11] Y. Yamasaki, H. Sagayama, T. Goto, M. Matsuura, K. Hirota, T. Arima, and Y. Tokura. Electric control of spin helicity in a magnetic ferroelectric. *Physical review letters*, 98(14):147204, 2007.

[12] N. Abe, K. Taniguchi, S. Ohtani, T. Takenobu, Y. Iwasa, and T. Arima. Polarization Reversal in Multiferroic TbMnO_ {3} with a Rotating Magnetic Field Direction. *Physical review letters*, 99(22):227206, 2007.

[13] I. Dzyaloshinsky. A thermodynamic theory of. *Journal of Physics and Chemistry of Solids*, 4(4):241–255, 1958.

[14] T. Moriya. Anisotropic superexchange interaction and weak ferromagnetism. *Physical Review*, 120(1):91–98, 1960.

[15] Y. Ishikawa, D. Tajima, et al. Helical spin structure in manganese silicide MnSi. *Solid State Communications*, 19(6):525–528, 1976.

[16] T. Moriya and T. Miyadai. Evidence for the helical spin structure due to antisymmetric exchange interaction in CrNbS2. *Solid State Communications*, 42(3):209–212, 1982.

[17] M. Ishida, Y. Endoh, S. Mitsuda, Y. Ishikawa, and M. Tanaka. Crystal chirality and helicity of the helical spin density wave in MnSi. II. Polarized neutron diffraction. *J. PHYS. SOC. JAPAN.*, 54(8):2975–2982, 1985.

[18] T. Miyadai, K. Kikuchi, H. Kondo, A. Sakka, M. Arai, and Y. Ishikawa. Magnetic properties of Cr sub (1/3) NbS sub (2). *J. PHYS. SOC. JAPAN.*, 52(4):1394–1401, 1983.

[19] H. Katsura, N. Nagaosa, and A.V. Balatsky. Spin current and magnetoelectric effect in noncollinear magnets. *Physical review letters*, 95(5):57205, 2005.

[20] M. Mostovoy. Ferroelectricity in spiral magnets. *Physical review letters*, 96(6):67601, 2006.

[21] E Huber, E and H Ridgley, D. Magnetic properties of a single crystal of manganese phosphide. *Physical Review*, 135:1033–1040, 1964.

[22] GP Felcher. Magnetic Structure of MnP. *Journal of Applied Physics*, 37:1056, 1966.

[23] JB Forsyth, SJ Pickart, and PJ Brown. The structure of the metamagnetic phase of MnP. *Proceedings of the Physical Society*, 88:333–339, 1966.

[24] GP FELCHER, GH LANDER, and TO BRUN. POLARIZATION EFFECTS IN NEUTRON SCATTERING FROM SPIRAL DOMAINS IN MnP. *Le Journal de Physique Colloques*, 32(C1):1–1, 1971.

[25] T. Komatsubara, A. Ishizaki, S. Kusaka, and E. Hirahara. Magnetic field effect on the ultrasonic attenuation in manganese phosphide. *Solid State Communications*, 14(8):741–745, 1974.

[26] H. Obara, Y. Endoh, Y. Ishikawa, and T. Komatsubara. Magnetic Phase Transition of MnP Under Magnetic Field. *J. Phys. Soc. Japan*, 49(3):928–935, 1980.

[27] M Moon, R. Neutron polarization analysis measurements on the spiral phase of MnP. *Journal of Applied Physics*, 53:1956, 1982.

[28] MS Reis, RM Rubinger, NA Sobolev, MA Valente, K. Yamada, K. Sato, Y. Todate, A. Bouravleuv, PJ von Ranke, and S. Gama. Influence of the strong magnetocrystalline anisotropy on the magnetocaloric properties of MnP single crystal. *Physical Review B*, 77(10):104439, 2008.

[29] CC Becerra, Y. Shapira, NF Oliveira Jr, and TS Chang. Lifshitz Point in MnP. *Physical Review Letters*, 44(25):1692–1695, 1980.

[30] Y. Shapira, CC Becerra, NF Oliveira Jr, and TS Chang. Phase diagram, susceptibility, and magnetostriction of MnP: Evidence for a Lifshitz point. *Physical Review B*, 24(5):2780–2806, 1981.

[31] Y. Shapira, NF Oliveira, CC Becerra, and S. Foner. Phase transitions of MnP for a field parallel to the hard-magnetization direction: A possible new Lifshitz point. *Physical Review B*, 29(1):361–373, 1984.

[32] V. Bindilatti, C Becerra, C, and F Oliveira Jr, N. Specific-heat exponent and critical-amplitude ratio at the Lifshitz multicritical point. *Physical Review B*, 40(13):9412–9415, 1989.

[33] C. Becerra, C., V. Bindilatti, and NF Oliveira Jr. Evidence for the Ising-Lifshitz crossover in MnP. *Physical Review B*, 62(13):8965–8968, 2000.

[34] A. Zieba, M. Slota, and M. Kucharczyk. Modulated phases, magnetic phase diagrams, and the Lifshitz point in MnP from the mean field theory. *Physical Review B*, 61(5):3435–3449, 2000.

[35] A. Takase, H. Yashima, and T. Kasuya. Low Temperature Specific Heat of MnP; Experiment and Analysis. *Journal of the Physical Society of Japan*, 47(2), 1979.

[36] A. Yanase and A. Hasegawa. Electronic structure of MnP. *Journal of Physics C: Solid State Physics*, 13:1989–1993, 1980.

[37] K. Naito, A. Kakizaki, T. Komatsubara, H. Sugawara, I. Nagakura, and T. Ishii. Weak 3p-3d Resonance in the Valence Band Photoemission of Manganese Phosphide. *Journal of the Physical Society of Japan*, 54(1):416–423, 1985.

[38] A. Takase and T. Kasuya. Temperature Dependences of Magnetization and Spin Waves in MnP. *Journal of the Physical Society of Japan*, 47(2), 1979.

[39] K. Tajima, Y. Ishikawa, and H. Obara. Neutron scattering studies of the ferro to spiral transition in MNP. *Journal of Magnetism and Magnetic Materials*, 15:373–374, 1980.

[40] Y. Todate, K. Yamada, Y. Endoh, and Y. Ishikawa. Spin-Waves in MnP. *Journal of the Physical Society of Japan*, 56(1):36–38, 1987.

[41] L. Dobrzynski and AF Andresen. On the magnetic double helical structure in MnP-and MnAs-based alloys. *Journal of Magnetism and Magnetic Materials*, 82(1):67–76, 1989.

[42] H. Yoshizawa, S. Shapiro, and T. Komatsubara. Softening of the spin waves in MnP and its relation to the Lifshitz point. *J. PHYS. SOC. JAPAN.*, 54(8):3084–3090, 1985.

[43] CC Becerra. Evidence for a new magnetic phase in MnP at very low fields. *Journal of Physics: Condensed Matter*, 12(27):5889–5895, 2000.

[44] K. Binder and A.P. Young. Spin glasses: Experimental facts, theoretical concepts, and open questions. *Reviews of Modern physics*, 58(4):801–976, 1986.

[45] A. Ito, H. Aruga, E. Torikai, M. Kikuchi, Y. Syono, and H. Takei. Time-Dependent Phenomena in a Short-Range Ising Spin-Glass, Fe_ {0.5} Mn_ {0.5} TiO_ {3}. *Physical review letters*, 57(4):483–486, 1986.

[46] T. Suzuki, Y. Matsumura, and E. Hirahara. Magnetic Field Effects on the Resistivity and Thermoelectric Power of Single Crystal MnP in the Metamagnetic State. *Journal of the Physical Society of Japan*, 21:1446, 1966.

[47] T. Suzuki. Magnetic Field Effects on Electrical Resistivity in Metamagnetic State of MnP Single Crystal. *Journal of the Physical Society of Japan*, 25(6), 1968.

[48] T. Suzuki. The Temperature Dependence of Electrical Resistivity and Thermoelectric Power of Single MnP. *Journal of the Physical Society of Japan*, 25:931, 1968.

[49] A. Takase and T. Kasuya. Temperature Dependences of Electrical Resistivity inMnP. *Journal of the Physical Society of Japan*, 48(2), 1980.

[50] A. Takase and T. Kasuya. Low Field Magnetoresistances in MnP; Purity Dependences of the Magnetic Phase Diagram. *J. PHYS. SOC. JAPAN*, 49(2):484–488, 1980.

[51] A. Takase and T. Kasuya. High Field Magnetoresistance in MnP. *J. PHYS. SOC. JAPAN*, 49(2):489–492, 1980.

[52] T. Yamada, N. Kunitomi, Y. Nakai, DE Cox, and G. Shirane. Magnetic Structure of a-Mn. *Journal of the Physical Society of Japan*, 28(3), 1970.

[53] J. Kishine, K. Inoue, and Y. Yoshida. Synthesis, Structure and Magnetic Properties of Chiral Molecule-Based Magnets. *PROGRESS OF THEORETICAL PHYSICS-SUPPLEMENT-*, 159:82, 2005.

[54] IG Bostrem, J. Kishine, and AS Ovchinnikov. Transport spin current driven by the moving kink crystal in a chiral helimagnet. *Physical Review B*, 77(13):132405, 2008.

[55] Y. Kousaka, J. Kishine, S. Yano, and J. Akimitsu. Possible chiral magnetism in CuB2O4. *Journal of Magnetism and Magnetic Materials*, 310(2):e463–e464, 2007.

[56] JC Slonczewski. Conductance and exchange coupling of two ferromagnets separated by a tunneling barrier. *Physical Review B*, 39(10):6995–7002, 1989.

[57] S.S.P. Parkin, M. Hayashi, and L. Thomas. Magnetic domain-wall racetrack memory. *Science*, 320(5873):190, 2008.

[58] L. Berger. Low-field magnetoresistance and domain drag in ferromagnets. *Journal of Applied Physics*, 49:2156, 1978.

[59] L. Berger. Exchange interaction between ferromagnetic domain wall and electric current in very thin metallic films. *Journal of Applied Physics*, 55:1954, 1984.

[60] L. Berger. Motion of a magnetic domain wall traversed by fast-rising current pulses. *Journal of Applied Physics*, 71:2721, 1992.

[61] A. Yamaguchi, T. Ono, S. Nasu, K. Miyake, K. Mibu, and T. Shinjo. Real-space observation of current-driven domain wall motion in submicron magnetic wires. *Physical review letters*, 92(7):77205, 2004.

[62] H. Tanigawa, K. Kondou, T. Koyama, K. Nakano, S. Kasai, N. Ohshima, S. Fukami, N. Ishiwata, and T. Ono. Current-driven domain wall motion in CoCrPt wires with perpendicular magnetic anisotropy. *Applied Physics Express*, 1(1):11301, 2008.

[63] G. Tatara and H. Kohno. Theory of current-driven domain wall motion: Spin transfer versus momentum transfer. *Physical review letters*, 92(8):86601, 2004.

[64] A. Yamaguchi, K. Yano, H. Tanigawa, S. Kasai, and T. Ono. Reduction of threshold current density for current-driven domain wall motion using shape control. *JAPANESE JOURNAL OF APPLIED PHYSICS PART 1 REGULAR PAPERS SHORT NOTES AND REVIEW PAPERS*, 45(5A):3850, 2006.

[65] O. Wessely, B. Skubic, and L. Nordstr
"om. Current driven magnetization dynamics in helical spin density waves. *Physical review letters*, 96(25):256601, 2006.

[66] WC Thoburn, S. Legvold, and FH Spedding. Magnetic Properties of the Gd-La and Gd-Y Alloys. *Physical Review*, 110(6):1298–1301, 1958.

[67] JMD Coey, V. Skumryev, and K. Gallagher. Rare-earth metals: Is gadolinium really ferromagnetic? *Nature*, 401(6748):35–36, 1999.

[68] SN Kaul and S. Srinath. Gadolinium: A helical antiferromagnet or a collinear ferromagnet. *Physical Review B*, 62(2):1114–1117, 2000.

[69] RJ Melville, RS Eccleston, GJ McIntyre, and SB Palmer. The helical-ferromagnetic phase transition in Gd-Y alloys. *Journal of Physics: Condensed Matter*, 4:10045–10052, 1992.

[70] S. Legvold, P. Burgardt, and BJ Beaudry. Search for Lifshitz points in rare-earth alloys. *Physical Review B*, 22(5):2573–2578, 1980.

[71] A. Michelson. Phase diagrams near the Lifshitz point. I. Uniaxial magnetization. *Physical Review B*, 16(1):577–584, 1977.

[72] T. Ito, S. Legvold, and BJ Beaudry. New look at magnetism in single-crystal Gd-Y alloys. *Physical Review B*, 23(7):3409–3413, 1981.

[73] ME Braga, RP Pinto, JB Sousa, GN Blackie, DJ Hemsley, and SB Palmer. The onset of helimagnetism in Gd-Y alloys. *Journal of Magnetism and Magnetic Materials*, 29(1-3):203–208, 1982.

[74] A.V. Andrianov and OA Savelieva. Possible-order magnetic phase transition in the Gd1-xYx system. *EPL (Europhysics Letters)*, 82:47012, 2008.

[75] HM Fretwell, SB Dugdale, MA Alam, DCR Hedley, A. Rodriguez-Gonzalez, and SB Palmer. Fermi surface as the driving mechanism for helical antiferromagnetic ordering in Gd-Y alloys. *Physical review letters*, 82(19):3867–3870, 1999.

[76] S. Bates, SB Palmer, JB Sousa, GJ McIntyre, D. Fort, S. Legvold, BJ Beaudry, and WC Koehler. Magnetic structure of Gd-Y single-crystal alloys from neutron diffraction and magnetization measurements. *Physical review letters*, 55(27):2968–2971, 1985.

[77] HR Child, WC Koehler, EO Wollan, and JW Cable. Magnetic Properties of Heavy Rare Earths Diluted by Yttrium and Lutetium. *Physical Review*, 138:1655–1660, 1965.

[78] C. Larica, E. Nunes, and JCC Freitas. Low field magnetic studies of Gd sub 1-x La sub x alloys. *Journal of Physics, Condensed Matter(UK)*, 11(3):821–831, 1999.

[79] S. RUNDQVIST and UPPSALA UNIV (SWEDEN). Phosphides of the B31 (MnP) structure type. *Acta Chem. Scand*, 16(2):287–292, 1962.

Published works

[1] T. Yamazaki, Y. Tabata, T. Waki, H. Nakamura, M. Matsuura and N. Aso. Anomalous phase of MnP at very low field. In *Journal of Physics: Conference Series*, Vol. 200, p. 032079. Institute of Physics Publishing, 2010.

[2] T. Taniguchi, K. Yamanaka, H. Sumioka, T. Yamazaki, Y. Tabata, and S. Kawarazaki. Direct observation of chiral susceptibility in the canonical spin glass AuFe. *Physical Review Letters*, Vol. 93, No. 24, p. 246605, 2004.

[3] T. Taniguchi, T. Yamazaki, K. Yamanaka, Y. Tabata, and S. Kawarazaki. Critical phenomena in canonical spin glass AuMn from Hall effect measurements. *Journal of Magnetism and Magnetic Materials*, Vol. 310, No. 2, pp. 1526-1528, 2007.

[4] T. Taniguchi, K. Yamanaka, T. Yamazaki, Y. Tabata, S. Kawarazaki, and H. Kawamura. Chiral Susceptibility of the Canonical Spin Glass AuFe. In *AIP Conference Proceedings*, Vol. 850, p. 1115, 2006.

[5] K. Yamanaka, T. Taniguchi, T. Yamazaki, and S. Kawarazaki. Anisotropy Dependence of the Chiral Susceptibility in Canonical Spin Glasses. In *AIP Conference Proceedings*, Vol. 850, p. 1117, 2006.

[6] K. Yamanaka, T. Taniguchi, T. Yamazaki, N. Ashitaka, Y. Mori- moto, Y. Tabata, and S. Kawarazaki. Anisotropy dependence of anomalous Hall effect in canonical spin glass alloys. *Journal of Physics: Condensed Matter*, Vol. 19, p. 145222, 2007.

[7] K. Yamanaka, T. Taniguchi, T. Yamazaki, N. Ashitaka, Y. Mori- moto, Y. Tabata, and S. Kawarazaki. Relation between anomalous Hall effect and the Dzaloshisky-Moriya anisotropy in the series of (Ag1-xAux) 0.9 Mn0. 1 alloys. *Journal of Magnetism and Magnetic Materials*, Vol. 310, No. 2, pp. 1523-1525, 2007.

[8] Y. Tabata, T. Yamazaki, M. Okue, H. Nakamura, and M. Matsuura. Anisotropic magnetic dffuse scattering in an easy-plane type anti- ferromagnet ErNi2Ge2. In *Journal of Physics: Conference Series*, Vol. 145, p. 012078. Institute of Physics Publishing, 2009.